ClassNK Technical Journal

No.2
2020（I）

ClassNK Technical Journal　No.2　2020（Ⅰ）

— CONTENTS —

Special Feature Articles on Reduction of GHG Emissions

Introduction of 4th IMO GHG Study 2020 ····· *Research Institute* ····· 1

IMO will publish the fourth GHG study by the end of 2020. NK participated in the International Consortium, which was tasked to draft this report, and roll to validate the overall QA/QC. The study provides the information on trends in GHG emissions and Carbon Intensity from 2012 to 2018, as well as CO_2 emission forecasts for 2050. The results should be crucial for evaluating the achievement of IMO's GHG reduction strategy. This report introduces these contents.

Roadmap to Zero Emission from International Shipping

····· *Japan Ship Technology Research Association. Marika NISHIMURO* ····· 13

Amid globally growing momentum for decarbonization, Japan established the “Shipping Zero Emission Project” in collaboration with industrial, academic, and public sectors with a view to tackle the climate change while ensuring the sustainable growth maritime transport and related industries. In this article, possible GHG emissions pathways that enable international shipping to meet the GHG reduction target set out in the IMO GHG reduction strategy and actions necessary to be taken by stakeholders to realize the pathways with their timelines (the Roadmap) considered by the Project are introduced.

Trends in Sustainable Finance with Potential Impacts on the Shipping Industry

····· *Intelligence & Strategy Team* ····· 21

Sustainable finance is defined as “the incorporation of environmental, social, and governance (ESG) principles into business decisions, economic development, and investment strategies.” This paper presents an overview of the principles and standards for evaluating whether the use of funds is sustainable or not in the case of sustainable finance with potential impacts on the shipping industry, concretely, in fund-raising by shipping companies.

Technical Topics

Wind-Assisted Propulsion Systems for Ships ····· *Technical Solution Department* ····· 27

“Wind power” has been used in shipping since antiquity, and is now in the spotlight again as a form of clean energy due to the heightened trend toward environmental regulation in recent years. In response to the current situation in which the development of wind propulsion systems utilizing state-of-the-art technologies is progressing worldwide, in 2019 ClassNK issued “Guidelines for Wind-Assisted Propulsion Systems for Ships,” which provides guidelines for wind-assisted propulsion system safety. This paper presents an overview of wind-assisted propulsion systems to date and the current status of this technology, together with an outline of the above-mentioned “Guidelines.”

Recent Research Progresses for Elucidating the Mechanism and Establishing Rational Control Methods for Brittle Crack Arrest ····· *The University of Tokyo Kazuki SHIBANUMA* ····· 35

In recent years, use of high strength and heavy gauge steel plates in container ships has progressed rapidly, and the heightened possibility of brittle fracture has become a concern, as this is the most dangerous failure mode in ship hull structures. In order to prevent catastrophic damage due brittle fracture in the unlikely event of a fracture, it important to study two-stage safety design, that is, "double integrity," which is capable of controlling and arresting crack propagation after initiation. This paper presents an outline of recent trends in research on elucidation of the mechanism of brittle crack arrest and the establishment of a method for its rational control, centering on the results obtained in the research projects "Fracture mechanics research for elucidation of the long crack problem (August 2014 to March 2018)" and "Development of a fracture mechanics model for realization of structural arrest design (April 2018, now continuing)" carried out with ClassNK as "Joint research at industry request."

Simple Evaluation Method for Ultimate Strength of Rectangular Plates under Combined Load

····· *Hull Rules Development Department Shin Kurushima Dockyard Co., Ltd. Toshifumi IKEMOTO, Osaka University Graduate School of Engineering Akira TATSUMI, Masahiko FUJIKUBO* ····· 63

Accurate evaluation of the ultimate strength of plates and stiffeners, which are basic elements of the ship hull structure, is extremely important for safety assessments of ships.
In this paper, the authors developed an evaluation method for the ultimate strength of rectangular plates by formulating the controlling factors for ultimate strength, namely, elastic buckling, initial imperfections and yielding, in physical terms as far as possible, and expressed this method in an explicit formula which does not depend on numerical analysis techniques such as repeated convergent calculations.

Trends in Utilization and Transportation Technologies for Hydrogen and Other Clean Fuels

····· *Renewables and Environment Department* ····· 83

Production, transportation and use of hydrogen and other clean fuels is under study with the aim of reducing CO_2 emissions. At present, the production cost of clean fuels is higher in comparison with fossil fuels, and how to reduce total CO_2 emissions, including the production and transportation processes, is an issue.
This paper introduces the outlook for the utilization of hydrogen and other clean fuels which are expected to be used in the future, and the energy carriers (liquefied hydrogen, ammonia, organic hydrides) that will be used in large-volume transportation and storage of those fuels.

Recent Topics at IMO ····· *External Affairs Department* ····· 93

This article introduces recent topics discussed at IMO (International Maritime Organization). Due to the spread of COVID-19, IMO meeting has been postponed. This article provides topics, which are expected to be discussed at 75th Marine Environment Protection Committee (MEPC 75) and 102nd Maritime Safety Committee (MSC 102) to be held in November 2020.

Introduction of 4th IMO GHG Study 2020

— Trends of GHG emissions and Carbon Intensity from 2008 to 2012 —

Shinichi HANAYAMA*

1. INTRODUCTION

This report introduces the contents of 4th IMO Green House Gas Study 2020 (hereafter GHG4) by the International Maritime Organization (IMO).

Please note that the content introduced in this report is based on the draft, and the content and conclusions may be modified with the instructions by Marine Environmental Protection Committee (MEPC).

Since 2000, IMO has issued comprehensive study reports on GHG emissions, and this is the fourth report. In drafting the report, an international consortium consists of the experts, who are independent either from administrations and NGOs, should be selected by MEPC. Also, the Steering Committee organized in MEPC, should evaluate the results, and the final draft should be approved by MEPC.

For GHG4, an international consortium consisting of 10 Universities and Institutions led by CeDELFT of the Netherlands won the bid in the summer of 2019. Figure 1 shows the institutes of the consortium, and Table 1 shows the main members of the consortium. NK and National Maritime Research Institute are participating from Japan.

After about half a year of works, a draft report approved by the Steering Committee has been submitted and will be approved at MEPC75 held in November 2020.

NK participated in the consortium not only as of the main author, but also, as a technical director, taking on the role of overall QA / QC.

Figure 1 Institutes consist of the Consortium for GHG4

Table 1 Major members of the international Consortium for GHG4

Dr. Jasper Faber	Project manager Lead author Section 4.5 (emission projections)	CEDelft
Shinichi Hanayama	**Technical director** **Lead author Section 2.9**	**ClassNK**
Dr. Shuang Zhang	Manager Task 1 (emissions inventory) Lead author Chapter 3 (carbon intensity)	Dalian Maritime University
Dr. Paula Pereda	Manager Task 2 (emission projections) Lead author Sections 4.2 and 4.3	University of São Paulo
Dr. Bryan Comer	Lead author Annex A and B	The International Council on Clean Transportation
Dr. Elena Hauerhof	Lead author Section 2.2 and 2.5	UMAS
Wendela Schim van der Loeff	Lead author Section 2.4 and 2.2.4	University College London
Dr. Tristan Smith	Lead author Section 2.7	UMAS University College London
Prof. dr. Yan Zhang	Lead author Section 2.8	Fudan University
Dr. Hiroyuko Kosaka	Lead author Section 4.4	NMRI

* Research Institute, ClassNK

2. RELATIONSHIP BETWEEN IMO'S GHG REDUCTION TARGETS AND GHG4

GHG4 contains the results of 2012-2018 trends of GHG emissions and Carbon Index trends, and as well as CO_2 emission forecasts towards 2050. For application and evaluation of measures to achieve short-term and medium-term targets stated in IMO's GHG reduction strategy, the information based on GHG4 is required. Table 2 shows the relationship between the short-term and medium-term targets in IMO's initial GHG strategy and the contents reported in GHG4.

It should be noted that while the medium-term target targets set only against CO_2, the long-term target targets not only against CO_2 but also GHGs than CO_2.

In this document, Chapter 3 introduces the secular change in emissions in 2012-2018 in relation to the achievement of short-term goals. Then, Chapter 4 introduces the trend of Carbon Intensity from 2012 to 2018. Finally, in relation to the achievement of short-term goals as well. Finally. Chapter 5 introduces future forecasts for 2050. Unless otherwise specified, all subsequent chapters are composed of the executive summary in the draft, and all interpretations and notes by ClassNK are NOT shown in the main texts but only in footnotes.

Table2　Relationship between reduction targets of IMO's GHG reduction strategy and reports in the 4th GHG study

Reduction Targets	Quantitative targets	Information reported in the 4th GHG study
Short-term toward 2030 (only for efficiency)	to reduce CO_2 emissions per transport work by at least 40% by 2030 compared to 2008	The results of Carbon Intensity in 2008 and 2012－2018
Mid-term toward 2050 (both for efficiency and total emissions)	to reduce CO_2 emissions per transport work pursuing efforts towards 70% by 2050 compared to 2008. to reduce the total annual GHG emissions by at least 50% by 2050 compared to 2008	Future CO_2 emission trends of 2019-2050

3. GHG EMISSION TRENDS IN 2012-2018

3.1 Overlook on the trends of GHG emissions

Figure 2 shows the GHG emissions estimated by the historical three IMO GHG Studies and GHG4, the trade statistics by UNCTAD, and the trends of the carbon intensity, only after 2012 which is the period of GHG4. A steady increase in shipping demand[*1] is observed for the maritime trade shown by the orange lines. On the other hand, the survey period of the IMO GHG Study can be divided into the following three eras.

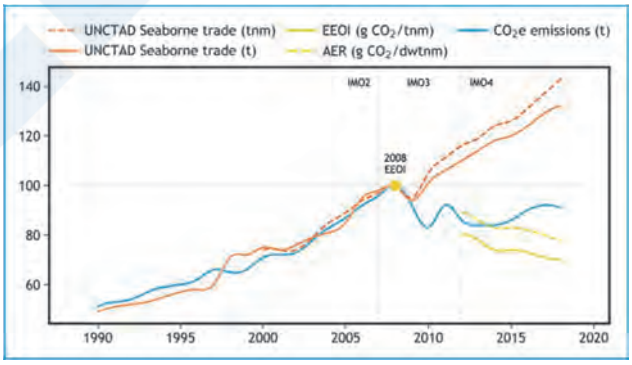

Figure 2　International shipping emissions and trade metrics, indexed in 2008, for the period 1990-2018, according to the voyage-based allocation of international emissions

[*1] According to the statistics by UNCTAD, the transport demands, especialy in ton-mile base, have conpletly revovered from the 2008 financial crisis.

1st Era (1990-2008) Era of increased emissions
when the increase in maritime trade (orange line) and GHG emissions (blue line) showed almost the same growth.

2nd Era (2008-2014) Era of GHG emission reduction
when increased transportation demand and GHG emissions are not linked, and an era of voluntary improvement in carbon intensity.

3rd Era (2014-2018) Era of re-increasing emissions
when GHG emissions are returning to an increasing trend, as carbon intensity continues to improve moderately, but at a slower pace than demand growth (UNCTAD).

3.2 The Method To Distinguish Between International And Domestic GHG Emissions

GHG4 has newly adopted a methodology of splitting between International emissions and Domestic emissions on a voyage basis. This method resulted in assigning each voyage to either international or domestic transport.

On the other hand, the 3rd IMO GHG Study used a different method to distinguish between GHG inventories for International and Domestic shipping. In this methodology, it was assumed that individual ship types and ship type groups were operated by either International and Domestic voyage only. This method relies on assumptions and uniform behaviour among similar ship types and sizes, and GHG4 analysis has shown that the methodology has some drawbacks. However, allow compatibility between the 3rd IMO GHG Study and GHG4, continue to use, and include results from both of these methods wherever possible.

In GHG4, the method used in the latter used in 3rd IMO GHG Study is called Option 1 (ship-based), and the former new method is called Option 2 (voyage-based)*2.

3.3 Trend Of CO_2 Emission In 2012-2018

Table 3 shows the trends in CO_2 emissions from international shipping from 2012 to 2018.

Using the new voyage-based allocation method introduced in Section 3.2, CO_2 emissions from international shipping increased from 701 million tonnes in 2012 to 740 million tonnes (growth with 5.6%) in 2018. When international shipping is allocated on a ship basis, CO_2 emissions increased from 884 million tonnes in 2012 to 919 million tonnes in 2018 (growth with 8.4%). In addition, voyage-based emissions are always smaller than ship-based emissions. Similar to the overall GHG trend shown in Figure 2, emissions have almost recovered after a decline between 2013 and 2014, and are equivalent to the 2008 emission level shown in the bottom line, as reference.

Table 3 CO_2 emissions from international shipping from 2012 to 2018

Year	CO_2 split by Option 2 (Voyage-based)	CO_2 split by Option 1 (Ship-based)
2012	701	848
2013	684	837
2014	681	846
2015	700	859
2016	727	894
2017	746	929
2018	740	919
as refference 2008	794	921

Unit million ton-CO2/year

*2 Based on the definition of International / Domestic spliting in the IPCC guidelines, even if the same vessel is operating in the same country, its CO2 emissions are counted as emissions in thecountry and excluded from International.
For example, when a container ship sailing from Los Angeles Port - Long Beach Port - Yokohama Port - Kobe Port - Los Angeles Port, only the legs of (Long Beach Port-Yokohama Port) and (Kobe-Los Angeles Port) are counted as International, and the legs of (Los Angeles Port - Long Beach Port) and (Yokohama Port - Kobe Port) is counted as domestic.

3.4 Trend Of the Emission of other GHGs than CO_2 In 2012-2018

Figure 3 shows the trends of nitrous oxide (N_2O) and methane (CH_4) as GHG emissions other than CO_2, along with the trends of CO_2 from 2012 to 2018 shown in the previous section, and the emission contribution ratio in 2018. CO_2 remains a major source of emissions, accounting for 98% of total GHG emissions (based on CO_2 equivalents) of International voyages.

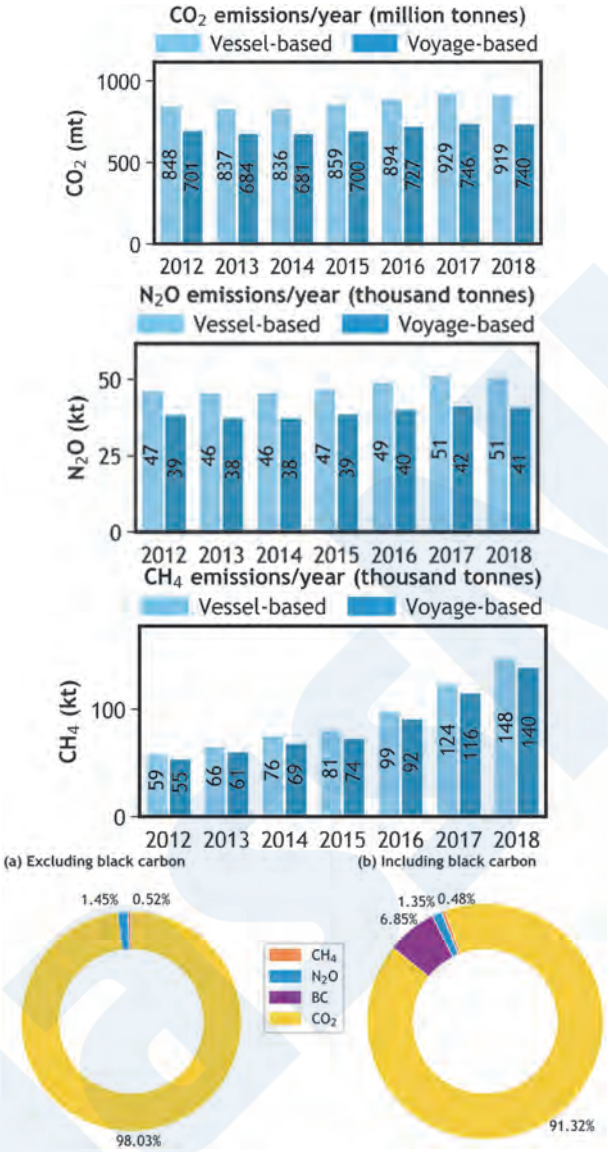

Figure 3 CO_2, N_2O and CH_4 emissions trends in 2012-2018 and emission contribution ratio in 2018

3.5 Trend Of the fuels' Contribution, Used Onboard In 2012-2018

Figure 4 shows the breakdown of fuel consumption by fuels, by ship type from 2012 to 2018. The three ship types; Container ships, bulk carriers, and oil tankers, demand CO_2 emissions from International shipping. Calculated on a voyage-based allocation, including chemical tankers, general cargo ships, and LNG tankers, emissions from these types of vessels account for 86.5% of total emissions from International shipping.

Heavy oil (HFO) continues to be the dominant fuel for International shipping (79% of total fuel consumption in 2018). However, during this study period, significant changes occurred in the fuel mix. While HFO consumption decreased, marine diesel oil (MDO) and liquid natural gas (LNG) consumption increased by 6% and 0.9%, respectively.

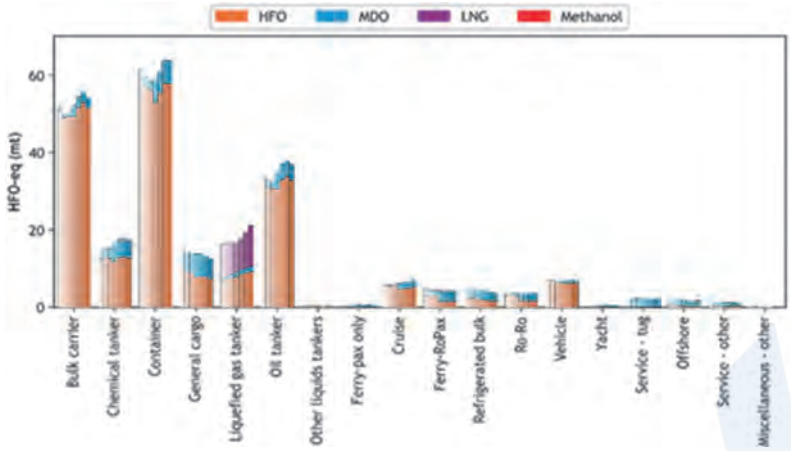

Figure 4 International HFO-equivalent fuel consumption per ship type, according to the voyage-based allocation (Option 2) of international emissions

3.6 Slow Steaming In 2012-2018

Figure 5 shows trends in average operating speed across the three ship types that dominate the inventory of emissions from International shipping. A decrease in operating speed was observed for almost all ship types during the survey period. Oil tankers and container ships saw an increase in average operating speed in 2015 and 2016. This indicates that operating speeds are susceptible to fluctuating markets.

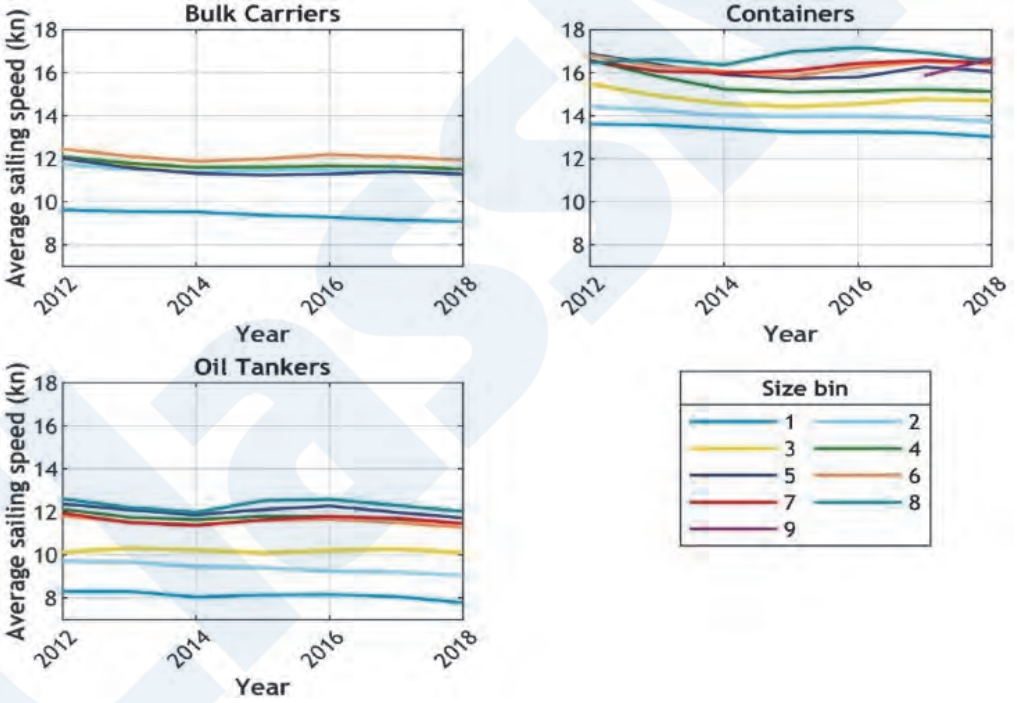

Figure 5 Speed trends for the three highest emitting fleets aggregated (top left) and broken down for each ship type′s size categories (more size bin means more DWT size)

3.7 The Proportion of Time Consumed Between International And Domestic

As shown in Fig. 6, it was found that GHG4 does not operate as International shipping on a voyage basis for all operating hours in all ship types and ship type categories.

For oil tankers, bulk carriers and container vessels, only 20-40% of the operating time are operated as International shipping in the smallest vessel size category. It has been distributed. The largest vessel sizes are up to 70% for general cargo ships, up to 80% for container ships, up to 90% for oil tankers/bulk carriers, and up to 100% for liquefied gas tankers. This observation is the reason why voyage-based emissions are always smaller than ship-based emissions, as shown in Section 3.3.

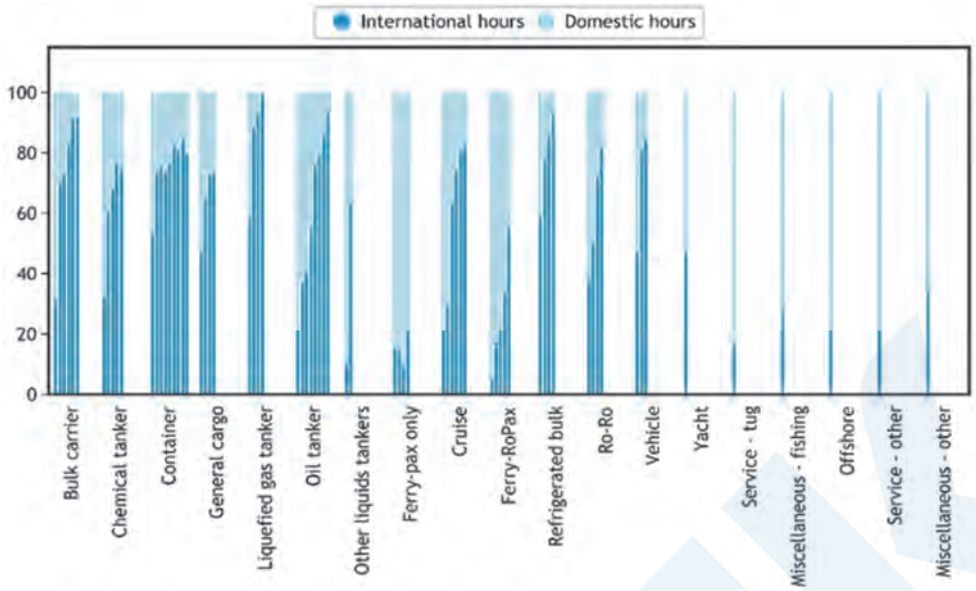

Figure 6　Proportion of time spent on international and domestic voyages on average by ship type and size in 2018 (%), where ship sizes are order small to large

4.　CARBON INTENSITY TRENDS IN 2012-2018

4.1　General description on Carbon Intensity

GHG4 reports the carbon Intensity values for 2008-2012 by the following four calculation methods.

① Energy Efficiency Operational Indicator (EEOI, gCO_2 / t/ nm)
② Annual Efficiency Ratio (AER, gCO_2 / dwt /nm)
③ DIST ($kgCO_2$ / nm)
④ TIME (tCO_2 / hr)

Metrics such as EEOI, AER, DIST and EPEI can be applicable to typical cargo ships and passenger ships, and DIST and TIME and their possible variants are service vessels that do not carry cargo or personnel, More suitable for workboats or fishing boats. In the following, only the calculation results of .1 EEOI and .2 AER will be introduced, which are representative typical carbon intensity calculation.

4.2　Results of Carbon Intensity evaluation

Tables 4 and 5 show the carbon intensity values for the entire International shipping fleet (Table 4 is ship-based, Table 5 is voyage-based). In GHG4, seven types of ships, bulk carriers, oil tankers, container ships, chemical tankers, liquefied gas tankers, general cargo ships, and frozen bulk carriers, were selected as the calculation targets*3. It accounted for about 88% of CO_2 emissions in China and 98% of the actual transportation results on a ton-mile basis. These two tables also show the trend of improvement in carbon intensity calculated compared to 2008 and 2018. Here, the overall improvement tendency*4 is calculated based on the aggregated data, while the improvement rate of the individual is estimated by the regression estimation.

*3 It should be noted that all carbon intensity (CI) in the report are calculated for only seven ship types, regardless of voyage-based or vessel-based.

*4 The numbers in the raw of Overall is a simple calculation of changes in CI values. For example, even if the intensity of individual ships does not change at all, it will be affected by changes in the composition of the of the ship size, such as the increase in size of the fleet. On the other hand, the numbers in the raw of Individual removes the influence of such changes in the composition , extracts only the operational / technical efficiency improvement for each ship size, and calculates the improvement rate.

Table 4 Carbon intensity levels and percentage changes of international shipping (Option 1, vessel-based)

Year	EEOI (gCO_2/t/nm)					AER(gCO_2/DWT/nm)				
	Value	Variation vs 2008		Variation vs 2012		Value	Variation vs 2008		Variation vs 2012	
		overall	individual	overall	individual		overall	individual	overall	individual
2008	17,10	—	—	—	—	8,08	—	—	—	—
2012	13,16	-23,1%	-16,8%	—	—	7,06	-12,7%	-5,6%	—	—
2013	12,87	-24,7%	-18,3%	-2,2%	-2,0%	6,89	-14,8%	-7,1%	-2,4%	-1,7%
2014	12,34	-27,9%	-20,4%	-6,3%	-4,6%	6,71	-16,9%	-7,8%	-4,9%	-2,4%
2015	12,33	-27,9%	-19,0%	-6,3%	-2,8%	6,64	-17,8%	-6,5%	-5,9%	-1,3%
2016	12,22	-28,6%	-18,7%	-7,2%	-2,5%	6,58	-18,6%	-6,4%	-6,8%	-1,4%
2017	11,87	-30,6%	-20,8%	-9,8%	-5,0%	6,43	-20,4%	-8,4%	-8,9%	-3,3%
2018	11,67	-31,8%	-21,5%	-11,3%	-6,2%	6,31	-22,0%	-9,3%	-10,6%	-4,2%

Table 5 Carbon intensity levels and percentage changes of international shipping (Option 2, voyage-based)

Year	EEOI (gCO_2/t/nm)					AER(gCO_2/DWT/nm)				
	Value	Variation vs 2008		Variation vs 2012		Value	Variation vs 2008		Variation vs 2012	
		overall	individual	overall	individual		overall	individual	overall	individual
2008	15,16	—	—	—	—	7,40	—	—	—	—
2012	12,19	-19,6%	-11,4%	—	—	6,61	-10,7%	-4,6%	—	—
2013	11,83	-22,0%	-13,6%	-3,0%	-2,6%	6,40	-13,5%	-6,6%	-3,2%	-2,2%
2014	11,29	-25,6%	-16,2%	-7,4%	-5,5%	6,20	-16,1%	-7,6%	-6,1%	-3,1%
2015	11,30	-25,5%	-14,5%	-7,3%	-3,7%	6,15	-16,9%	-6,2%	-6,9%	-2,0%
2016	11,21	-26,1%	-14,0%	-8,1%	-3,2%	6,09	-17,7%	-5,9%	-7,8%	-1,8%
2017	10,88	-28,2%	-15,9%	-10,8%	-5,4%	5,96	-19,5%	-7,7%	-9,8%	-3,7%
2018	10,70	-29,4%	-17,2%	-12,3%	-7,0%	5,84	-21,0%	-8,9%	-11,5%	-4,8%

As shown in Tables 4 and 5, EEOI and AER values continued to improve largely from 2012 to 2018, compared to 2008 in 2018. The improvement rates have reached about 29% and 21%, respectively. The discrepancy between the value of EEOI and AER was mainly caused by the method of allocating the cargo mass loaded. In either case, the short-term target of 40% improvement has not been achieved by 2018.

Figure 7 and 8 show trends in AER and EEOI for each ship type, estimated on both ship-based (Option 1) and voyage-based (Option 2). As shown in these figures, the carbon intensity values are higher in the order of bulk carriers, oil tankers, and container ships. For container ships, while improvement was seen to be almost constant during the target period, the improvement for other ship types was different, such as slackening.

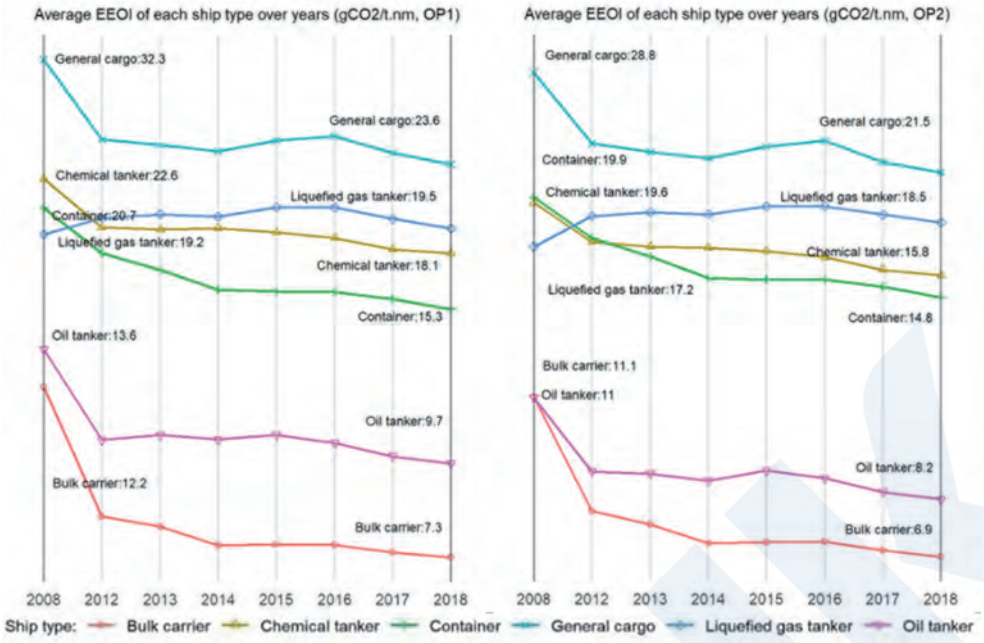

Figure 7　Percentage changes in individual based carbon intensity of international shipping 2012-2018 (Option 1, vessel-based)

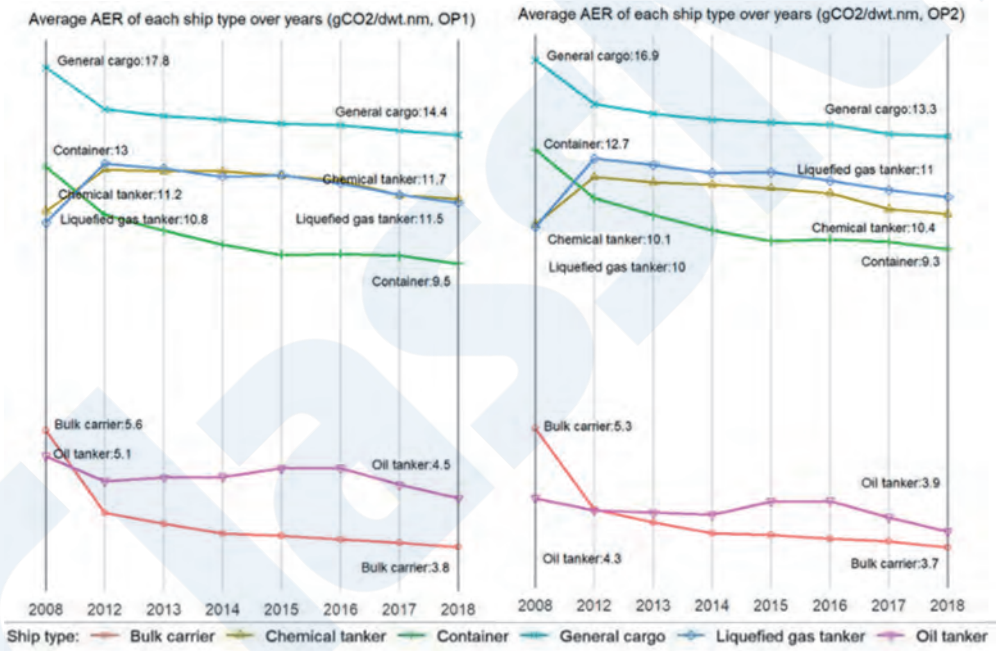

Figure 8　Percentage changes in individual based carbon intensity of international shipping 2012-2018 (Option 2, voyage-based)

5. FORECAST OF CO_2 EMISSION TOWARDS 2050

5.1 General Description

Forecast CO_2 emissions for shipping by 2050. The method for predicting shipping emissions in GHG4 involves the following six work steps:

① Estimate of sea transport demands　of non-energy products:
② Estimate of sea transport demands of energy products:
③ Analysis of the current fleet composition and its activities in 2018
④ Forecast future fleet composition and its activities for 2050

⑤ Predict the future energy efficiency of ships by using the implementation of the current regulations toward 2050 and the Marginal Abatement Cost Curve (MACC), taking into account market-based efficiency improvement.

⑥ Predict total CO2 emissions of shipping sectors by combining the results of Steps .4 and .5 above.

Transport demands depend on three primary factors:

A) The socio-economic scenario taken for the forecast.

The higher the forecast economic growth rate and population growth rate, the higher the sea transportation demands of non-coal dry bulk, unitized cargo such as containers, chemicals, and other products that strongly correlate with economic development.

B) Long-term energy scenario taken for the forecast.

The higher forecast of the fossil fuel consumption onland, the higher the sea transport demands of dry coal bulkers, and oil tankers and gas tankers.

C) Establishing methodologies of the relationship between transport demands and related parameters.

Two methodologies are established to predict the volume of non-energy products transported. The first is a logistics model that statistically analyzes the interrelationship between the world's transportation demands and its related factors over the longest available period, and further predicts the relationship using a logistics curve. The second is a gravity model analysis that analyzes bilateral trade flows and establishes the elasticity of trade between those countries and related factors. In general, GHG4 found that the logistics model approach leads higher transport demands forecasted than the gravity model approach.

For Sea Transport demands of Non-Energy Products and Energy Products, Table 6 summarizes the details of the scenarios that affect the sea transport of non-energy products.

Table 6 Characteristics of transport work demand projections

Non-coal dry bulk, containers, other unitized cargo, and chemicals (Relation between transport work and relevant drivers: Logistics, denoted by _L; Gravitation model, denoted by_G)	**Coal dry bulk,-oil tankers and gas tankers**
Long-term socio-economic scenarios	**Long-term energy scenarios**
SSP1 (Sustainability – Taking the Green Road)	RCP1.9 (1.5°C) in combination with SSP1, SSP2 and SSP5
SSP2 (Middle of the Road)	RCP2.6 (2°C, very low GHG emissions) in combination with SSP1, SSP2, SSP4 and SSP5
SSP3 (Regional Rivalry – A Rocky Road)	RCP3.4 (extensive carbon removal) in combination with SSP1, SS2, SSP3, SSP4 and SSP5
SSP4 (Inequality – A Road Divided)	RCP4.5 (2.4°C, medium-low mitigation or very low baseline) in combination with SSP1, SS2, SSP3, SSP4 and SSP5
SSP5 (Fossil-fueled Development – Taking the Highway)	RCP6.0 (2.8°Cmedium baseline, high mitigation in combination with SSP1, SS2, SSP3, SSP4 and SSP5
OECD long-term baseline projections	

5.2 Transport Demands

As a result of examining the three influential factors shown in the previous section, factor A and factor B were classified into two cases, that is, factor A was designated as SSP2 or OECD shown in Table 6, and factor B was designated as RCP2.6 shown in Table 6. For factor C, the above two methods were applied. From the above, a total of 4 cases were extracted as typical cases. Figure 9 shows the projected sea transportation (expressed as billion ton=miles) from 2020 to 2050 based on these conditions.

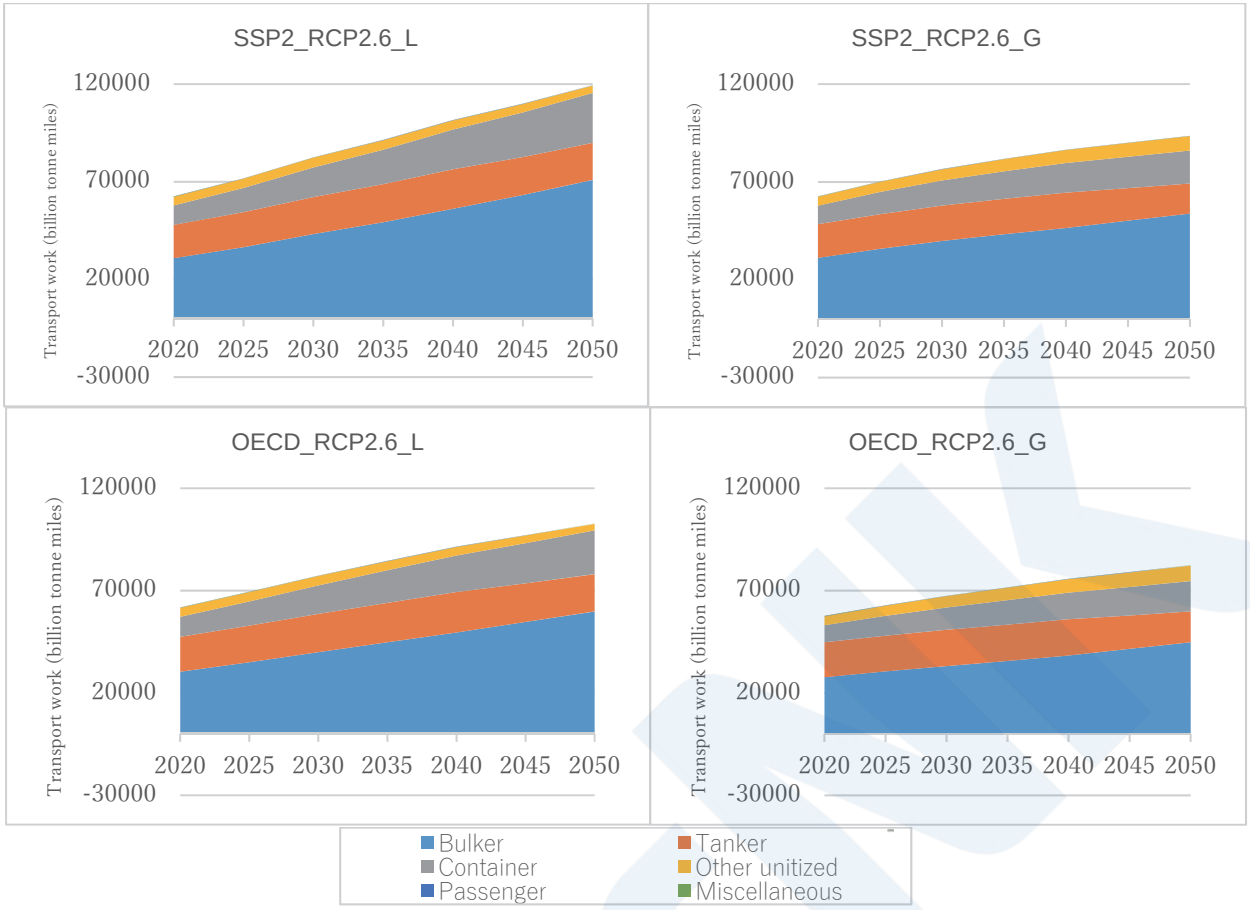

Figure 9　Transport work projections (billion tonne-miles)

Sea transport (ton-miles / year) in 2050 is expected to increase to 190% -290% compared to 2008 (42,000 billion-ton miles / year). In general, forecasts using a logistics analysis model (75% -100% growth in 2050 compared to 2018) have higher growth than forecasts using a gravity model (40% -60% growth compared to 2018). Also, in the SSP2 scenario, where the increase in GDP and population is assumed to be higher, the increase in container transportation is higher than of the other scenarios. On the other hand, some bulkers and tankers may start to decrease in sea traffic toward 2050, depending on the scenario.

Uncertainty remains because the effects of COVID-19 cannot be quantitatively analyzed at this timing, however, in general, as same as the recovery from the economic crisis in 2008 shown in Fig. 2, it is expected that the demands will converge to one of the selected scenarios from the long-term viewpoint toward 2050.

5.3　Marginal Abatement Cost Curve

There are many ways to improve shipping energy efficiency or carbon emission density. GHG4 evaluated the mitigation potentials and costs of 44 technologies for four groups: energy-saving technologies, renewable energy use, alternative fuel use[*5], and ship speed reduction. The curve that rearranges the typical costs of reducing 1 ton of CO_2 for each of the 44 technologies in ascending order is called the Marginal Abatement Cost Curve. The results are shown in Fig. 10.

Assuming that all selected reductions will be applied to all vessels newly built after 2025, it is expected that both of Short-term and Mid-term reduction targets specified in the initial strategy can be achieved.

However, by 2050, the use of alternative fuels will contribute to about 64% of total CO_2 reductions. In other words, it shows that the use of alternative fuels is theoretically essential to achieve the medium-term target. Note that the alternative fuel marginal reduction cost curve (MACC) is highly dependent on the projected price of zero-carbon fuels.

[*5] The alternative fuel does not include LNG. the alternaticve fuels mean carbon-free fuels, such as hydrogen, ammonia, or a fuel that can be regarded as carbon-neutral such as synthetic methane / synthetic methanol.

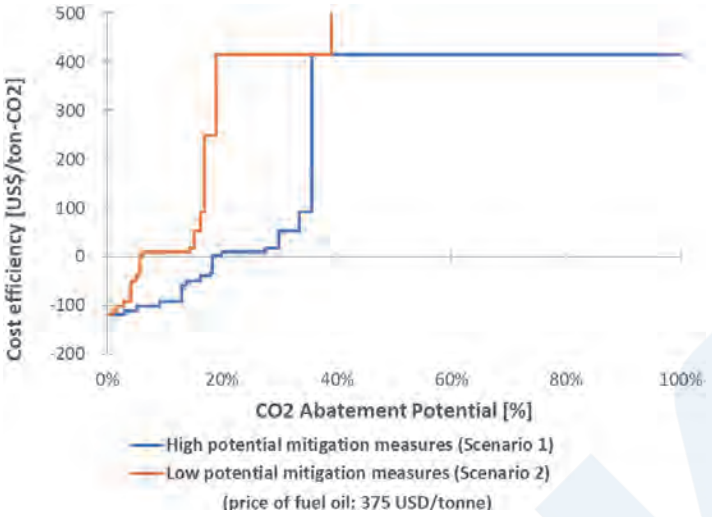

Figure 10　Marginal abatement cost curve for 2050

5.4　CO_2 emission Forecast toward 2050

Figure 10 shows the CO_2 forecast results from 2020 to 2050 in the so-called BAU (Business As Usual).

In GHG4, BAU defines in the shipping sector that no new regulations affecting energy efficiency or carbon intensity will be adopted*6.

Figure 11 shows the total CO_2 emissions from all vessels in the six long-term scenarios shown above. In these BAU scenarios, shipping emissions are projected to increase from 1 billion tonnes of CO_2 in 2018 to 1 billion to 1.5 billion tonnes of CO_2 in 2050. This means an increase of 0% to 50% compared to the 2018 emissions, and falls within the range of 90% to 130% compared to the 2018 emissions.

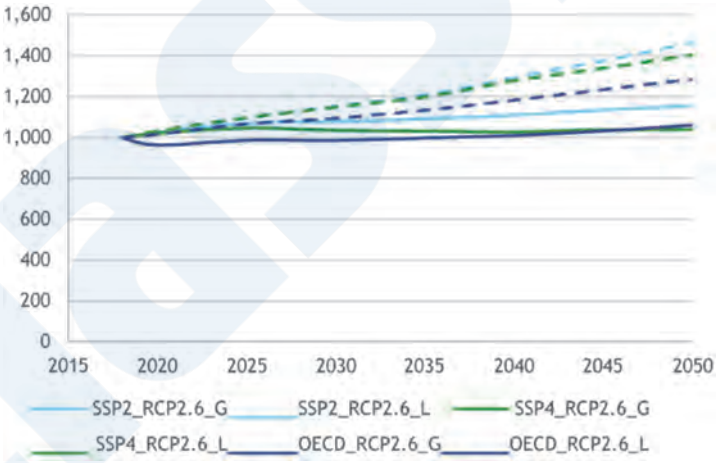

Figure 11　CO_2 emission forecasts for 2050

These differences in CO_2 emission forecasts are due to differences in transport volume forecasts, which means differences in socio-economic forecasting methods and independent variables such as transport demands, GDP per capita, population, and primary energy demands. This is due to differences in the scenarios are established*7.

The emissions shown in Fig. 10 are the total of all shipping, including domestic and fishing vessels. The share of domestic and international voyages is expected to remain unchanged*8.

*6 The effects up to EEDI Phase 3 are incorporated. On the other hand, the effect of EEXI and the rating system using CII, which are under discussion, is not incorporated.

*7 In the 3rd IMO GHG Study, two scenarios (the amount of LNG diffusion) were prepared for the energy utilization composition, but in this 4th Study, the energy utilization composition on the ship side is four maritime trades. In GHG4 assumed that the energy mix towards 2050 is constant as 2018.

*8 This implies that GHG (CO_2 equivalent) from international shipping will also increase in the range of 90% to 130% of the 2008 level.

It is too early to quantitatively assess the impact of COVID-19 on emission forecasts, but it is clear that emissions in 2020 and 2021 will decline significantly due to the decline in sea transport. On the other hand. In the long run, as explained in Section 4.3, emissions in the coming decades will be at most a few percent lower than expected, depending on the recovery in transport. Overall, the impact of COVID-19 in 2050 is likely to be less than the projected range of emissions due to the uncertainty of this scenario.

6. SUMMARY OF THE CONTENTS

① With respect to CO_2 emissions trends from the entire shipping sectors (International, Domestic, and fishery), CO_2 emissions in 2012 were 692 million tons, and CO_2 emissions in 2018 were 1.056 billion tons, within an increase of 9.3% during the period.

② The representative Greenhouse gas (GHG) emissions. ie. carbon dioxide (CO_2), methane (CH_4), and nitrous oxide (N_2O) increased from 977 million CO_2 equivalent tons in 2012 to 1076 million CO_2 equivalent tons in 2018. It has increased to 100 million CO_2 equivalent tons, an increase of 9.6% of 2012.

③ With respect to the CO_2 emissions of International shipping split from the whole shipping sectors mentioned above, when the ship-based allocation method is used, the CO_2 emissions of ocean shipping increased from 701 million tons in 2012 to 740 million tons (increase by 5.6%) in 2018. On the other hand, when the voyages-based allocation method is used, CO_2 emissions increased from 884 million tonnes in 2012 to 919 million tonnes in 2018 (increase by 8.4%).

④ The difference between the two allocation methods is caused from the observation that the ratio of the time operating in the same country will reach to >10% even of the largest ship size in each ship type.

⑤ From 2012 to 2018, the Carbon Intensity of the international sectors had been improved. On a voyage basis, there was a 21% improvement in AER and a 29% improvement in EEOI over 2008. However, the improvement is not sufficient to achieve the 40% reduction target by 2030. While more than half of the improvements have been achieved by 2012, the pace of improvement has slowed since 2015.

⑥ Emissions in 2018 were about 90% in 2008, however, based on long-term economic and energy mix scenarios onlands, CO_2 emissions are expected to increase to 90-130% by 2050 compared to 2008. In order to achieve the midterm reduction target, it is not sufficient to improve efficiency by EEDI or voluntary slow steaming, and it is crucial to introduce low/zero-carbon fuels to this sector.

ACKNOWLEDGMENT

ClassNK would like to express our appreciation to all the members of the consortium, who accomplished this project in a quite short period, especially to Dr. Jasper Faber of CeDELFT who led the consortium.

REFERENCES

1) IMO GHG Study 2020 – Final report. IMO, MEPC 75/7/15
The document is available from the URL below;
https://docs.imo.org/

Roadmap to Zero Emission from International Shipping

Marika NISHIMURO *

1. INTRODUCTION

According to the study on greenhouse gas (GHG) emissions from international shipping conducted by the International Maritime Organization (IMO) in 2014, total CO_2 emissions from international shipping in 2012 was approximately 800 million tons, around 2.2% of global emissions and comparable to those from countries such as Germany and Brazil. Its emissions are expected to increase amid the growth of the world economy.

Measures to reduce global GHG emissions are discussed at the conferences under the United Nations Framework Convention (UNFCCC). However, GHG emissions from international transport sector, namely international shipping and aviation operating beyond national borders, are difficult to be controlled and allocated to each country by nationality of the ship or aircraft, or by the country of a company which operates them. Thus, actions to reduce emissions from these sectors are not compatible with the country-specific reduction measures pursuant to the UNFCCC framework. For these reasons, discussions on reduction measures of these sectors have been delegated to the United Nations Special Agencies, the IMO and the International Civil Aviation Organization (ICAO), respectively.

In November 2016, the Paris Agreement under the UNFCCC was entered into force aimed at achieving net zero emission as the long-term goal, that is, “a balance between anthropogenic emissions by sources and removals by sinks of greenhouse gases” “in the second half of this century.” As to international shipping, the IMO adopted “the Initial Strategy on reduction of GHG emissions from ships” (hereinafter referred to as “the IMO Strategy”) in 2018 setting the GHG reduction targets: (i) to reduce carbon intensity (i.e. CO_2 emissions per transport work) of international shipping by at least 40% by 2030 compared to that in 2008 (“the 2030 target”); (ii) to reduce the total annual GHG emissions from international shipping by at least 50% compared to those in 2008 (“the 2050 target”); and (iii) to phase out GHG emissions as soon as possible in this century.

The international shipping sector had already making efforts to reduce the emissions from ships prior to the adoption of the IMO Strategy. For example, it had introduced the mandatory energy efficiency design index (EEDI) regulations for new ships and gradually strengthened these rules. However, to achieve the targets under the IMO Strategy, especially the targets for 2050 and beyond, it is necessary not only to continue these ongoing efforts but also to introduce and speed up actions that go beyond the conventional ones, such as transition from conventional fossil fuels to low-/zero-carbon fuels and introduction of innovative technologies.

As a one of major players in global shipping and shipbuilding industries, Japan should take the lead in the global actions to tackle the climate change in a manner that stimulates the innovation and sustainability of global maritime sector. Under these circumstances, the Shipping Zero Emission Project (hereinafter referred to as “the Project”) was launched in 2018 in collaboration with the industrial, academic, and public sectors with the support from the Nippon Foundation. The Project carried out a research to clarify necessary actions conducted by the maritime sectors and the direction to be followed by the future ships, and published “the Roadmap to Zero Emission from International Shipping” in March 2020 as a long-term strategy in order to provide materials for maritime industries in determining and implementing the concrete actions toward the GHG emissions reduction.

Toward achieving the 2030 target, the Maritime Environment Protection Committee (MEPC) of the IMO have been discussing the short-term measures. At its 75th session held in November this year, in order to improve the operational efficiency of existing ships, the package of the energy efficiency existing ship index (EEXI) regulations and operational carbon intensity rating based on fuel oil consumption was agreed with a view of adoption at the 76th session next year. These regulations will enter into force at the beginning of 2023 at the earliest.

In this article, focusing on the measures to be taken to achieve the targets for 2050 and beyond, the GHG reduction scenarios

* Japan Ship Technology Research Association (JSTRA)

(emission pathways) and the timelines and details of the technological development and the environmental preparation including the development of international rules (the roadmap) considered in the Project are introduced.

2. EMISSION PATHWAYS FOR ACHIEVING THE 2050 TARGET

2.1 Perspectives on Achieving Reduction Targets

It is yet challenging to achieve the 2050 target only by means of design and operational improvement regulations on new and existing ships, while the 2030 target will be met by the EEDI and EEXI regulations mentioned above.

Figure 1 shows one of the estimated business-as-usual (BAU) emissions from international shipping up to 2050 calculated by the Project, which uses a socioeconomic scenario in which the international seaborne trade increases the most. BAU emissions is defined as the amount of CO_2 emissions in the future assuming that no reduction measures will be taken from 2008 onward, that the state of marine transport (ship speed, ship type and size distribution, etc.), design technologies, fuels and others will be maintained, and that the average energy efficiency will remain unchanged.

Based on this estimate, required improvement in average energy efficiency of international shipping by the year of 2050 is approximately 80% from 2008 level to meet the 2050 target. Therefore, it is necessary to start introducing 80% or more efficient ships from around 2030, on a simplified assumption that ocean-going ships have a service life of 20 years. If they have a longer life, efforts should be made towards introducing ships with 90% or greater efficiency improvement by 2030. Japan, as one of the major players in global shipping and shipbuilding sectors, should endeavor to introduce such ultra-low or zero emission ships even earlier than 2030. In addition, measures taken to achieve the 2050 target should be part of holistic framework/approach that leads to achieve the long-term target, namely zero emissions as early as possible in this century.

In light of the matters mentioned above, potential alternative fuels and technological options were narrow down, and GHG emission pathways to achieve the 2050 target were developed accordingly.

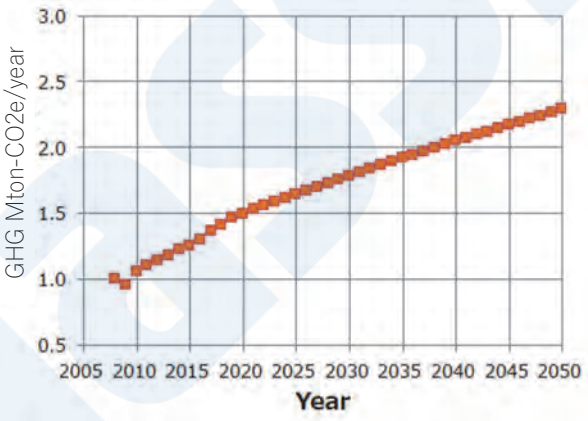

Figure 1 BAU emissions from international shipping (index: the emissions in 2008 = 1)

2.2 Options for Alternative Fuels and Abatement Technologies toward the 2050 Target

As GHG emission reduction measures, the combination of various technologies and elements can be considered, such as use of low/zero-carbon fuels, slow steaming, design efficiency improvement, including the use of wind power assistance, and carbon capture and storage so as to prevent CO_2 emissions from being released to the atmosphere.

In the Project, considering the conditions mentioned in section 2.1, the followings were identified as the main options which “have a potential to improve energy efficiency by 90% or more in 2028 compared to the 2008 level” and “are capable of achieving zero emission from international shipping in the long term”: LNG, Hydrogen, Ammonia, Carbon-recycled methane, onboard carbon capturing system, wind propulsion, and battery propulsion system. Table 1 shows the advantages and issues related to each fuel and technology. In this study, fuel cells using alternative fuels have been categorized as having relatively low potential for practical application to a main source of propulsion power at the time of 2028 because there are larger barriers to the application in large ocean-going ships compared to direct combustion.

Table 1 Main options for alternative fuels and emission reduction technologies

	Advantages	Issues
LNG	• Already in practical use (stored at -163C).	• Reduction of CO_2 emissions is limited (26% reduction compared to HFO). • Methane slip (approx. 28 times higher global warming potential averaged over 100 years compared to that of CO_2).
Methanol	• Already in practical use.	• Reduction of CO_2 emissions is limited (10% reduction compared to HFO).
Hydrogen	• No CO_2 emission onboard.	• Storage stability (-253 in liquid state). • Combustion control (flammability) • Large fuel volume, approx. 4.5 times that of HFO.
Ammonia	• No CO_2 emission onboard.	• Toxicity. • Low flammability. • N_2O emissions (approx. 260 times higher global warming potential).
Biomethane, Carbon-recycled methane*	• Potential to be treated as carbon neutral. • LNG-fueled ships and infrastructure for LNG can be used as these fuels are chemically identical to LNG.	• No explicit provisions in IPCC guidelines defining carbon-recycled methane as carbon neutral. • Methane slip.
Onboard CO_2 capturing	• Already in practical use in the onshore sectors. • Reduction of onboard emissions considerably without using low/zero-carbon fuels.	• Necessary to reduce the size of CO_2 capturing and storage system. • Capture rate should be increased. • Onshore CO_2 reception facilities (storage, recycling) need to be developed.
Wind propulsion	• Zero emission onboard.	• Instability. • Effect depends on weather conditions and selected course.
Battery propulsion	• Implemented as the main propulsion system in small boat.	• Low weight and volumetric energy density. • Longer charging time than conventional fuel bunkering. • Necessary to replace battery periodically.

*Methane produced from hydrogen and captured CO_2.

2.3 Emission Pathways for Achieving the 2050 Target

Taking into account these shortlisted options in section 2.2, GHG emission pathways, aligned with the GHG reduction targets set out in the IMO Strategy, are developed.

Given that alternative fuels, such and hydrogen and ammonia and technologies may be introduced in or after 2028, LNG fuels alone are the only practicable option to address GHG emissions reduction by means of fuel transition in international shipping for the time being. It is therefore considered that the expansion of the use of LNG fuels will be a common trend to all emission pathways. On the basis of this trend, the following two major possibilities of fuel shift in international shipping are examined while acknowledging uncertainties in future energy supply scenarios.

- Emission pathway I “a fuel shift from LNG to carbon-recycled methane”
- Emission pathway II “the expansion of hydrogen and/or ammonia fuels”

In both pathways, the following assumptions are used: (i) hydrogen fuels, ammonia fuels and onboard CO_2 capturing technology would be introduced from 2028 onwards; (ii) the newbuilding of ships using petroleum-based fuel such as heavy fuel oil would gradually decrease and that no such ships would be built in or after 2035 with the wide spread use of LNG-fueled ships; (iii) the 2030 target of carbon intensity reduction by 40% will be achieved, followed by an extra 5% reduction by means of technical and operational improvement by 2050; and (iv) nearly 2% of the entire fleet engaged in international shipping will adopt wind or battery propulsion.

GHG emission and fuel consumption trends in international shipping under the two emission pathways are examined in the following section.

2.3.1 A Fuel Shift from LNG to Carbon-recycled Methane

In this pathway, use of biomethane or carbon-recycled methane, which have potential to be considered as carbon-neutral, is expanded using the infrastructure for LNG fuels that have been already widely used as a marine fuel. In addition, it is assumed that construction of infrastructure for hydrogen and ammonia fuels will not advance considerably despite the increased use of LNG-fueled ships and the expansion of infrastructure for supplying LNG fuels.

Left side of figure 2 shows the BAU emissions (the top broken line), GHG emission pathway achieving the 2050 target (the bottom solid line), and energy consumption by fuel in 2050. In this emission pathway, carbon-recycled methane will make the greatest contribution to GHG emissions reduction besides the reductions achieved by the introduction of energy saving technologies and operational improvements. In this case, nearly 75% of energy consumption in international shipping in 2050 will be supplied by LNG fuels, carbon-recycled methane, or biomethane fuels while around 10% will be by hydrogen or ammonia fuels. In addition, some 20% of the LNG-fueled ships will introduce onboard CO_2 capturing system. These set of measures enable the achievement of the 2050 target. In figure 2, carbon-recycled methane and biofuels are treated under the same category (right orange) as both are carbon-neutral fuels.

2.3.2 Expansion of Hydrogen and/or Ammonia Fuels

In this pathway, the possibility of increased use of either hydrogen or ammonia fuels, or both, which generate no CO_2 at all when burnt, was examined in addition to the continuous use of LNG fuels. It is assumed that the development of ship technology will be advanced and fuel supply will be increased for hydrogen or ammonia fuels, or for both. However, since the introduction of ships using these fuels is presumed to commence around 2028, it is considered more realistic to envision that the use of currently available LNG fuels will also increase to some extent. In addition, it is envisioned that nearly 5% of the ships engaged on the international shipping will introduce onboard CO_2 capturing. Furthermore, it is to be noted that this pathway assumes that hydrogen and/or ammonia fuels will be sufficiently supplied.

Right side of figure 2 shows the BAU, GHG emission pathway achieving the 2050 target and energy consumption by fuel in 2050 in this pathway. It will be possible to reach the 2050 target on the condition that hydrogen or ammonia fuels account for approximately 45% of energy consumption in international shipping in 2050 and LNG fuels some 35%, while carbon-recycled methane or biomethane fuels account for around 7%. As shown in table 1, hydrogen and ammonia have their respective advantages and disadvantages and at this stage it is difficult to tell which of them is superior.

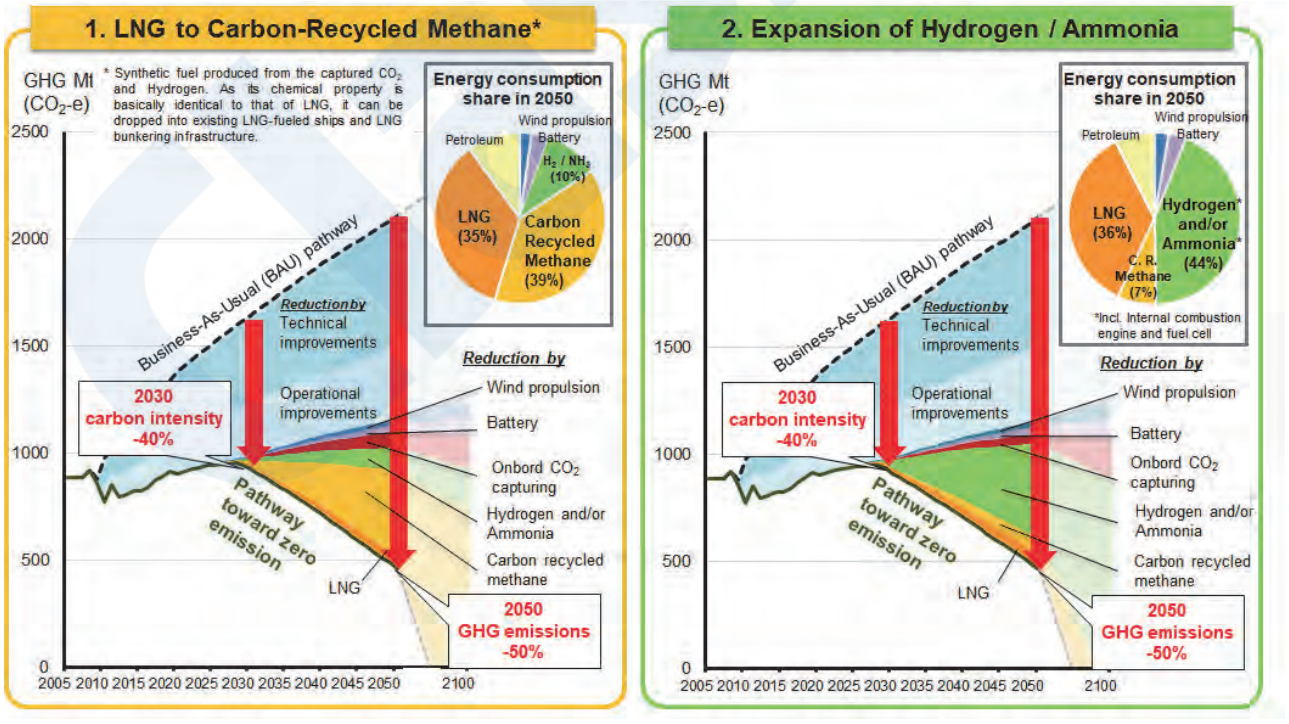

Figure 2 GHG emission pathways for achieving the 2050 target

3. CONCEPT DESIGNS FOR ULTRA-LOW OR ZERO EMISSION SHIPS

In the GHG emissions pathways in chapter 2, it is envisioned that the ultra-low or zero emission ships achieving nearly or more than 90% reduction of GHG emissions compared to the 2008 level (hereafter "Zero Emission Ships") to be introduced by 2028. The Project created the concept designs for the following four types of Zero Emission Ships: (i) hydrogen-fueled ships; (ii) ammonia-fueled ships; (iii) onboard CO_2 capturing ships; and (iv) super-efficient LNG-fueled ship, envisioning 20,000 TEU container ships or 80,000 DWT bulk carriers as base ships, and identified possibilities as well as challenges in introducing the Zero Emission Ships from technical and other perspectives.

3.1 Hydrogen-fueled Ship

The designs were based on the assumption that i) liquefied hydrogen for the purpose of bunker fuel could be supplied at five major ports located around the world, in Europe, the Middle East, Australia, Japan and South America, that ii) the 80,000 DWT bulk carrier would have a one-way cruising range of 7,000 nautical miles (NM) while the 20,000 TEU container ship would have 11,500 NM, and that iii) a dual fuel reciprocating engine would be used as the main engine. Table 2 shows the principal characteristics for the hydrogen-fueled container ships (20,000 TEU). In developing the concept design, the following technical issues which should be resolved in introducing the liquified hydrogen-fueled ships were identified: development of hydrogen-fueled engines and fuel supply systems, upsizing of fuel tanks, thermal protection systems, and measures to prevent hydrogen leakage.

Table 2 Principal characteristics of the hydrogen-fueled 20,000 TEU container ship

Total length	399.90 m
Ship length	383.00 m
Total width	61.50 m
Depth	33.00 m
Draft	
Designed draft	14.50 m
Full load summer draft	16.50 m
Liquefied hydrogen tank	30,000 m^3
Number of containers	21,000 TEUs
Freezing container plugs	1,100 TEUs
Designed speed	22.5 knots
Cruising distance	11,500 NM
Main engine	1 unit
Maximum output	60,000 kW x 80 rpm
Normal output	54,000 kW x 77 rpm
Power generator	3 units
	5,000 kW

3.2 Ammonia-fueled ship

The design was based on the assumptions that i) the ship would serve Japan-Australia route, and that ii) a dual fuel reciprocating engine using a mechanism of injecting methanol, LPG or other liquid fuels as a pilot fuel would be used as a main engine. Given that ammonia fuels were flame-retardant, the engine was equipped with a pilot fuel injection valve to control ignition. With the pilot fuel considered, the ship was expected to reduce CO_2 by 91.9% compared to conventional ships of the same type and size. Table 3 shows its principal characteristics.

In developing the concept design, the following technical issues which should be resolved in introducing the ammonia-fueled ships were identified: the risks of ammonia's toxicity and other properties, the control of ammonia leakage, release to the atmosphere in the event of an emergency, NOx emissions, N_2O emissions and other issues.

Table 3　Principal characteristics of Ammonia-fueled 80,000 DWT bulk carrier

Total length	233.00 m
Ship length	225.5 m
Total width	32.26 m
Depth	20.10 m
Draft	
Designed draft	12.20 m
Full load summer draft	14.45 m
Deadweight	81,000 tons
Ammonia tank	1,550 m^3
Designed speed	14.2 knots
Main engine	1 unit
Maximum output	9,660 kW
Normal output	7,052 kW
Power generator	3 units
	600 kW

3.3　Onboard CO_2 Capturing Ship

The design was based on assumptions that i) the ship would operate on routes between the Far East and Europe, that ii) a dual fuel reciprocating engine using methanol fuels would be used as main engine, and that iii) the ship is equipped with an onboard CO_2 capturing system using the liquid amine absorption method and CO_2 storage tanks. The systems are expected to capture 85.7% of CO_2 emissions, and has potential to improve the capturing rate to 90% or higher subject to further technological development. Table 4 shows its principal characteristics.

In developing the concept design, specific technical issues related to the CO_2 capturing and liquefaction systems which should be resolved in introducing the onboard CO_2 capturing ships were identified.

Table 4　Principal characteristics of 20,000 TEU container ship with an onboard CO_2 capturing system

Total length	399.90 m
Ship length	383.00 m
Total width	61.00 m
Depth	33.50 m
Draft	
Designed draft	14.50 m
Full load summer draft	16.00 m
Number of containers	21,300 TEUs
Methanol tank	13,200 m^3
CO_2 tank	6,400 m^3 x 2 sets
Impact on loading capacity	-1,820 TEUs
Designed speed	21.8 knots
Main engine	1 unit
Maximum output	55,000 kW
Normal output	49,500 kW
Power generator	5 units
	6,870 kW

3.4　Super-efficient LNG-fueled Ship

The project developed concept designs for a bulk carrier and a container ship using a combination of LNG fuel and other technologies to achieve energy efficiency improvement by more than 80% compared to the 2008 level. These designs assumed introduction of a hybrid contra-rotating propeller, hull form improvements, speed optimization, ship upsizing, electric propulsion and the application of LNG fuels and other innovative energy saving technologies, such as the wind propulsion system and the air lubrication system. In accordance with the IMO's EEDI calculation guidelines, these concept designs would achieve 86% improvement compared with the average efficiency of conventional ships. Table 5 shows the principal characteristics for a balk carrier.

Table 5 Principal characteristics of the super-efficient LNG-fueled bulk carrier

Total length	229.00 m
Ship length	225.00 m
Total width	42.00 m
Depth	20.60 m
Draft	
Designed draft	12.20 m
Full load summer draft	14.45 m
Deadweight	102,000 tons
LNG tank	3,800 m^3
Designed speed	11.5 knots
Propulsion motors	2 units
Rated output	1,750 kW

4. ROADMAP TO ZERO EMISSION FROM INTERNATIONAL SHIPPING

In Chapter 2, it was identified that energy efficiency improvement by 80% or more by 2050 compared to 2008 level would be needed in order to achieve the 2050 target of the IMO Strategy. Then the two emission pathways were developed: Emission Pathway I "a fuel shift from LNG to carbon-recycled methane" and Emission Pathway II "expansion of hydrogen and/or ammonia fuels" as explained in section 2.2. On this basis, the Project considered actions which would need to be taken by the industrial, academic, and public sectors, as well as timelines for these actions. These actions and timelines are put together as a roadmap to zero emission from international shipping.

Figure 3 outlines the roadmap. It designates the period from 2028 to 2030 as the milestone to start introduction of Zero Emission Ships (ultra-low or zero emission ships capable of achieving nearly or more than 90% reduction of GHG emissions compared to the 2008 level) in order to achieve the 2050 target. To realize construction and operation of Zero Emission Ships by the milestone, research, development and demonstration of new technologies should be accelerated, and simultaneously international regulatory framework and standards should be reviewed or developed. Then, it would also be necessary to develop measures to incentivize adoption of Zero Emission Ships, as well as global supply chains and infrastructures for low-/zero-carbon alternative fuel in order to facilitate wide spread of them.

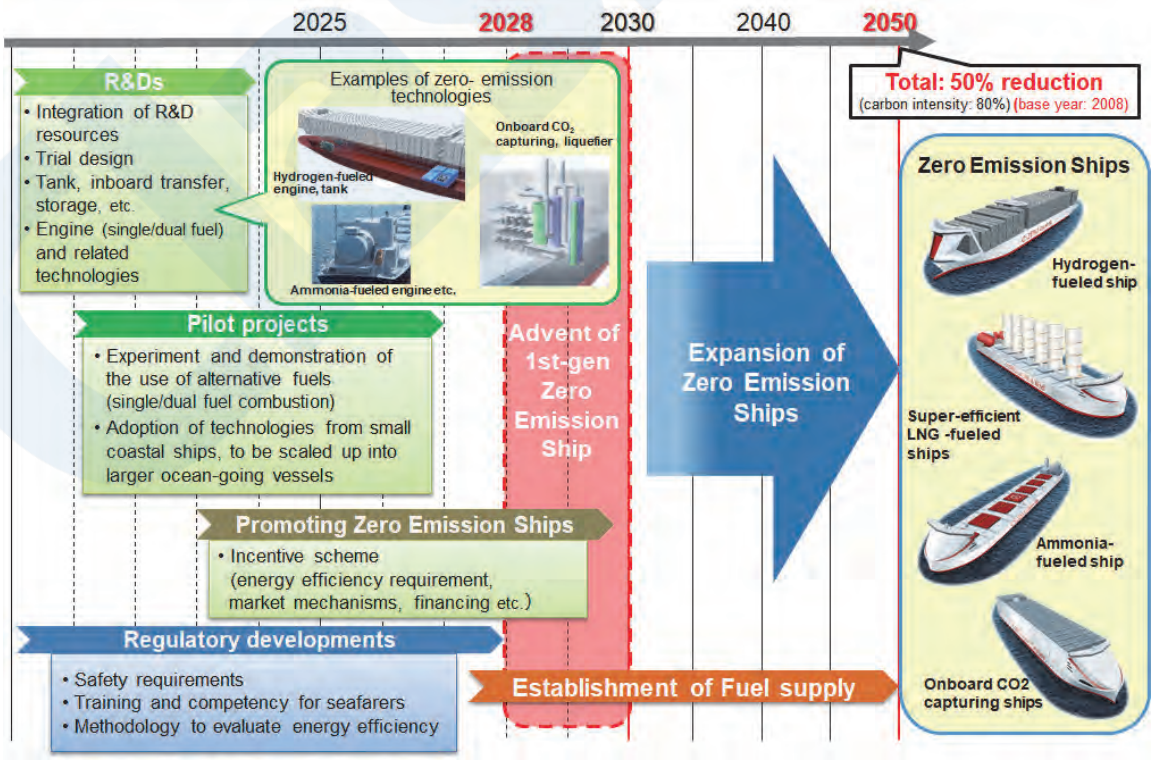

Figure 3 Outline of the roadmap to zero emission from international shipping

5. CONCLUSION

Potential of zero emission from international shipping in the future depends on intricately entangled and uncertain factors, such as technological developments, supply capacity and availability of alternative fuels, and their costs, which cannot be precisely predicted at this stage. Under these circumstances, based on information currently available, the Project analyzed and explored possible emission pathways that enable international shipping to meet the GHG reduction target set out in the IMO Strategy. It then developed detailed plan of actions, including technological developments and regulatory development that would be necessary to realize the pathways and presented them in the form of a Roadmap.

The Roadmap needs to be revised continuously through reviewing and narrowing down the optional pathways and actions taking into account updated circumstances and progresses. Therefore, the Project would continue vigorous activities in and after 2020, supporting all stakeholders to accelerate actions toward the introduction of zero emission ships in 2028 and achieving GHG reduction targets.

REFERENCE

“Roadmap to Zero Emission from International Shipping” can be found at the following link:
https://www.mlit.go.jp/common/001354314.pdf

Trends in Sustainable Finance with Potential Impacts on the Shipping Industry

Masao YAMASAKI*

1. INTRODUCTION

According to the International Monetary Fund (IMF), "Sustainable finance incorporates a large array of environmental, social, and governance (ESG) principles that are becoming increasingly important for borrowers and investors. [1)]"

The website of GREEN × GLOBE Partners [2)] provides the following commentary, which may be more understandable for the readers of this article: Although 'money has no color,' a movement that seeks to contribute to building a sustainable society by circulating money with a color, most notably, 'green,' but also including terms like 'social' and 'sustainability,' is now occurring around the world. This flow of financing aimed at building a sustainable society is called 'sustainable finance.'

This article introduces trends in sustainable finance, which is gradually becoming widespread in the shipping industry.

2. OVERVIEW OF PRINCIPLES AND STANDARDS RERATED TO SUSTAINABLE FINANCE WITH POTENTIAL IMPACTS ON THE SHIPPING INDUSTRY

This chapter presents an overview of the sustainable finance that may have impacts on the shipping industry, or more concretely, principles and standards for evaluating whether the use of funds is sustainable in fund-raising by shipping companies.

2.1 Equator Principles (EPs)

The Equator Principles (EPs) is a set of voluntary guidelines adopted by the financial industry for assessing and managing the impacts of projects on the natural environment and regional society ("environmental and social risks") when financial institutions provide financing for large-scale projects such as infrastructure construction.

The Equator Principles was adopted in 2003 by 10 leading banks in Europe and the United States. As of the end of August 2020, a total of 109 financial institutions in 38 countries, including 8 institutions in Japan, had adopted the EPs.

Although the EPs framework is not applied to financing for ship construction in general, as its object is large-scale projects, it has been used as reference when drafting the principles and standards described below.

2.2 Principles and standards for financing

The methods used by shipping companies to procure external funding include loans from financial institutions and issuance of corporate bonds, among others. In recent years, there has been heightened interest in whether the use of loans and funds raised by issuing corporate bonds is "green" or not, that is, whether appropriate consideration is given to the environment or not.

The following introduces principles and standards for assessing whether the use of funds satisfies environmental considerations or not when a company receives financing from a financial institution.

2.2.1 Green Loan Principles (GLP)

The Green Loan Principles (GLP) are voluntary guidelines that were established to promote the development and integrity of the green loan market by clarifying the methods by which loans may be categorized as "green." The GLP was established in 2018 by the Loan Market Association (LMA), the Asia Pacific Loan Market Association (APLMA) and the Loan Syndications & Trading Association (LSTA) based on the Green Bond Principles described in the following, and the most recent version was published as a 2020 version.

The actual record of GLP loans in Japan includes financing for the construction of a chemical tanker using methanol fuel [3)] and a LNG bunkering ship [4)]. Third-party reviews of these loans found that they satisfied the standards required in the Green Loan Principles.

* Intelligence & Strategy Team, ClassNK

2.2.2 Poseidon Principles

The Poseidon Principles was established in 2019 by 11 major financial institutions in Europe and the United States as a tool for quantitative assessments of the degree of contribution to reduction of greenhouse gas (GHG) emissions in international shipping of ship loans by financial institutions.

Since the Poseidon Principles was established, the number of participating financial institutions had increased to 18 as of the end of August 2020, and in March 2020, Japan's Sumitomo Mitsui Trust Bank became the first financial institution in Asia to join. The balance of ship loans of these 18 financial institutions is estimated at a total of US$150 billion, which is equivalent to about 30% of the world's total ship loan balance.

The Poseidon Principles sets the global carbon intensity trajectory (Fig. 1) for annual CO_2 emissions by ship type and size so as to "reduce the total GHG emissions from international shipping by at least 50 % by 2050 compared to 2008 levels," which is the target in the Initial IMO Strategy on Reduction of GHG Emissions from Ships adopted by the International Maritime Organization (IMO) in 2018. Under this framework, the climate change achievement score ("portfolio climate alignment") of the ship loan portfolios of each signatory financial institution is obtained by calculating the deviation between the annual CO_2 emissions (AER: annual emission ratio) of ships and the standard value (trajectory value), and assigning weighted values based on the debt outstanding for the ships concerned.

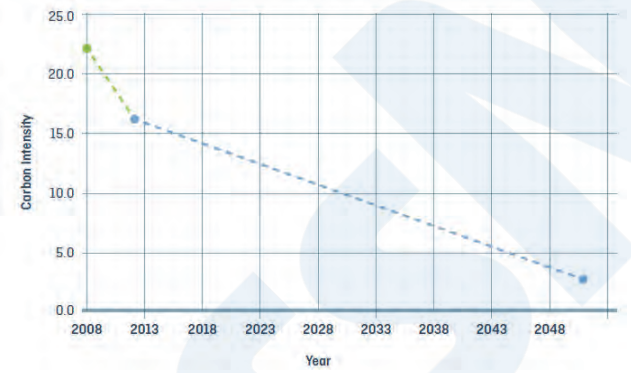

Figure 1 Global carbon intensity trajectory under the Poseidon Principles [5)]

All signatories are required to report their portfolio alignment scores in their environmental report, and the Secretariat of the Poseidon Principles also publishes the scores of all signatories every year.

Because the signatories of the Poseidon Principles are required to continue to collect and assess the CO_2 emissions of financed ships until the loan reaches full term, the owners of financed ships are encouraged to reduce CO_2 emissions.

2.3 Principles and standards for corporate bonds

Next, the following introduces the principles and standards for assessment of whether the use of proceeds from corporate bonds ("bonds") issued by companies satisfies environmental considerations.

2.3.1 Green Bond Principles (GBP)

The Green Bond Principles (GBP) is voluntary guidelines which was established to secure the transparency of green bonds issued by companies and promote information disclosure and reporting. The GBP was established by the International Capital Market Association (ICMA), and have been revised successively since publication of the first edition in 2014. The most recent edition is the 6th Edition published in June of 2018.

In Japan, the record of the Green Bonds Principles includes bonds for the construction of an LNG-fuelled ship [6)] and for the installation of a ballast water management system [7)]. Third-party reviews found that these bonds satisfied the standards required in the Green Bond Principles.

2.3.2 Climate Bonds Standard (CBS)

The Climate Bonds Standard (CBS) was developed to ensure reliability and transparency in the environmental contribution of bonds issued by companies, and lays out the verification scheme and pre-issuance and post-issuance requirements. The CBS was established by the Climate Bonds Initiative (CBI), an international NGO located in the United Kingdom. It has been revised twice since Version 1 was issued in 2011. The most recent version, Climate Bonds Standard Version 3, was issued in

December 2019.

The Standard consists of common criteria, which are applicable to all sectors, and sector-specific criteria, which are technical criteria for each sector. As of the end of August 2020, sector-specific criteria had been released for Agriculture, Bioenergy, Geothermal Energy, Forestry, Marine Renewable Energy, Solar Energy, Wind Energy, Land Transport, Buildings, Water Infrastructure, Waste Management, etc.

In addition to these sector-specific criteria, a draft criteria for shipping sector (Shipping Criteria) was developed in April 2020, and public consultation was conducted until 26 June 2020. Although the results of the public consultation had not been announced as of the end of August 2020, the following presents an overview of the Shipping Criteria. Here, please note that the content is still in the draft stage, and further revisions are possible in the final version.

As distinctive items in the Shipping Criteria, dedicated fossil fuel carriers such are crude oil tankers and LNG carriers are excluded from the objects of the Criteria. That is, if funds for the construction of a dedicated fossil fuel carrier are procured by issuing corporate bonds, those bonds cannot be certified as complying with the Climate Bonds Standard.

Furthermore, when funds for a ship are raised by bonds complying with the Shipping Criteria, the ship must satisfy the specified threshold for CO_2 emission efficiency in each year until the bonds reach maturity. These threshold values are set so as to decrease gradually until reaching zero emissions in 2050. For ships which do not satisfy zero emissions at the time of construction, the applicant must present a management plan showing how the ship can meet the increasingly stringent threshold values applied each year. In this respect, it can be said that the eligibility requirements of the Climate Bonds Standard are stricter than those of the Green Bond Principles.

2.4 Trends in transition finance

The focus of the above-mentioned Climate Bonds Standard, Green Bond Principles, Green Loan Principles and similar standards is whether the project concerned is “green” or not. In contrast to this, in recent years, there has been increasing interest in the idea that projects related to low-carbon investment should not simply be classified as “green” or not, but should also be assessed based on the viewpoints of the degree of GHG emissions reduction or the transition to decarbonization.

In this connection, the International Capital Market Association (ICMA) set up the Climate Transition Finance Working Group in June 2019 with the participation of approximately 60 financial institutions to discuss the concept of transition finance.

Moreover, at the Climate Action Summit held in September 2019, the following statement by the former Governor of the Bank of England, Mr. Mark Carney, drew considerable attention: “We need a common taxonomy to help financial markets rigorously identify environmental outperformance and direct investment accordingly. The EU’s Green Taxonomy and the Green Bond Standard are a good start, but they are binary (dark green or brown). Mainstreaming sustainable investment will require a richer taxonomy – fifty shades of green.”

In June 2020, Sustainalytics, a leading global provider of ESG research and rankings, announced the start of a service providing second-party opinions (SPO) on transition bonds. Since no international standards have been established for transitions bonds, Sustainalytics plans to establish sectorial standards independently based on predictions by the Intergovernmental Panel on Climate Change (IPCC), International Energy Agency (IEA) and others, and provide SPOs based on those independent standards.

As of the end of August 2020, Sustainalytics had released standards for the natural gas sector and iron and steel sector, and will also release standards successively for shipping, aviation, cement, aluminum and other sectors in the future.

3. TRENDS IN SUSTAINABLE FINANCE IN EUROPE – THE EU GREEN BOND STANDARD

In Europe, an EU Green Bond Standard has been drafted. The following introduces the background, purpose and progress of this standard.

Following the adoption of the SDGs (September 2015) and the Paris Agreement (December 2015) by the United Nations, the European Commission (EC) established the High-Level Expert Group (HLEG) on Sustainable Finance in December 2016.

The HLEG was asked to describe the scale of the issues and opportunities which will be brought about by sustainable finance, and to recommend a comprehensive program of reforms to the framework of financial policy in the EU, including a clear priority ranking.

Here, sustainable finance in EU policy is understood as finance to support economic growth while alleviating pressure on the

environment and considering social and governance aspects. At the EU level, the aim is to support the accomplishment of the purposes of the European Green Deal by directing private investment, as a complement to public financing, to a transition to an economy which realizes climate neutrality, high resource efficiency and societal fairness.

Based on the results of the study by the HLEG, in March 2018, the EC adopted an Action Plan for Financing Sustainable Growth (Action Plan), which included the following:

・Preparation of an EU Green Bond Standard

・Construction of an EU classification system (EU Taxonomy) for sustainable activities

In order to implement the Action Plan, the EC set up a Technical Expert Group on Sustainable Finance (TEG) in July 2018, and in June 2019, the TEG issued an interim report containing 10 recommendations related to the EU Green Bond Standard (EU-GBS), beginning with the following items:

① The EU-GBS should be set up as a voluntary standard, and not a compulsory legal system.

② The EU-GBS should comprise the following four core components:

(1) Alignment of green projects with the EU Taxonomy;

(2) Green Bond Framework for the issuer to provide details of its strategy and issuance process;

(3) Mandatory reporting of use-of-proceeds and environmental impacts; and

(4) Mandatory verification by accredited outside verifiers.

Based on the report by the TEG, the EC will carry out a study with the aim of establishing a finalized version of the EU Green Bond Standard, including whether the Standard should be established as a legal system or not.

The above-mentioned EU Taxonomy, which was issued in March 2020, presents EU standards for determining what is considered sustainable finance, and is a clearly-defined classification system for investors, companies and government-related parties. Under the large categories of Agriculture and forestry, Manufacturing, Energy, Transport etc., the taxonomy defines subcategories such as Passenger rail transport and Passenger cars and commercial vehicles for Transport, with accompanying thresholds for judging their contribution to sustainable finance. For example, the Taxonomy provides threshold values for CO2 emissions when manufacturing 1 ton of hydrogen or ammonia, depending on the type of industry. Oceangoing shipping is not defined as an object of the EU Taxonomy at the present point in time and is to be added in the future. However, the possibility that this may have some type of effect when shipping companies adopt alternative fuels cannot be denied.

4. CONCLUSION

Following the adoption of the Paris Agreement in December 2015, the International Maritime Organization (IMO) adopted the Initial IMO Strategy on Reduction of GHG Emissions from Ships in April 2018, setting a target of reducing total GHG emissions from international shipping by at least 50% by 2050 compared to 2008 levels.

At present, industries, government agencies and academic institutions around the world, as one, are rapidly working toward achievement of this target. There are also moves to support those efforts in the financial area, as can be understood from the establishment of the Poseidon Principles and the draft of the Shipping Criteria for the shipping sector in the Climate Bonds Standard based on the above-mentioned IMO target.

In addition to the trends in Europe described above, there are also moves to standardize assessment and reporting of green bonds, green loans, and the like in the International Organization for Standardization (ISO). Continuing monitoring of those moves will be necessary.

In order to reduce GHG emissions from international shipping by 50% in 2050 compared to 2008 levels, an estimation [8] has shown that investment of US$1-1.4 trillion will be required between 2030 and 2050, suggesting that there will be even higher interest in sustainable finance for international shipping, both in Japan and overseas.

The author hopes that this article will be useful when considering further efforts to reduce GHG in the shipping industry.

REFERENCES

1) IMF Global Financial Stability Report, 2019

2) https://ggpartners.jp/article/000008.html

3) Website of Nippon Yusen Kaisha (NYK Line)
(https://www.nyk.com/csr/envi/greenloans/)
4) Website of Mitsui O.S.K. Lines
(https://www.mol.co.jp/pr/2019/19100.html)
5) Poseidon Principles with technical guidance
6) Website of Nippon Yusen Kaisha (NYK Line)
(https://www.nyk.com/csr/envi/greenbond/)
7) Website of Mitsui O.S.K. Lines
(https://www.mol.co.jp/pr/2018/18063.html)
8) https://www.globalmaritimeforum.org/content/2020/01/Getting-to-Zero-Coalition_Insight-brief_Scale-of-investment.pdf

Wind-Assisted Propulsion Systems for Ships

Motoki SAKAGAMI*

1. INTRODUCTION

Trends in environmental regulations affecting the shipping industry are accelerating year after year. A representative example of these moves is the "Initial IMO Strategy on Reduction of GHG Emissions from Ships," which was adopted in April 2018, targeting a 50% reduction in total GHG emissions from international shipping by 2050 (compared to 2008) and zero GHG emissions in the current century [1]. Based on this, clean technologies which minimize GHG emissions are also demanded in the shipping industry.

Among clean technologies, "wind-assisted propulsion systems" (hereinafter referred to as "WAPS") have attracted attention, as these systems utilize clean wind power to produce propulsive force for ships. While the mention of "wind power" in the world of ships may call to mind the image of the classic sailing ship, WAPS have continued to evolve by incorporating modern technology, and technical development of various systems is now underway in countries around the world.

Although WAPS cannot be considered a general technology in today's shipping industry, one trial calculation indicated that these systems may be installed on more than 10,000 bulkers and tankers by 2030 [2]. Similarly, the Roadmap of the Shipping Zero Emission Project (organized by the Japan Ship Technology Research Association (JSTRA) and Japan's Ministry of Land, Infrastructure, Transport and Tourism (MLIT)) estimates that wind power technologies will be introduced in approximately 2% of international shipping in 2050 to cover part of ship energy consumption [3]. Thus, regardless of the predicted values for the future, there is no doubt that high expectations are placed on WAPS as a response to environmental regulations.

Based on these current conditions, this article introduces an overview and the current status of WAPS. The author hopes that this article will be useful in deepening the understanding of wind power technologies.

2. USE OF WIND POWER IN SHIPPING

The beginnings of wind power in shipping are said to predate the Christian era. Shortly after the invention of the ship as a means of movement on water, the technique of using sails to harness the power of the wind was also devised, and that technology developed with the times. Large numbers of ships were constructed in many countries from the 15th to the 18th century, which is called the Age of Great Voyages, and the discovery of the Americas by Columbus and the circumnavigation of the globe by Magellan are particularly famous.

However, following the invention of the steam engine, steam engines replaced wind power as source of power for ships and, in turn, steam was replaced by the internal combustion engine in the 20th century. The traditional sailing ship gradually declined, and now only small sailboats used for leisure and a few training ships remain.

Recently, in the 1970s and 1980s, wind power was again in the spotlight as a result of the sharp rise in crude oil prices accompanying the Oil Crises of the 1970s. In Japan, research on modern sail-assisted ships utilizing the technologies available at the time was carried out, and WAPS developed by the then-NKK Corporation (Nippon Kokan K.K., now JFE Engineering Corporation) and then-JAMDA (Japan Marine Machinery Development Association, now Japan Ship Machinery and Equipment Association) were installed on a total of 17 ships, beginning with a coastal service tanker, the Shin-Aitoku Maru (Fig. 1). Although the NKK/JAMDA system had a comparatively simple structure, in which canvas sails were fixed on steel frames, a sail angle control technology was introduced, and the system reportedly reduced fuel consumption by 8-10% [4] [5]. However, for various reasons, including the maintenance cost of the sail system, the additional work load on the crew and the recovery (decline) of crude oil prices following the Second Oil Crisis, adoption of this modern sailing ship was limited to those vessels.

* Technical Solution Department, ClassNK

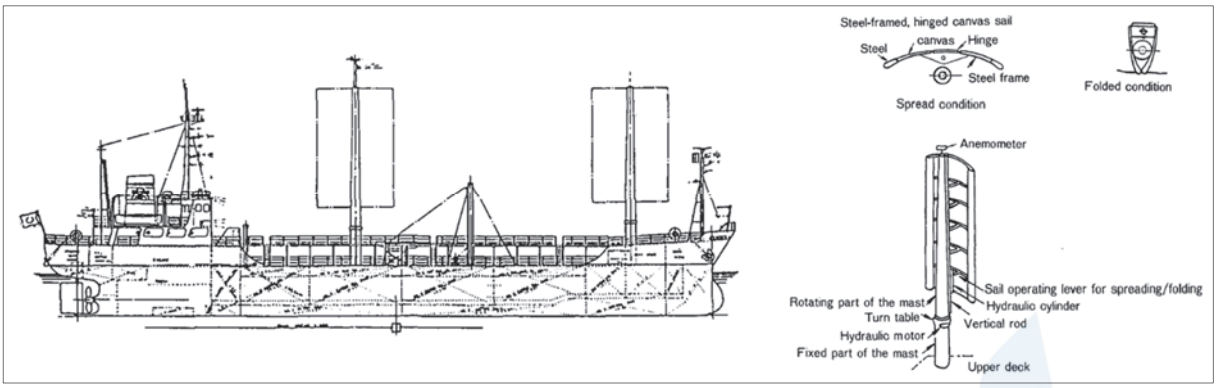

Figure 1　Overview of the Shin-Aitoku Maru [5)]

Figure 2　Image of the Wind Challenger Project [6)]

At this point, it seemed that the modern sailing ship might disappear from the scene, but in the 2000s, active research on a variety of technologies was conducted around the world, encouraged by heightened environmental awareness. In Japan, the Wind Challenger Project, a joint industry-academia research initiative which began in 2009, (Fig. 2), is widely known. In 2015, the International Renewable Energy Association (IRENA) reported survey results showing that many WAPS had reached the design stage or technology verification stage [7)]. Subsequently, moves to develop wind power technologies for ships continued to accelerate in response to the above-mentioned IMO target for GHG reduction, and in some cases, those technologies have already been installed on actual ships.

The following two points may be mentioned as features of the state-of-the-art WAPS under development in recent years, and are indicative of the technological progress from the devices of the past.

① Large scale of devices: Systems with larger scale and larger output are being designed, assuming installation not only on small- and medium-scale coastal ships, but also on large-scale merchant ships.

② Optimization of operation: More efficient operation is realized by combined use of operation automation technologies and weather routing.

3. TYPES AND OVERVIEW OF WAPS

As described above, modern sail-assisted ships are not limited to the form of the classic sailing ship. A number of variations of wind propulsion devices have been developed. Figure 3 shows the classification of wind propulsion devices, as reported in an earlier paper [8)]. This chapter introduces the features of various types of wind propulsion devices in line with this classification.

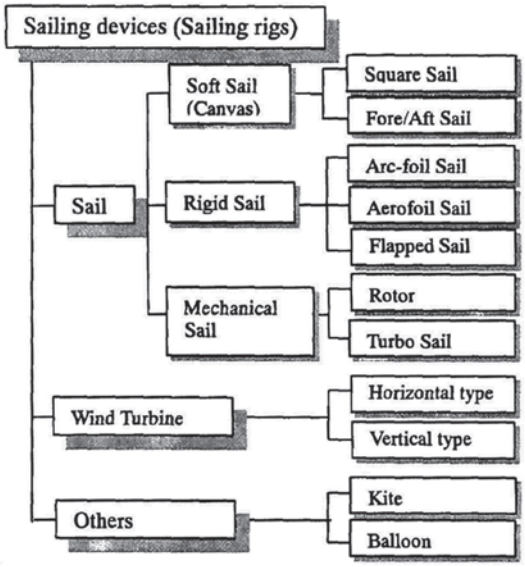

Figure 3 Classification of wind propulsion devices

Figure 4 General view of the Maltese Falcon [9)]

3.1 Wing-Shaped Sails

Wing-shaped sails are a class of wind propulsion devices which obtain lift by receiving wind with a sail with a wing-shaped cross-sectional shape, and are broadly divided into soft sails and rigid (/hard/fixed) sails, depending on the mechanism.

The soft sail is a device with a mechanism that deploys a sail made of canvas or vinyl from a mast, as seen in classic “tall ships,” and is a technology with an extensive record of actual results. The soft sail system developed in the German “Dynaship” project in 1955 was installed on a small-scale cruise ship called the “Maltese Falcon” in 2006 (Fig. 4), and the development of similar systems has continued in several other projects.

The rigid sail employs a mechanism in which the shape of the sail is fixed by a mast or frame, as in the aforementioned NKK/JAMDA sail. In addition to sailcloth, metal materials or FRP can also be used as the material of the sail surface. As a distinctive feature of this design, the optimum wing profile (air foil profile) can be maintained at all times because the sail surface is not deformed by wind. Utilizing this feature, the idea of installing solar panels on the sail surface and simultaneously utilizing solar power has also been proposed [10)]. Among the drawbacks of rigid sails, a mechanism for avoiding strong winds is necessary, and depending on the material, the weight may be significantly larger than that of soft sails. As proposed solutions to the former problem, in the NKK/JAMDA sail, the wind receiving area can be reduced by folding the sail longitudinally in half, and in the “Wind Challenger Project”, the sail area is increased or reduced by vertically raising or lowering the sails.

3.2 Mechanical Sails

This is a type of wind propulsion device in which lift is produced by a mechanical mechanism, and not by the design of the sail cross-sectional shape. Typical examples are the rotor sail and the turbo sail (/suction wing).

The rotor sail is a cylindrical device which rotates at high speed and produces lift (thrust) by the Magnus effect (phenomenon whereby lift acts in the vertical direction of a flow when a rotating cylinder or sphere is placed in a uniform current, as illustrated in Fig. 5). This technology was developed in the 1920s. In recent years, in 2010, it was installed on a trial basis on “E-Ship 1” (Fig. 6), and was also adopted in three ships (including European cruise ships, etc.) beginning in 2015, thus reaching the stage of use in commercial ships.

In the turbo sail, lift is produced by controlling the boundary layer around the device by using a movable flap and a suction mechanism rather than a rotating mechanism (Fig. 7). After this technology was developed in the 1980s, an actual ship test was conducted in 2018.

Mechanical sails have the advantage of realizing a higher lift coefficient than conventional wing-shaped sails. However, because power is constantly required for the rotating mechanism and suction mechanism, the system must be designed so that the energy consumption of these mechanical devices does not exceed the propulsive force that can be obtained by sails.

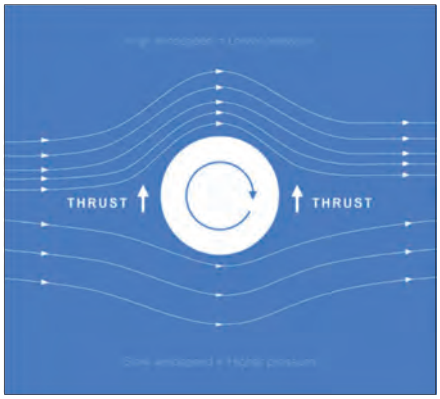

Figure 5　Principle of the Magnus effect [11)]

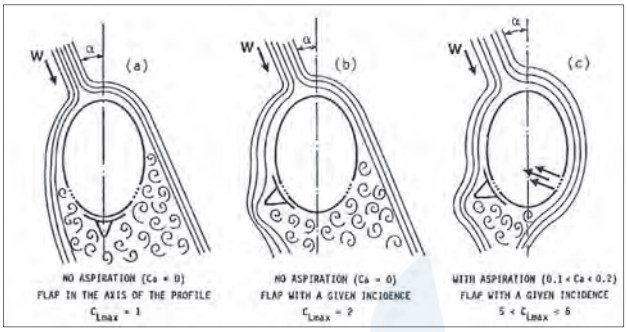

Figure 7　Principle of the turbo sail [13)]

Figure 6　General view of the E-Ship 1 [12)]

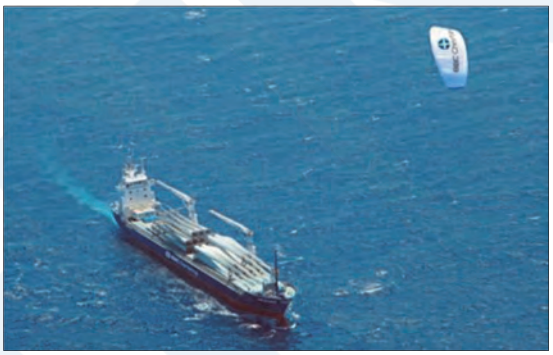

Figure 8　General view of a ship equipped with SkySail [14)]

3.3　Wind Turbines (/Windmills)

In this type of system, a wind turbine which rotates in the wind is installed on the ship, and its rotation is directly linked to the propeller mechanism, or is converted to electricity for use as propulsive force. As a feature of these technologies, unlike the other technologies, propulsive force can be obtained even in a direct headwind. However, past efforts were limited to tests with small craft, and there are still few examples of practical application.

3.4　Towing Kites

Towing kites are deployed from the bow of the ship , and the wind received by the kite produces propulsive force which pulls the ship forward. As the first example of practical application, a system called “SkySail” was developed in 2008. This device has been installed on multiple ships (Fig. 8), and development of similar devices is now progressing [15)]. In comparison with other systems, towing kites require less space on the ship’s deck, and also have the advantage of using the strong winds at higher altitudes, but due to the large freedom of movement of the kite itself, realizing stable control may be considered to be a problem.

3.5　Other Systems

In addition to the systems described above, efforts have also been made to use the shape of the ship’s hull plate as a gigantic “sail.” [16)] Such innovative concept suggests even wider possibilities of wind propulsion.

4.　SAFE DESIGN OF WAPS

If operated correctly, WAPS can realize the merits of improved fuel consumption and reduced GHG emissions, but they must not cause unexpected accidents or harm to the ship’s equipment, crew or surrounding environment. Although the safety of ships is guaranteed by international conventions, domestic laws, related regulations, etc., there are still no conventions applicable to WAPS.

Under these circumstances, in 2019, ClassNK issued “Guidelines for Wind-Assisted Propulsion Systems for Ships,” which provides guidance for the safety of WAPS (Fig. 9). This chapter presents an outline of the content of the provisions of the

Guidelines as reference in the design and operation of WAPS.

Although the Guidelines were established assuming all types of WAPS, successive updates are planned, corresponding to progress in technology, for example, updating of the special conditions for individual types of systems at the stage when actual results and knowledge concerning the adoption of WAPS have been accumulated.

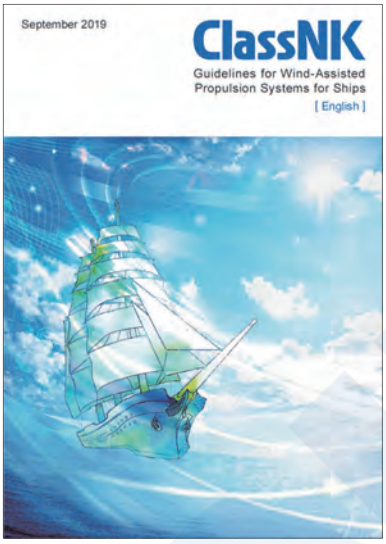

Figure 9　Guidelines for Wind-Assisted Propulsion Systems for Ships [17)]

4.1　Validation of Design Specifications

Because the types of WAPS span a diverse range, the Guidelines specify the following items as functional requirements which are common to all types of WAPS, and should be achieved as the minimum requirements.

- Safety and reliability of the systems
- Safety and reliability of operation
- Resistance to failure
- Protection of personnel and environment
- Interference with ship's function
- Assessment of compatibility

These functional requirements are considered as a baseline of the safety of WAPS. A safe concept can be proposed by planning a system in compliance with these requirements.

4.2　Safety of Operation

A risk assessment is to be carried out to verify the safety of the assumed operation by evaluating the risks associated with installation of WAPS. The appropriateness of the design of the electrical and control equipment related to WAPS is verified by applying the relevant Class rules as necessary.

4.3　Structural Strength

In verifying structural strength, appropriate design loads are set based on the assumed operation. Setting of these loads assumes the following three load cases at minimum:

- In-service condition
- Standby condition during stormy weather
- Abnormal condition in an emergency such as malfunction, etc. (defined based on the risk assessment)

The aerodynamic load, gravitational and inertial load, green water load, etc. are calculated for each load case. WAPS is confirmed to have the sufficient structural strength by the calculations based on these design loads.

4.4　Interference with the Ship

Care must be taken to ensure that the installation of WAPS will not hinder the necessary functions of the ship. For example, an appropriate evaluation of the following items is necessary.

- Effect on ship stability
- Effect on manoeuvrability

・Interference with navigation bridge visibility
・Interference with navigation lights and radar equipment
・Vibration of the system

4.5 Maintenance, Inspections and Surveys

In addition to routine inspections by crew members, periodic surveys are conducted by the classification society to confirm that the system is in good condition. The inspection items and frequency are determined corresponding to the specification of the system, and appropriate means of access for the system are to be provided.

5. ISSUES FOR POPULARIZATION OF WAPS

Although various efforts related to WAPS have already been described, at present, it would be difficult to say the sufficient progress has been achieved in the use of wind power in shipping. Several examples of issues hampering the development and progress of WAPS have been reported [2) 18) 19)]. This chapter introduces some representative examples.

5.1 Institutional Issues

While WAPS are expected to have the effects of improving fuel consumption and reducing GHG on the ship concerned, there are cases where these improvements are not directly linked to the profit of the user. For example, because fuel costs are generally borne by the ship charterers, the ship owners cannot profit directly from the effect of investment in the system. To solve this kind of problem, providing clear institutional incentives is considered necessary. The EEDI (Energy Efficiency Design Index) is a regulation which promotes CO_2 reduction through energy efficiency, and presents technical guidance for reflecting the effect of WAPS in the EEDI. However, in its present form, the effect of wind power cannot be reflected in the EEDI due to the lack of an official certification scheme. Based on this, the above-mentioned Shipping Zero Emission Project aims to create a scheme for the certification by 2022 [3)].

Moreover, accurate information concerning the advantages and disadvantages expected by system installation is indispensable when a ship owner decides on adoption of WAPS, but because WAPS are still a developing technology, there are few cases in which effective verification results have been made public. Under these circumstances, preparation of standards such as the above-mentioned EEDI certification scheme and Class guidelines is considered to be an important means for objectively confirming the performance and safety of WAPS.

5.2 Facility-Related Issues

Particularly in the case of large-scale wind propulsion devices, interference with the cargo-handling equipment and surrounding structures in ports is a concern. In such cases, changes in loading and unloading procedures in the port, and in turn, denial of permission to enter the port are conceivable. Since it would not be realistic to change the equipment in ports to suit the requirements of specific WAPS, study of countermeasures to minimize the effect on work in ports, based on consideration of the type of ship, application, navigation route, etc. of the ship concerned, and adequate advance consultation with the port authorities are considered necessary.

6. CONCLUSION

This article has introduced the overview and current status of WAPS, which are being developed at an accelerating pace in recent years in response to more stringent environmental regulations.

Due to the nature of wind power, it is foreseen that wind power “cannot be used as the main source for propulsion for reasons of scale” [3)]. However, unlike other GHG reduction technologies, such as some alternative fuels, wind power is a clean technology which generates no GHG emissions. Today, when the IMO has laid out a GHG reduction strategy, increasingly high expectations for WAPS, which utilize renewable energy, are foreseen in the future.

On the other hand, use of wind power still has not gained wide acceptance in the shipping industry, and no small number of issues must be solved in order to popularize this technology. To overcome these issues, improvement of the reliability of the technology, while accumulating actual results in the form of demonstration tests and installation on actual ships, will be indispensable, and it is also important to create the related standards for this.

ClassNK intends to contribute to the further development of WAPS from the viewpoint of safety assessment for this

technology based on the “Guidelines for Wind-Assisted Propulsion Systems for Ships” issued by the society last year.

REFERENCES

1) IMO: Resolution MEPC.304(72), Initial IMO Strategy on Reduction of GHG Emissions from Ships, 2018
2) CE Delft: Study on the analysis of market potentials and market barriers for wind propulsion technologies for ships, 2016
3) Shipping Zero Emission Project: Roadmap to Zero Emission from International Shipping, 2020
4) T. Watanabe, Y. Endo, K. Shimizu, H. Namura: The Dawn of the Age of Practical, Sail-equipped Motorships – Application of Sail System to Large Ships –, Nippon Kokan K.K., 1983
5) Nippon Kaiji Kyokai: Introduction of New Ships Built in Japan, Sail-assisted Motor Cargo Ships with NK Class, Technical Bulletin of Nippon Kaiji Kyokai, Vol. 3, pp.97-100, 1985
6) Wind Challenger Project: http://wind.k.u-tokyo.ac.jp/
7) International Renewable Energy Agency: Renewable Energy Options for Shipping Technology Brief, 2015
8) Y. Yoshimura: A Prospect of Sail-Assisted Fishing Boats, Fisheries Sciences, 68, pp.1815-1818, 2002
9) Maltese Falcon: http://symaltesefalcon.com/
10) Eco Marine Power: https://www.ecomarinepower.com/
11) Norsepower: https://www.norsepower.com/
12) ENERCON: https://www.enercon.de/
13) Y. Ikeda: Turbosail System, Journal of the Kansai Society of Naval Architects, Japan, No. 208, pp. 83-85, 1988
14) SkySails Group: https://skysails-group.com/
15) AIRSEAS: https://www.airseas.com/
16) G. Allwright: Commercial Wind Propulsion Solutions: Putting the ‘Sail’ Back into Sailing, Trends and Challenges in Maritime Energy Management, pp.433-443, 2018
17) Nippon Kaiji Kyokai: Guidelines for Wind-Assisted Propulsion Systems for Ships, 2019
18) I. Rojon and C. Dieperink: Blowin' in the wind? Drivers and barriers for the uptake of wind propulsion in international shipping, Energy Policy, 67, pp.394-402, 2014
19) N. Rehmatulla, S. Parker, T. Smith, V. Stulgis: Wind technologies: Opportunities and barriers to a low carbon shipping industry, Marine Policy, 75, pp.217-226, 2017

Recent Research Progresses for Elucidating the Mechanism and Establishing Rational Control Methods for Brittle Crack Arrest

Kazuki SHIBANUMA*

1. INTRODUCTION

In recent years, construction of large container ships has progressed rapidly accompanying the internationalization of markets. Extremely thick steel plates with thicknesses exceeding 80 mm, with which shipbuilders had no prior experience, are used in the hull structures of these vessels. However, the heightened possibility of brittle fracture associated with this increase in plate thickness is a concern. Two-stage safety design, that is, “double integrity,” is critically important for preventing catastrophic damage due to brittle fracture. Double integrity means controlling the “propagation” of a crack in the unlikely event of crack initiation, and ensuring safe “arrest” of the crack before it can result in serious damage.

Although the performance of hull structural plates in arresting brittle cracks (arrest toughness) had not been adequately discussed until the time, Nippon Kaiji Kyokai (ClassNK) organized research committees in stages for (1) Establishment of an evaluation test method and (2) Clarification of the design requirements for brittle crack arrestability. Particularly in (2) Clarification of design requirements, assuming as a standard the arrest toughness values obtained by the established evaluation test method, in which steel plates with a width of 500 mm are used, large-scale tests were conducted with actual ship structure model specimens with a width of 2 400 mm with a joint structure, as shown in Figure 1, and based on the results of those experiments, guidelines for arrest design were established for the first time [11) 12)].

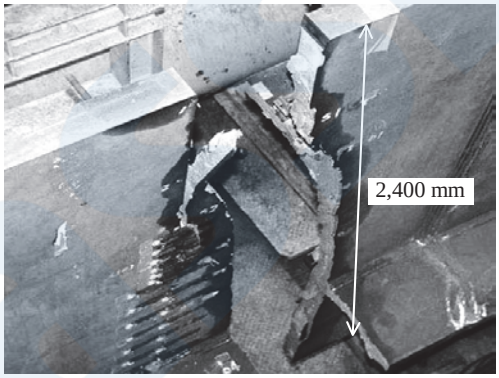

Figure 1 Large-scale arrest test using actual ship structure model specimen with width of 2,400 mm with a joint [13)]

Although the knowledge obtained as empirical facts in these tests was an important result and formed the basis for brittle crack arrest design, many points in connection with the theoretical explanation remained to be clarified. In particular, as shown in Figure 2, it is known that a large discrepancy occurs between the results obtained by general standard tests and wide-size actual ship model tests, and the physical grounds for that divergence had remained unexplained for more than 40 years. This issue was called the “long crack problem” [14)]. Because control of crack propagation behavior when this kind of long crack occurs is directly linked to securing the fracture safety of ship hull structures of increasingly large scale, establishment of a basic theory of the brittle crack arrest phenomenon, including the long crack problem, was an urgent challenge.

* Department of Systems Innovation, School of Engineering, University of Tokyo

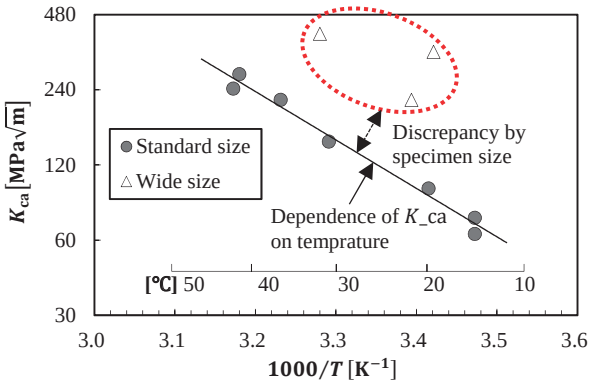

Figure 2　Discrepancy between crack arrest toughness K_{ca} obtained by standard test with 500 mm plate width and large-scale actual ship model test with wide-size plate width of 2 000 mm or more (The physical grounds for this discrepancy had remained unexplained for more than 40 years; this was called the “long crack problem.”) [1) 14)]

Against this backdrop, Nippon Kaiji Kyokai and the author concluded agreements for “Fracture mechanics research for elucidation of the long crack problem (August 2014 to March 2018)” and “Development of a fracture mechanics model for realization of structural arrest design (April 2018 to the present, now continuing)” as “Joint research at industry request,” and carried out research for the purposes of elucidating the mechanism of brittle crack arrest and establishing the scientific basis for a rational method for its control.

This paper presents an overview of the research results, focusing on the above-mentioned joint research. In concrete terms, the composition of the paper is as follows.

Chapter 2：Formulation of Basic Theoretical Model and Elucidation of the Long Crack Problem (Eng. Fract. Mech. 2016a, 2016b [1) 2)])

Chapter 3：Verification of Fracture Criterion (Local Critical Fracture Stress Criterion) (Materials & Design 2018 [3)])

Chapter 4：Physical Interpretation of Required Brittle Crack Toughness Value and Its Estimation for Extremely Thick/High Strength Steel Plates (Eng. Fract. Mech. 2018 [4)])

Chapter 5：Influence of Microscopic Factors of Steel Materials on Arrestability (Acta Materialia 2019a, 2019b [5) 6)])

Chapter 6：Influence of Structural Factors of Joint Structures on Arrestability (Int. J. Mech. Sci. 2020 [7)])

Chapter 7：Development of Numerical Analysis Technique for Realizing Rational Structural Design (Int. J. Solid Struct. 2018, Comp. Meth. Appl. Mech. Eng. 2020 [8) 9)])

(Entries in parentheses show the journal and year of publication of the results.)

2. FORMULATION OF BASIC THEORETICAL MODEL AND ELUCIDATION OF THE LONG CRACK PROBLEM [1) 2)]

2.1 Brittle Crack Propagation and Arrest Phenomena

Because brittle cracks propagate at a high speed of 300 m/s or more in steel materials, brittle crack propagation is a very dangerous phenomenon that causes fracture of a structure almost instantaneously. Although the crack front is presumably accompanied by an extremely high strain rate during propagation, no test method which enables direct measurement of the material constitutive law in such an ultra-high strain rate region has been established. Moreover, the high speed propagation of a brittle crack is a complex physical phenomenon due to the large difference in plastic constraint between the interior, which approximates a plane strain condition, and the surface, where the condition approaches plane stress. This means that two completely different types of fracture proceed simultaneously, namely, cleavage fracture in the interior and ductile fracture at the surface. Because the cleavage fracture which occurs in the interior involves virtually no deformation, and cleavage fracture also proceeds at a far higher speed than ductile fracture, an uncracked part called a side ligament is formed in the vicinity of the surface, where ductile fracture finally occurs in the crack growth process, and direct measurement of the position of the cleavage crack front from outside the specimen with a high speed camera, *etc*. during propagation is impossible. Thus, the phenomena of brittle crack propagation and arrest are extremely problematic physical phenomena in comparison with other fracture phenomena.

2.2 Formulation of Integrated Model

Fracture surface analysis after a fracture occurs has revealed that the most critical microscopic mechanism which controls the phenomenon of brittle crack propagation is continuous cleavage in a body centered cubic (bcc) polycrystalline solid [5]. Based on this fact, the authors placed the "local critical fracture stress criterion" [15] proposed by Aihara *et al*. on the foundation of a governing equation. The critical condition for fracture based on the local critical fracture stress criterion (i.e., the condition for continuation of brittle crack propagation) is expressed by the following equation.

$$\sigma_{yy}[r_c] = \sigma_f \qquad (1)$$

where, σ_f is the critical facture stress and is considered to be a characteristic material property value which is inherent to a material, and $\sigma_{yy}[r_c]$ is the stress perpendicular to the crack face at a small characteristic distance r_c from the crack front. Figure 3 is a schematic diagram of the local critical fracture stress criterion. As shown here, local critical fracture stress is not the critical value for cleavage fracture of a crystal grain unit, but is the average value of the tensile stress in the process zone, which has a width approximately equal to the characteristic distance defined in the vicinity of the crack front. At a glance, the local critical fracture stress criterion is defined by an extremely simple formulation, as shown in Eq. (1). However, nonlinearity is extremely high, and accurate estimation of the local stress in the vicinity of a crack front under a high strain rate condition is difficult .

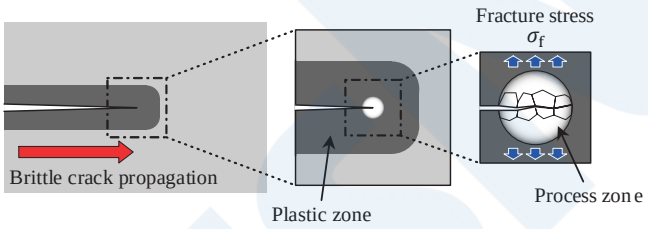

Figure 3 Local critical fracture stress criterion, assuming the brittle crack propagation phenomenon as a critical condition for fracture [1]

As a factor which had not been considered in the conventional fracture mechanics theory, our attention was drawn to the effect of "relaxation of plastic constraint" accompanying crack propagation when a crack develops into a long crack. That is, we formulated the hypothesis that, when a crack grows and develops into a long crack, the plastic zone in front of the crack expands due to an increase in the driving force of crack propagation (for example, the stress intensity factor), and as a result, a transition phenomenon from the plane strain state to a condition approaching the plane stress state occurs at very near the crack front, and the material is released from the high stress state simultaneously with a decrease in stress triaxiality.

In order to verify the validity of the theory described above, we developed a model which integrates the "local critical fracture stress criterion" and "relaxation of plastic constraint." Figure 4 shows a schematic diagram of this integrated model.

Considering the mechanism which controls the phenomena, we adopted the following three assumption in the construction of this model.

(1) The cleavage crack front in a plate is a straight line perpendicular to the direction of crack propagation.
(2) The uncracked side ligament which forms at the plate surface becomes thicker with relaxation of plastic constraint, and compressive loading equivalent to the yield strength of the material acts in the range of side ligament formation and has the effect of closing the crack.
(3) The evaluation of crack propagation/arrest is performed only for the plate mid-thickness part.

By adopting these assumptions, a broad simplification is possible without greatly sacrificing generality. Concretely, based on the above-mentioned assumptions, the four equations which describe (i) the fracture limit, (ii) strain hardening, (iii) yield strength and (iv) the crack closure effect of the side ligament can be reduced to a 1-dimensional problem whose object is limited to only the crack propagation direction. Assuming a sufficiently short crack length as the initial condition, it is possible to reproduce the behavior of brittle crack propagation by simultaneously solving these four equations while updating the crack length. Finally, "arrest" of the brittle crack can be reproduced at the point when a solution that satisfies the simultaneous

equations does not exist, that is, when it is no longer possible to satisfy the critical condition expressed by Eq. (1).

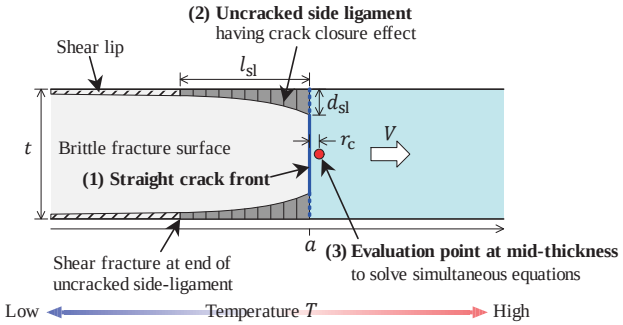

Figure 4　Integrated model of brittle crack arrest phenomenon for solution of the long crack problem [1)]

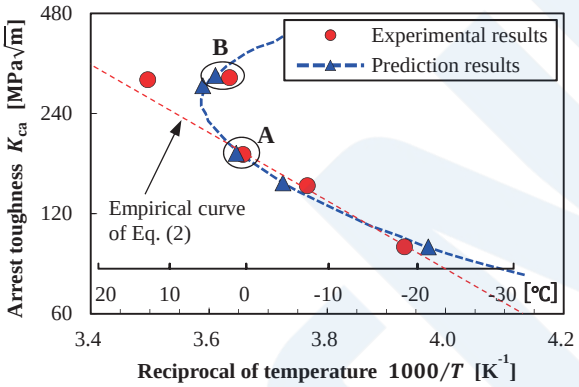

Figure 5　Temperature dependence of crack arrest toughness K_{ca} obtained by a temperature gradient arrest test with standard width specimens including a high applied load region (comparison of experimental results and results of prediction by integrated model) [2)]

2.3　Model Validation by Comparison with Experimental Results

In order to verify the validity of the proposed integrated model, brittle crack arrest tests were carried out using the two types of steel plates shown below, and the results given by the model were compared with the test results.

- Standard width arrest test including a high applied stress region using YP36 class steel plates with a thickness of 30 mm
- Test reproducing the long crack problem (wide duplex test) using YP47 class steel plate with a thickness of 75 mm [16)]

The following presents an outline of the validation results of these respective tests.

2.3.1　Standard width arrest test including high applied stress region using YP36 class steel plate with thickness of 30 mm

The crack driving force, represented by the stress intensity factor, is described as a monotonously increasing function between the crack length and applied stress relationship. On the other hand, assuming that “relaxation of plastic constraint,” which occurs as a result of an increase in this crack driving force, is the main factor in the long crack problem, there is a possibility that a phenomenon similar to the long crack problem can be reproduced, even without the formation of a long brittle crack, by applying a high load not normally applied in the standard width arrest test. Therefore, multiple brittle crack arrest tests were conducted using test plates with the standard width of 500 mm under conditions that included applied stress reached 80 % or more of room temperature yield strength, and a reproduction analysis was carried out using the proposed integrated model.

Figure 5 shows the temperature dependence of the arrest toughness K_{ca} obtained in this experiment, where the experimental results are indicated by red circles. According to the conventional empirical knowledge, the relationship between K_{ca} and temperature follows the Arrhenius equation, as shown below.

$$K_{ca} = K_0 \cdot \exp(-k_0/T) \qquad (2)$$

where, T is absolute temperature, and K_0 and k_0 are material constants. However, the results of the experiment under a high applied load deviated substantially from the empirical equation shown in Eq. (2), and arrest occurred earlier than predicted by the equation. Comparing the experimental results that occurred depending on the dimensions of the test specimen, which is known at the long crack problem (Fig. 1), it became clear that the results in the case of a long crack in the wide-width (duplex) test, and the results in the case of a high applied load in the standard width test show a similar tendency.

In reproducing the arrest test using the proposed integrated model, the local critical fracture stress σ_f needs be determined in advance. For this test plate, σ_f was identified so as to minimize the least square errors with the experimental results for three tests under low applied stress that showed good agreement with the empirical equation in Eq. (2). The above Figure 5 also shows the results of predictions obtained by the integrated model based on this condition. The predicted results are shown by the blue circles and the blue line in the figure. These results showed that deviation from the results of the empirical equation on the high applied stress side also occurred in the results predicted by the model. Thus, the model reproduced the same tendency as the experimental results.

Figure 6 shows a comparison of the fracture surface and crack arrest position obtained in the experimental results and the predicted results using the model. Not only the crack arrest position, but also the formation range of the side ligament near the plate surface showed good agreement in the experimental results and model prediction results.

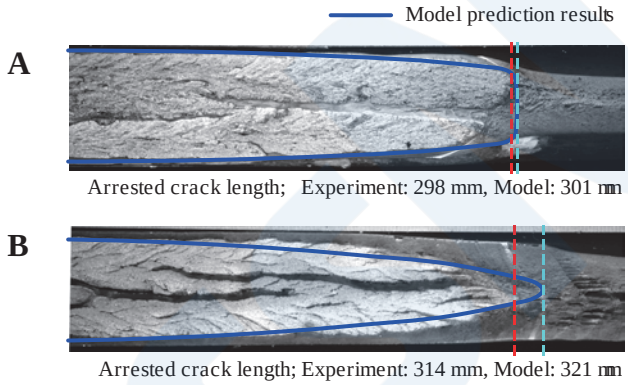

Figure 6 Comparison of experimental results and results of calculation by the integrated model for the fracture surface formation morphology in the standard width arrest test (corresponding to A and B in Fig. 5) [2)]

2.3.2 Test reproducing long crack problem using YP47 class steel plate with thickness of 75 mm[15)]

Large-scale crack arrest tests to reproduce the long crack problem are extremely expensive. Therefore, in this study, the results of past experiments conducted by Nippon Kaiji Kyokai [15)] were used as the object of validation.

This test is a duplex-type arrest test, in which the occurrence of crack arrest is evaluated by causing a brittle crack to initiate and propagate in a crack-running plate containing an embrittled part, which is intentionally formed by the welding heat effect, and that crack is made to run into the target test plate. This duplex-type arrest test is equivalent to the CAT (Crack Arrest Temperature) test, which has reportedly been carried out internationally in recent years. The test was conducted with two specimens. The stress intensity factor when the brittle crack ran into the test specimen was $K = 12{,}000$ N/mm$^{3/2}$, whereas the arrest toughness evaluated in the standard width temperature gradient arrest test was $K_{ca} = 6{,}100$ N/mm$^{3/2}$ or $7{,}100$ N/mm$^{3/2}$. In other words, the driving force of crack propagation based on linear facture mechanics greatly exceeded the crack arrestability performance of the specimens. However, the long crack problem was reproduced successfully, as “arrest” in the test plate was confirmed in both test specimens.

The local critical fracture stress σ_f used in the reproduction analysis by the proposed integrated model was identified based on the experimental results of a standard width temperature gradient arrest test, which was conducted separately. Figure 7 shows the comparison of the experimental results and the model prediction results for the crack arrest position in the test reproducing the long crack problem. From the figure, the model prediction results showed extremely good agreement with the experimental results. Furthermore, although the duplex test has been used in order to clearly judge whether crack propagation or crack arrest occurs, the model prediction results suggested that a temperature-related transition curve existed in the crack propagation distance in the test plate until crack arrest was achieved.

Based on the results described above, the basis for modeling which provides a quantitative explanation of the phenomena of brittle crack propagation and arrest in steel plates was established, including an elucidation of the long crack problem, providing physical grounds that had remained unknown for more than 40 years.

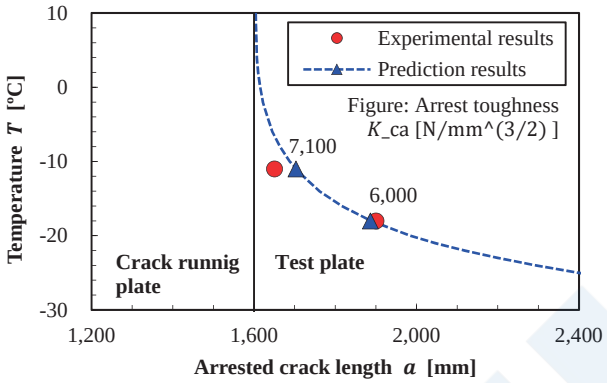

Figure 7　Comparison of experimental results and model prediction results for the long crack problem [2)]

3.　VERIFICATION OF LOCAL CRITICAL FRACTURE STRESS CRITERION [3)]

3.1　Concept of Experiment and Design of Specimens

In the integrated model for reproducing the brittle crack arrest phenomenon of steel plates outlined in Chapter 2, the most important constituent element is the “local critical fracture stress criterion,” which represents the critical condition for fracture in cleavage fracture propagation. Until now, however, this theory had been no more than one hypothesis, since its validity could only be discussed based on the validation results by the integrated model presented in section 2.3. As noted in section 2.1, the most important reason why the critical fracture condition of the brittle crack arrest phenomenon remained unexplained was the extreme difficulty of directly measuring brittle crack propagation behavior. In particular, due to the change in the degree of plastic constraint in the plate center and at the surface, the triaxiality of the crack front is high in the plate mid-thickness region and low near the plate surface. For this reason, the crack front takes a “tunneling” shape advancing in the plate interior, which is a large obstacle to direct measurement (Fig. 8(a)). However, if the local critical fracture stress criterion is in fact valid, and a linear crack front is assumed to exist through the full plate thickness, ideal 2-dimensional crack propagation is realized and it is possible to estimate the crack propagation behavior of the entire crack, including the interior of the material, by using only information measured at the surface. This means that the local stress in the vicinity of the crack front during high speed propagation can be evaluated by carrying out a reproduction analysis by the finite element method (FEM) by inputting the time of crack passage measured at the surface, and the validity of the local critical fracture stress criterion can be verified experimentally.

Based on this experimental concept, a side groove for controlling the decrease in stress triaxiality in the near-surface region of the test specimen was designed based on a preliminary analysis by FEM. Figure 8 shows an outline of the standard plate-shaped specimen and the side-grooved specimen used in this test.

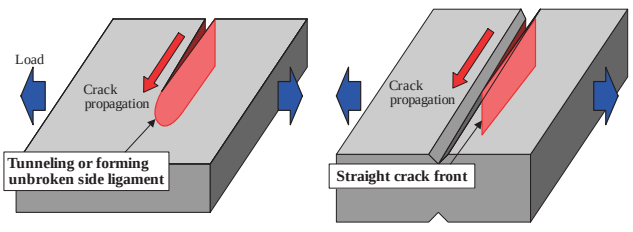

(a) Standard plate specimen　　(b) Side-grooved specimen

Figure 8　Standard plate-shaped specimen and the side-grooved specimen used in this test [3)]

Figure 9 shows an example of the distribution of local stress in the vicinity of the crack front in the plate thickness direction, assuming a straight linear crack front and the finite element model used in the design. For comparison, the figure also shows the distribution of local stress around the crack front of a standard plate specimen. In the range of 95 % of the plate thickness from the mid-thickness, the maximum principal stress decreased by as much as 27 % in the standard plate specimen, but in the side-grooved specimen, this decrease could be reduced to only 3.4 %. Therefore, assuming that brittle crack growth follows the local critical fracture stress criterion, it was shown that a crack front in a linear ideal 2-dimensional condition can be realized in substantially the entire plate thickness direction.

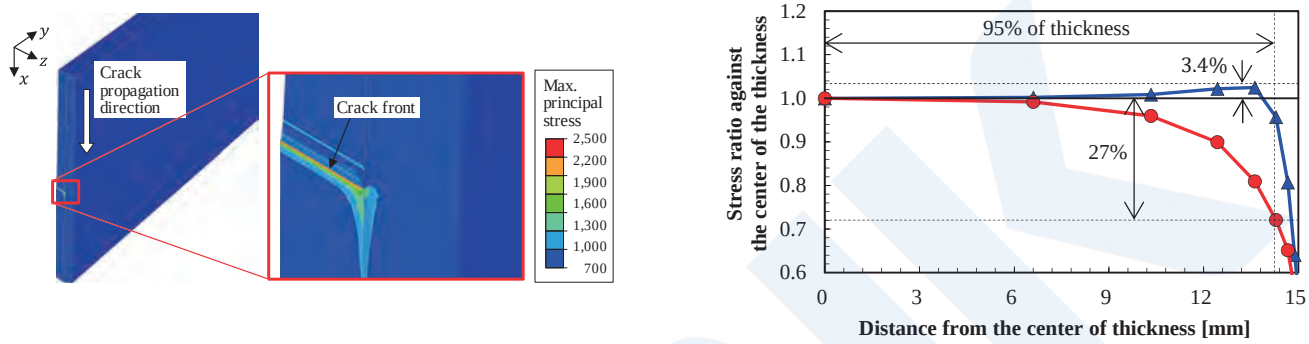

Figure 9 FE model used in design of the side-grooved specimen, and comparison of the local stress distributions in the plate thickness direction around the crack front for a standard plate specimen and the side-grooved specimen [3)]

3.2 Fracture Test and Reproduction Analysis by FEM

Based on the above-mentioned conditions, multiple brittle crack propagation tests based on various temperature and applied load conditions were carried out using two types of steel plates (steel S and steel N). The timing of crack passage was measured by the response of strain gauges mounted to the bottom of the side groove, as shown in Figure 10. Very high level of technology was required in the execution of this measurement because it was necessary to adjust the strain gauge mounting position at the 0.1 mm order.

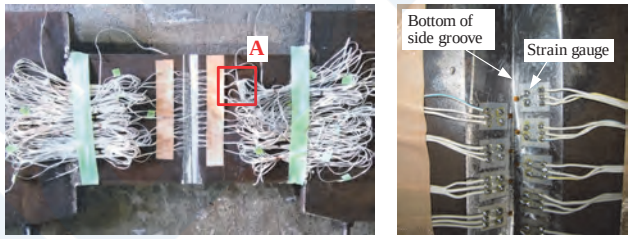

(a) Whole of specimen (b) Close up of A

Figure 10 General view of a side-grooved specimen and closeup showing the mounted strain gauges for crack velocity measurement [3)]

A reproduction analysis by FEM was conducted for each test using the crack passage time obtained by the measurements as an input condition. The dynamic stress intensity factor K_d was evaluated based on conventional linear fracture mechanics, while the local stress σ_{yy} was evaluated based on the local critical fracture stress criterion. Figure 11 shows the obtained results. It can be understood that K_d, which represents the conventional theory, not only showed different tendencies with respect to both temperature and applied stress in each material, but also changed greatly accompanying crack propagation during each test. Therefore, the impossibility of using K_d directly as a critical fracture condition became obvious. In contrast, although σ_{yy} includes some variations that are thought to be due to measurement error, it also became clear the σ_{yy}, which is based on the local critical fracture stress criterion, always shows a certain value inherent to the material during high speed crack propagation, independent of the temperature and applied load. This certain characteristic of the material is none other than the local critical fracture stress σ_f. Based on these results, the validity of the local critical fracture stress criterion, which had been no more than a hypothesis until now, was verified for the first time.

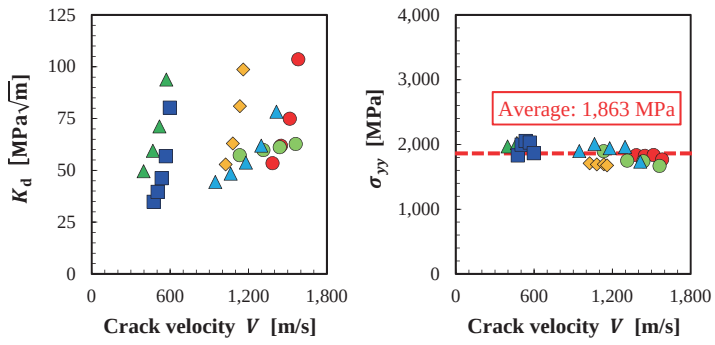

(a) Steel S

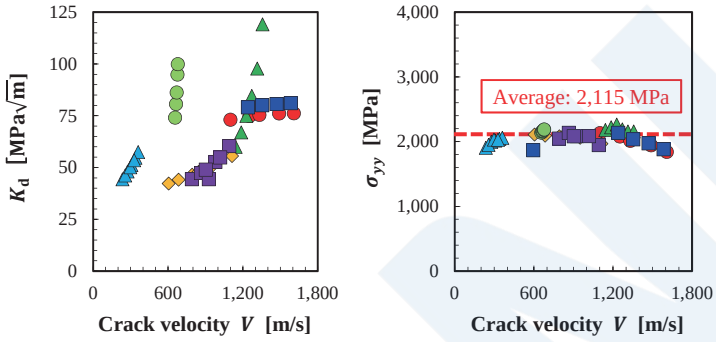

(b) Steel N

Figure 11　Dynamic stress intensity factor K_d and local stress σ_{yy} evaluated in brittle crack propagation test [3)]

4. PHYSICAL INTERPRETATION OF REQUIRED BRITTLE CRACK ARREST TOUGHNESS VALUE AND ITS ESTIMATION FOR EXTREMELY THICK/HIGH STRENGTH STEEL PLATES [4)]

4.1 Brittle Crack Arrest Toughness Value

At present, arrest design of actual ship hulls is defined by an index called the "required brittle crack arrest toughness value" [11) 12)]. This required brittle crack arrest toughness value $\widetilde{K}_{ca}$ is specified as K_{ca}, which corresponds to the actual result of the temperature at which cracks were arrested in a large-scale test in the temperature dependence curve of the arrest toughness K_{ca} obtained by a temperature gradient test with standard width specimens. In case a steel plate has a value of K_{ca} which is equal to or greater than the value of $\widetilde{K}_{ca}$, it is assumed that a crack can be arrested safely under any conditions, provided the temperature is equal to or higher than the temperature in the large-scale test and stress does not exceed that in the test. However, this brittle crack arrest toughness value $\widetilde{K}_{ca}$ depends only on the experimental "K_{ca} when a crack could be arrested, when the design stress obtained by an actual structural scale test was used." In other words, this is not a test at the actual design temperature, and is limited to the results for certain designated structural specifications. For this reason, its general applicability was a matter of great concern. Furthermore, the physical grounds for the existence, as such, of the brittle crack arrest toughness value were also unexplained. Owing to the large scale of the tests used to evaluate this brittle crack arrest toughness value and the enormous cost and labor involved, it is important to establish a firmly-grounded theory which is capable of explaining the generality and physical grounds of the brittle crack arrest toughness value.

Here, we attempted to explain the physical grounds of the brittle crack arrest toughness value by a systematic numerical analysis using the integrated model proposed in Chapter 2, and based on the results obtained thereby, we also estimated the effects on the heavier gauge and higher strength of steel plates, which are expected to increase in the future.

4.2 Calculation Procedure Using Integrated Model

The characteristic values of steel plates which are necessary in a reproduction analysis of an arrest test by the integrated model are only (a) plate thickness, (b) yield strength and (c) local critical fracture stress. If these characteristics can be given, it is possible to obtain a single curve expressing the temperature dependence of the arrest toughness K_{ca} like that shown in Figure

12 as the result of a calculation by the integrated model. Although this curve shows that K_{ca} tends to increase as the temperature rises under comparatively low temperature conditions, including the conditions of the standard test, it can be understood that there is also a temperature region where a solution does not exist, with a certain temperature as a critical temperature threshold. This critical temperature expresses the fact that brittle crack propagation cannot occur under the action of any applied load at temperatures equal to or higher than the critical temperature. Here, this critical temperature is termed the ICAT (intrinsic crack arrest temperature).

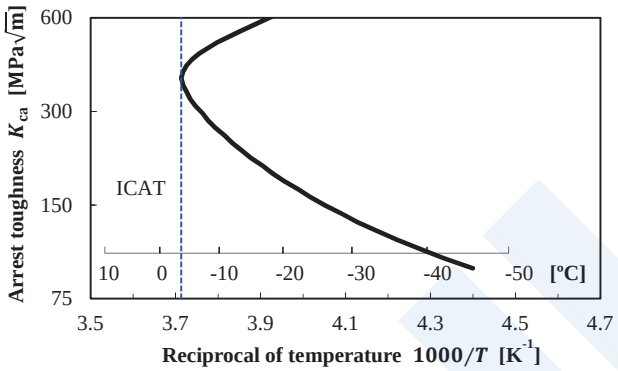

Figure 12 Relationship of temperature dependence of arrest toughness K_{ca} and intrinsic crack arrest temperature (ICAT) in a temperature gradient arrest test calculated by the integrated model [4)]

On the other hand, when a systematic reproduction analysis of a constant temperature duplex test (or CAT test) was carried out under various applied load and temperature conditions using the integrated model, a contour diagram like that shown in Figure 13 was obtained as the relationship between the stress intensity factor and temperature when the brittle crack ran into the test plate, and the crack arrest length in the test plate. For convenience, here, the case of arrest at a crack length of 300 mm or less in the test plate was defined as a judgment of "arrest" (blue line in Fig. 13). When the results of the temperature gradient arrest test shown in Figure 12 were overlaid on these results, as shown by the red line in Figure 13, it can be understood that the ICAT of the temperature gradient test is positioned on the lower side than the ICAT of the constant temperature duplex test. Using this feature, it is possible to explain the origin of the brittle crack arrest toughness value with respect to the strength, thickness and design temperature of a steel plate. The concrete procedure is presented below (also see Fig. 13).

(i) The thickness and yield strength of the steel plate are designated, and the local critical fracture stress σ_f is identified so that the ICAT in the duplex arrest test is in agreement with the design temperature.

(ii) Using the σ_f obtained in (i), a reproduction analysis of the temperature gradient arrest test is carried out, and the temperature dependence of arrest toughness K_{ca} is obtained.

(iii) The K_{ca} corresponding to the design temperature on the low K_{ca} side of the K_{ca} temperature dependence curve of (ii) is defined as the required brittle crack arrest toughness value $\widetilde{K}_{ca}$.

In case a steel plate of the same thickness and yield strength has a higher K_{ca} at the design temperature than the required brittle crack arrest toughness value $\widetilde{K}_{ca}$, the ICAT of that plate in the duplex test will inevitably be higher than the design temperature. This means that the plate can arrest a brittle crack within 300 mm under any applied stress condition, thus demonstrating the validity and physical grounds of the required brittle crack arrest toughness value.

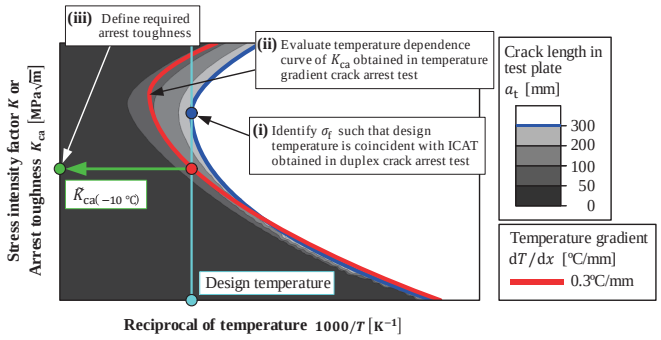

Figure 13　Estimation procedure for the temperature/stress intensity factor dependence of the crack arrest length and required brittle crack arrest toughness value $\tilde{K}_{ca}$ in the duplex arrest test calculated by the integrated model [4)]

4.3　Result of Estimation of Required Brittle Crack Arrest Toughness and its Validation

The required brittle crack arrest toughness value $\tilde{K}_{ca}$ of steel plates having thicknesses t = 30 mm to 120 mm and room temperature yield strength σ_{Y0} = 300 MPa to 600 MPa was estimated for a design temperature condition of $-10°C$ by the procedure described in section 4.2. Figure 14 shows the estimated values of the obtained $\tilde{K}_{ca}$. The results revealed that the bilinear relationship of t and σ_{Y0} shown by the following equation is materialized for $\tilde{K}_{ca}$ (dashed lines in Fig. 14).

$$\tilde{K}_{ca(-10\ °C)}\left[\mathrm{N/mm^{3/2}}\right] = 0.0724(\sigma_{Y0}[\mathrm{MPa}] + 339)(t\ [\mathrm{mm}] + 48) \qquad (3)$$

In order to verify the validity of the estimation curve of Eq. (3), the results [16)] of all wide-width duplex tests led by Nippon Kaiji Kyokai since the 2000s were compared. The results showed that the brittle crack propagation/arrest results in all the tests can be explained without contradiction, demonstrating the validity of the estimation curve of Eq. (3). Table 1 shows the required brittle crack arrest toughness value $\tilde{K}_{ca}$ for the design temperature of -10 °C estimated by Eq. (3) for high strength, extremely thick steel plates whose applicability is studied in recent years.

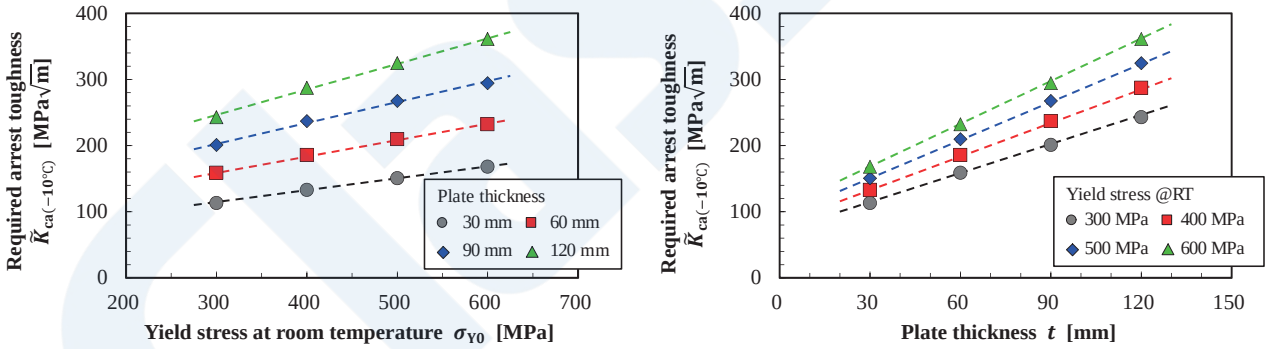

Figure 14　Estimation of the required brittle crack arrest toughness value $\tilde{K}_{ca}$ for steel plates with various thicknesses and yield strengths (dashed lines show the estimation curves obtained with Eq. (3)) [4)]

Table 1 Estimated value of the required brittle crack arrest toughness value $\tilde{K}_{ca}$ of representative steel plates at design temperature of -10 °C [4)]

Thickness t [mm]	Yield strength σ_{Y0} [MPa]	Required arrest toughness $\tilde{K}_{ca(-10\ °C)}$ [N/mm$^{3/2}$]
75	400	6,599
	470	7,223
90	400	7,400
	470	8,102
100	400	7,935
	470	8,688

The range of application of the integrated model used in the discussion in this chapter is limited to plate structures. Therefore, the reader should note that these results are applicable only to simple plate structures. In order to evaluate the arrestability of actual members with joints or other structural discontinuities, it is necessary to develop a numerical analysis technique with high general applicability, as described in Chapter 7.

5. INFLUENCE OF MICROSCOPIC FACTORS OF STEEL MATERIALS ON ARRESTABILITY [5) 6)]

5.1 Microstructure Dependence of Cleavage Crack Propagation Resistance

It is known that the mechanical properties of metal materials, such as strength and toughness, fatigue resistance performance, *etc*. strongly depend on the microstructure of the material. In particular, it is known that toughness, i.e., performance with respect to initiation of brittle fracture in steel materials, largely depends on crystal grains, which are the most fundamental factor of the microstructure, and steel materials display higher properties as the grain size decreases. On the other hand, the necessity of "arrest toughness" that is, the brittle crack arrest performance of a material, has been widely recognized in recent years, spurring intense competition among steel makers in Japan and other countries to develop high arrestability steels. However, the influence of the steel microstructure on arrest toughness has not been clarified.

Here, in order to clarify the relationship between the crystal grain size, which is the most basic microstructural factor, and cleavage crack propagation resistance, two techniques of different scales, both of which integrate experimental research and numerical analysis, were proposed and examined. The outlines of these techniques are presented in the following.

5.2 Evaluation of Local Critical Fracture Stress based on DCB Test and Reproduction Analysis by FEM

As described up to this point, the local critical fracture stress criterion is the most promising basic theory of the critical condition for facture in cleavage crack propagation, which is the core of brittle crack propagation, and local critical fracture stress is an intrinsic material characteristic expressing the cleavage crack propagation resistance possessed by a material. Therefore, referring to the approach based on experimental research and reproduction analysis by FEM proposed in Chapter 3, the influence of the crystal grain size on local critical fracture stress was evaluated.

First, three types of steels, Steel S1, S2 and S3, were prepared. The three steels have identical chemical compositions, and only their grain size is different, as shown in Figure 15. Using these three sample steels, the Double Cantilever Beam (DCB) test shown in Figure 16(a), which is a small-scale test of crack arrestability, was carried out under multiple temperature conditions. A reproduction analysis by FEM was also conducted under a constant crack velocity condition, as shown in Figure 16(b), based on the knowledge obtained by validation by a preliminary systematic numerical analysis [17)], and local critical fracture stress was evaluated.

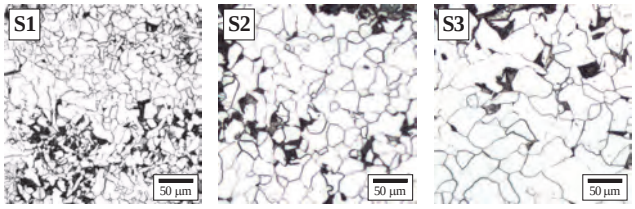

Figure 15　Sample steels for evaluation of crystal grain size dependence of cleavage crack propagation resistance (ferrite/pearlite steels with identical chemical compositions and different grain sizes) [6)]

Figure 17 shows the results of an evaluation of local critical fracture stress σ_f obtained based on an experiment and reproduction analysis by FEM for a DCB test using the above-mentioned sample steels with different grain sizes. This evaluation showed that σ_f increases as the grain size becomes coarser, in other words, coarser-grained materials display higher properties. This tendency is the opposite of "toughness," which is the resistance of a material to initiation of brittle fracture, as described in section 5.1. As in the results presented in Chapter 3, σ_f displayed an intrinsic constant value for each of the sample steels, even though the tests were conducted under multiple temperature conditions.

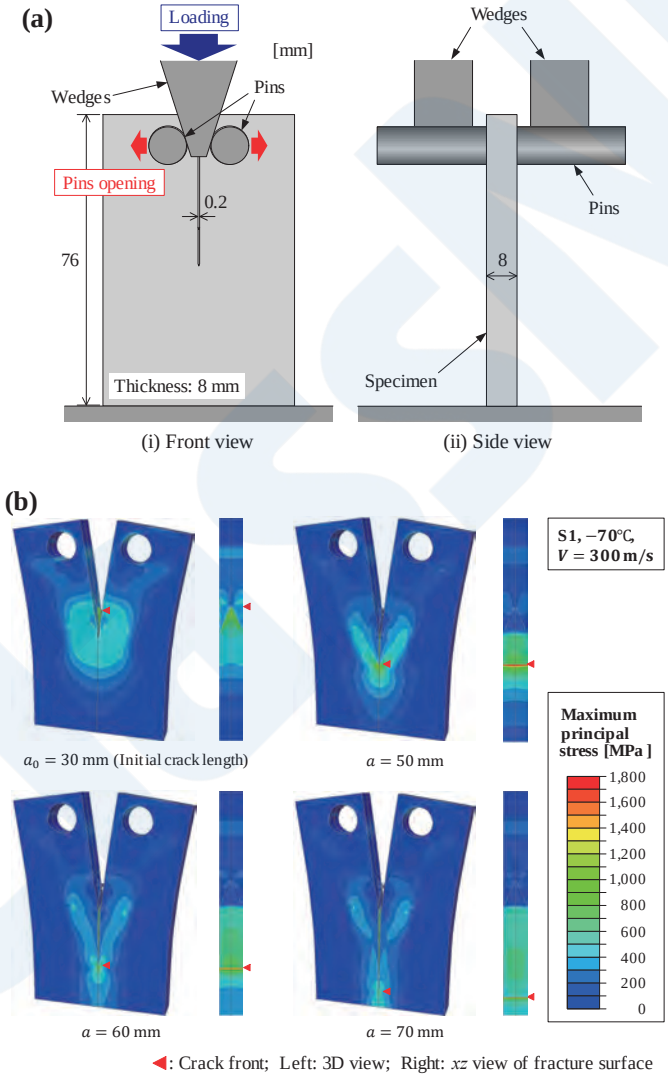

Figure 16　DCB test for evaluation of local critical fracture stress σ_f: (a) specification of test piece and jig, (b) reproduction analysis by FEM [6)]

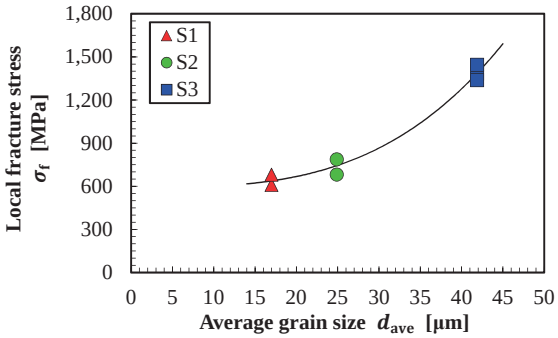

Figure 17 Crystal grain size dependence of local critical fracture stress σ_f (σ_f increases as the grain size becomes coarser; this tendency was the opposite of "toughness," i.e., resistance to brittle fracture initiation) [6)]

5.3 Evaluation of Dissipation Energy based on Microscopic Mechanism related to Origin of Cleavage Crack Propagation Resistance

Here, an evaluation was carried out by an approach based on the microscopic mechanism of fracture, which is completely different from the evaluation method in the previous section, in order to provide stronger support for the results of the evaluation of the grain size dependence of cleavage crack propagation resistance presented in the previous section.

The fracture surface formed by cleavage crack propagation comprises two different types of fracture surfaces, namely, cleavage planes and tear-ridges as shown in Figure 18. However, it is thought that the dissipation energy (also called effective surface energy) associated with tear-ridge formation, which is accompanied by large plastic deformation, accounts for the larger part formed by this dissipation energy.

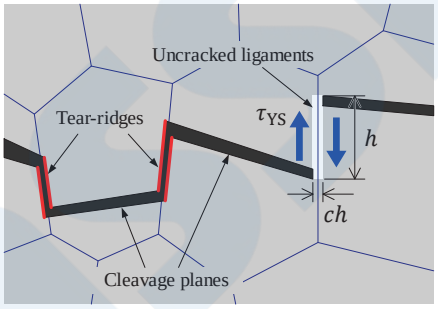

Figure 18 Fracture surfaces formed by cleavage crack propagation, comprising cleavage planes and tear-ridges, and their dissipation energy mechanisms [6)]

As shown in Figure 18, it is thought that tear-ridges are generally formed along grain boundaries. For this reason, there is concern that an estimation based on the influence of crystallographic factors on the plastic deformation behavior until the formation of tear-ridges, which is the source of dissipation energy, will not necessarily agree with an estimation by continuum mechanics, which assumes an isotropic material as its object. First, therefore, a micromechanics test for quantification of the amount of dissipation energy accompanying the formation of one tear-ridge was proposed. Concretely, first, a micro-scale test piece, as shown in Figure 19(a), was prepared using a single-phase material consisting of coarse crystal grains. In this test piece, cleavage planes are simulated by focused ion beam (FIB) machining of sharp slit-shaped notches which reach the grain boundaries in two adjoining grains. It is then possible to reproduce tear-ridge formation by performing a tensile test of this test piece, as shown in Figure 19(b), to induce ductile fracture between the two cleavage planes simulated by FIB machining. The amount of dissipation energy accompanying tear-ridge formation can be calculated by integrating the load-displacement curve obtained in this test. As a result of multiple tests using different slit-notch tip distances (i.e., distance between two cleavage planes), an empirical equation stating that the dissipation energy accompanying tear-ridge formation per unit length is proportional to the second power of the slit-notch tip distance was obtained, as shown in Figure 19(c). Because this is arranged as an approximation based on continuum mechanics assuming an isotropic material, it was suggested that the influence of crystallographic factors in the vicinity of the grain boundary is slight.

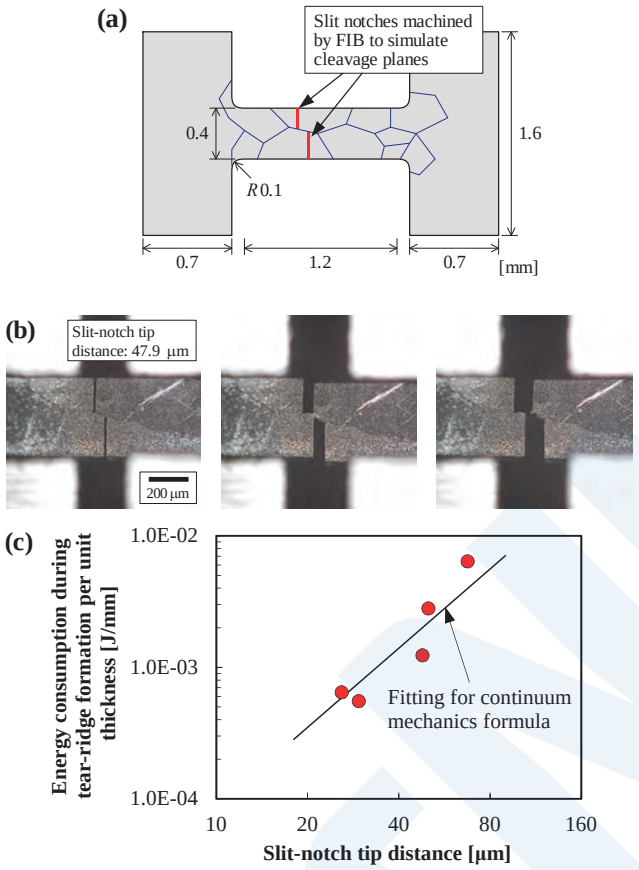

Figure 19　Small-scale test for evaluation of dissipation energy accompanying tear-ridge formation: (a) geometry of test piece, (b) deformation and fracture behavior of test piece in test process, (c) relationship of dissipation energy and slit-notch tip distance [6)]

Cleavage crack propagation is an extremely complex phenomenon, and the model proposed by Aihara and Tanaka [18)] is the sole micromechanical model in past research. However, there was a large discrepancy between the results of this model and the actual phenomenon due to the various simplifications applied in the model, such as discretization by rectangular unit cells of a single shape and evaluation of the stress intensity factor of the crack front by superimposition of approximate solutions. Therefore, in this research, a new cleavage crack propagation model based on the extended finite element method was developed [5)]. With this model, the fracture surface formation accompanying complex cleavage crack propagation can be reproduced simply and with high accuracy by defining the finite element mesh independently from the crack and crystal grains. Here, tear-ridge formation interpolated between the formed cleavage planes was modeled as shown in Figure 20, and an algorithm for evaluation of the dissipation energy accompanying fracture plane formation was constructed using the empirical equation for the amount of dissipation energy accompanying the tear-ridge formation quantified by the above-mentioned small-scale test.

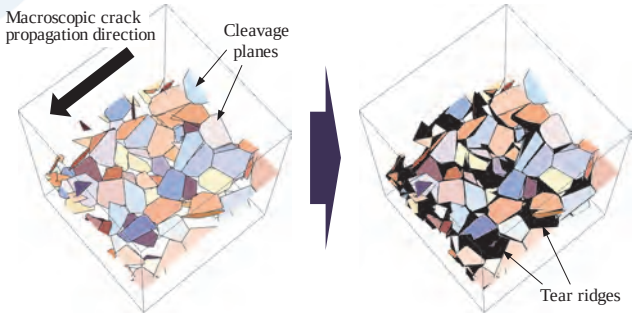

Figure 20　Cleavage crack propagation model [5)] based on extended FEM and modeling of tear-ridge formation [6)]

Figure 21 shows the results of an evaluation of the dissipation energy accompanying fracture plane formation per unit area of the three types of steels (S1, S2 and S3) used in section 5.2, based on their average grain size distributions. From these results, dissipation energy accompanying fracture plane formation, in other words, cleavage crack propagation resistance, increases as the grain size of the steel becomes larger.

As described above, in all evaluations, the results of an evaluation of cleavage crack propagation resistance of steel materials by a technique which combines the two completely different approaches of experimental research and numerical analysis showed a tendency opposite to that of toughness, which indicates the resistance of a material to brittle crack initiation. This surprising result is expected to make a large contribution to the development of high arrestability steels, for which increasing demand is predicted in the future.

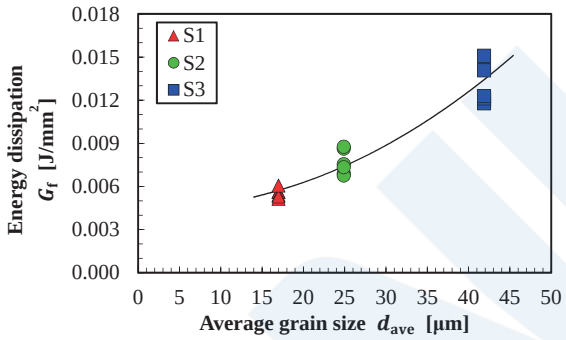

Figure 21 Grain size dependence of dissipation energy G_f accompanying cleavage fracture plane formation (showing completely the same tendency as the results for local critical fracture stress in Fig. 17) [6)]

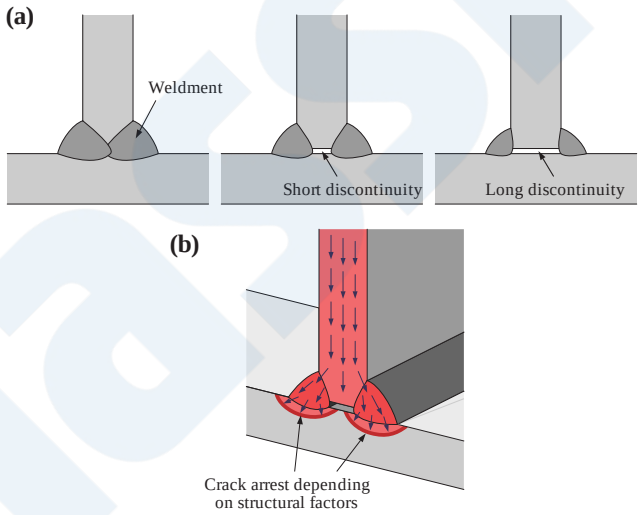

Figure 22 Concept of structural arrest: (a) Structural factors such as structural discontinuities in the joint structure, (b) influence of structural factors on arrestability[7)]

6. INFLUENCE OF STRUCTURAL FACTORS OF JOINT STRUCTURES ON ARRESTABILITY [7)]

6.1 Influence of Structural Factors on Arrestability

When designing structures with excellent arrestability, it is essential to develop materials with excellent arrestability, as described in Chapter 5. However, as a result of experimental studies in recent years, it has become clear that not only the properties of these materials, but also structural factors such as joints, *etc*. have no small influence on arrestability [19) 20)]. This is because realization of crack arrest and enhancement of crack arrestability can be expected when larger structural discontinuities exist in the joint structure, as illustrated in Figure 22. However, due to the extremely high cost and large amount of labor involved in this type of structural-scale arrest testing, the obtainable experimental results were fragmentary, and the mechanism by which

these structural factors influence arrestability remained to be clarified. Thus, elucidation of the contribution of these structural factors to arrestability and establishment of the concept of structural arrest design are critical issues with the potential to dramatically enhance arrestability performance as a structure, in a separate dimension from the material development described in Chapter 5.

Against this background, rapid crack arrest tests were carried out using small-scale specimens simulating joint structures containing a structural discontinuity, focusing on the transparent resin polymethyl methacrylate (PMMA) as a material which makes it possible to realize rapid crack propagation with little energy dissipation accompanying crack propagation like that which occurs during cleavage crack propagation in steel materials. Furthermore, a quantitative evaluation of the influence of structural factors such as structural discontinuities in joints, *etc*. was attempted for the first time by an integrated approach using a combination of experimental research and numerical analysis by detailed measurement of rapid crack propagation behavior with a high speed camera and stress intensity factor analysis by the extended finite element method.

6.2 Rapid Crack Arrest Test Using PMMA and its Measurement with a High Speed Camera

In order to evaluate only the influence of geometrical factors of the specimen on rapid crack propagation behavior, in this validation experiment, the specimen was cut out from a single block of PMMA rather than preparing joints by adhesion. Figure 23 shows the geometry of the specimen used in this experiment. The same DCB test as in Chapter 5 was used as the mechanism for inducing crack initiation, propagation and arrest. The thickness of the vertical material, which is the main member when measuring crack propagation behavior, was set at 13 mm. However, holes with a width of 4 mm or 6 mm were machined in some of the test pieces, supposing a structural discontinuity at a position equivalent to a joint, as shown in Figure 22(a). In total, three types of specimens were prepared (P0: no hole, P4, 4 mm hole, P6: 6 mm hole). To vary the load at the time of crack initiation, multiple specimens of P0, P4 and P6 were prepared with different radii at the notch bottom, which is the site of crack initiation. The high speed camera measurements were carried out using an i-SPEED 726 camera manufactured by nac Image Technology Inc., as shown in Figure 24. The field of view was set in a direction which captured the cruciform joint from the front, and the measurements were conducted under the condition of a framerate of 250 000 fps.

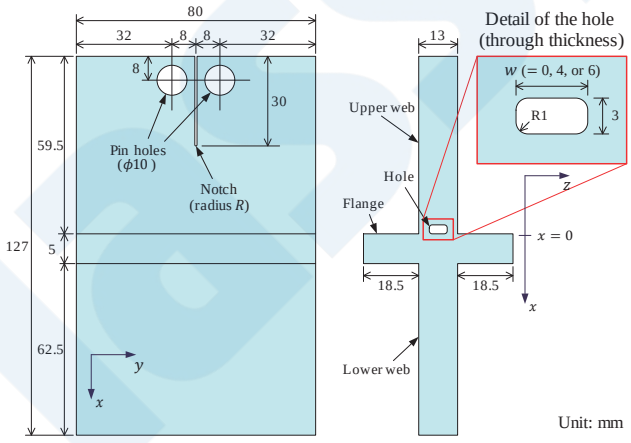

Figure 23 PMMA specimen simulating joint structure for evaluation of the influence of structural factors on arrestability (in some specimens, a structural discontinuity was reproduced by machining a hole with a width of 4 mm or 6 mm at the joint position) [7)]

Figure 25 shows the relationship of the crack arrest length and pin opening displacement (equivalent to the driving force of crack propagation). Based on these results, it was suggested that cracks are arrested earlier as the size of the structural discontinuity in the specimen becomes larger, and this effect was remarkable in the flange part. In particular, focusing on the test results for P0-3, P4-4 and P6-2, the order of the distance between the pins was P0-3 < P4-4 < P6-2 (in order from the shortest distance), but this notwithstanding, the crack arrest length showed the opposite tendency, that is, P0-3 > P4-4 > P6-2. In other words, this experiment showed that a substantial improvement in rapid crack arrestability is possible by providing a larger structural discontinuity at joint parts.

Figure 26 shows the crack propagation behavior and final crack arrest position for P0-3, P4-4 and P6-2 measured by the high speed camera. In P4-4 and P6-2, which have structural discontinuities, the detailed rapid crack propagation behavior was

successfully measured, showing, for example, that when a crack ran into the flange, its crack front shape curved with curvature and then was arrested.

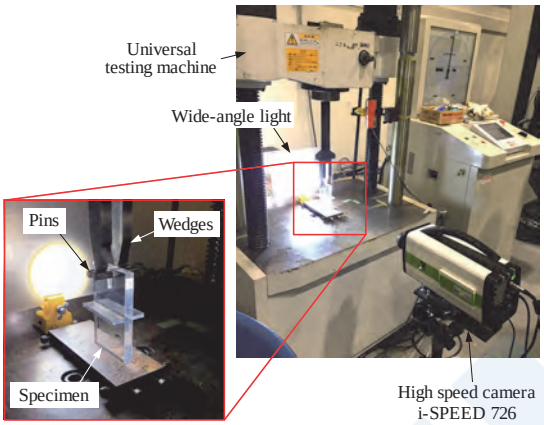

Figure 24 Setup for measurement of crack propagation behavior in a joint structure arrest test using PMMA photographed by high speed camera [7)]

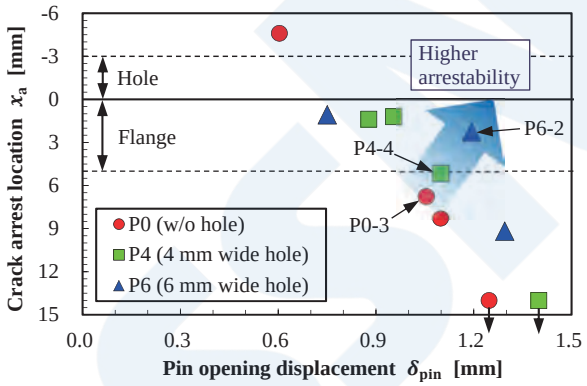

Figure 25 Relationship of crack arrest length and pin opening displacement in joint structure arrest test using PMMA [7)]

6.3 Analysis of Stress Intensity Factor based on Extended FEM

In order to elucidate the mechanism of crack arrest in joint structures containing a structural discontinuity, a stress intensity factor analysis was conducted using the extended FEM method [21) 22)], which makes it possible to model a crack and the finite element mesh independently, by rational use of the detailed history of the position and shape of the crack front in the rapid crack propagation process captured by the high speed camera.

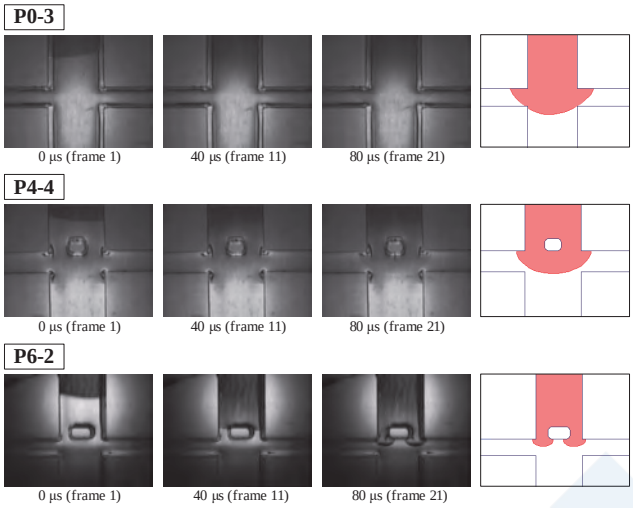

Figure 26　Results of measurement of crack propagation in the joint structure arrest test using PMMA photographed by high speed camera [7)]

Figure 27 shows the transition of the distribution of maximum principal stress accompanying crack growth in P0-3, P4-4 and P6-2. Figure 28(a) shows the transition of the stress intensity factor K, which was evaluated based on the integral interaction method [23)]. In P0-4, which does not contain a structural discontinuity, the results confirmed that K decreases monotonously and the crack is arrested with no change in that behavior. In contrast, in P4-4 and P6-2, which contain structural discontinuities, K increased once when the crack passed through the side of the hole, but then decreased rapidly thereafter. This rapidly decreasing tendency of K also continues after the crack runs into the flange, and finally K becomes substantially equal to that in P0-3, and the crack is arrested earlier in P4-4 and P6-2 than in P0-3. For a more quantitative evaluation of the effect of structural discontinuities in improving arrestability, the results for P4-4 and P6-2, in which holes were machined, were normalized by the result for P0-3, which does not contain a structural discontinuity, are shown in Figure 28(b). These results showed that K decreases greatly, by as much as 35%, in P6-2, which has the largest structural discontinuity, in comparison with P0-3 without a structural discontinuity. As a structural arrest effect, this result is equivalent to applying a material with 1.5 times higher crack arrest toughness. Thus, structural factors have an extremely high crack arrestability enhancement effect in comparison with actual material development. In the future, realization of structures with innovative crack arrestability is expected by developing new numerical analysis techniques and using those techniques in combination with structural optimization techniques.

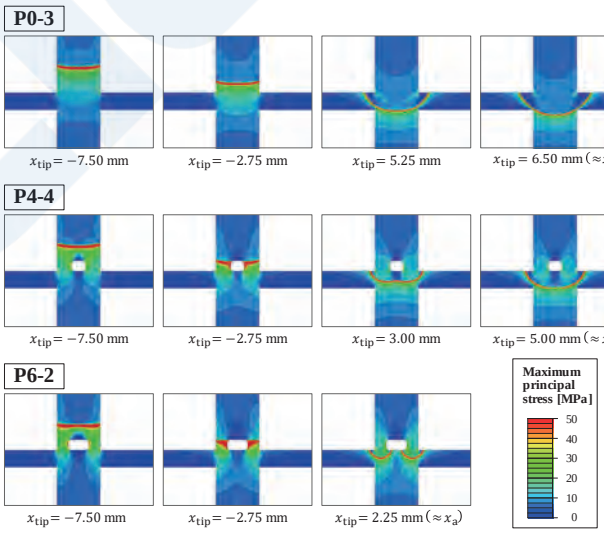

Figure 27　Distribution of maximum principal stress in a joint structure arrest test using PMMA obtained by extended FEM [7)]

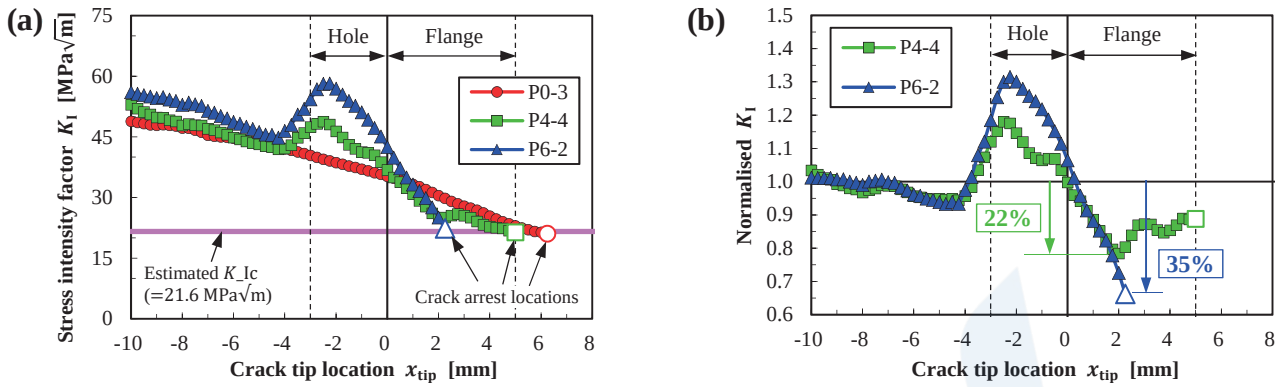

Figure 28 (a) Transition of the stress intensity factor K in the joint structure arrest test using PMMA based on extended FEM and (b) transition of K normalized by the result for the specimen without a hole (P0-3) [7)]

7. DEVELOPMENT OF NUMERICAL ANALYSIS TECHNIQUE FOR REALIZATION OF RATIONAL STRUCTURAL DESIGN [8) 9)]

7.1 Significance of Development of Numerical Analysis Technique for Reproduction of Brittle Crack Propagation/Arrest Behavior

Although the validity of the integrated model described in Chapter 2, which reproduces brittle crack propagation/arrest behavior, was demonstrated as a physical model, its range of application is limited to simple plate structures using homogenous materials. However, the results presented in Chapter 6 suggested the possibility that arrestability performance as a structure can be dramatically enhanced by utilizing structural factors such as joint discontinuities. Although a technique which is capable of reproducing the brittle crack arrest phenomena in arbitrary structures with discontinuities with high accuracy and high generality has not been established, if such a technique can be realized, it is considered possible to construct an extremely practical structural design method that can provide structures with innovative crack arrestability by using the brittle crack arrest reproduction technique in combination with optimization techniques.

It is widely known that FEM is the most powerful numerical analysis technique for structural analysis. Therefore, the development of a model of the brittle crack arrest phenomenon which is applicable to arbitrary structures within the framework of FEM is considered to be an effective strategy. For this, it will be necessary to incorporate the local critical fracture stress criterion, which is the critical condition for fracture in the brittle crack arrest phenomenon, into FEM. The five points mentioned below are assumed to be issues for development.

(1) Accuracy of local stress evaluation
(2) Reduction of numerical calculation cost
(3) Expression of crack front shape
(4) Extension to elastoplastic analysis
(5) Integration with ductile fracture model

With recognition of the above-mentioned purpose and issues, the author's research group is currently developing a rapid crack propagation analysis technique based on the mesh superposition method, which is one numerical analysis technique within the framework of FEM. Among the issues mentioned above, as of September 2020, when this paper was written, the results of "(1) Accuracy of local stress evaluation" and "(2) Reduction of numerical calculation cost" had already been finalized and published in leading international journals [8) 9)]. For "(3) Expression of crack front shape," development of the basic technique has also been completed and submission of a paper is planned for the near future [10)]. On the other hand, "(4) Extension to elastoplastic analysis" and "(5) Integration with ductile fracture model" are now in the development stage. Therefore, the following will present an outline of the above-mentioned (1) to (3) as the current status of progress.

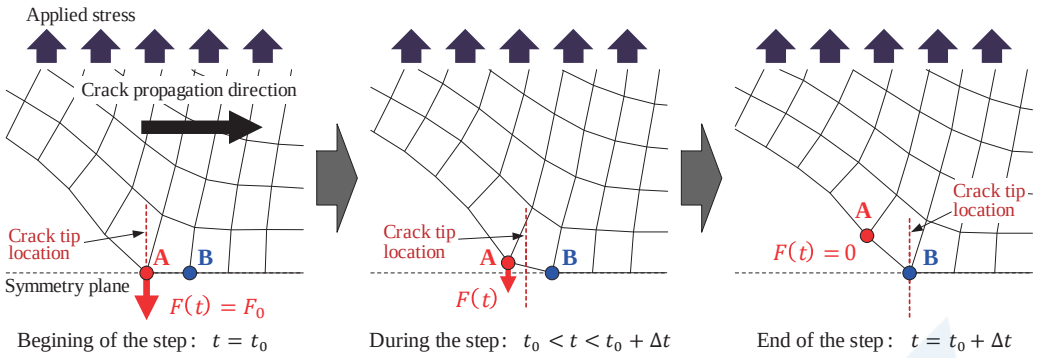

Figure 29　Modeling of rapid crack propagation by the nodal force release method [8) 9)]

7.2　Nodal Force Release Technique and Control of Numerical Vibration [8)]

The simplest and most robust technique for simulating dynamic crack propagation by FEM is the nodal force release technique, in which the reaction force at nodes arranged on a symmetrical plane is released sequentially, as illustrated in Figure 29. The nodal force release technique has already been applied to many analyses of crack propagation owing to its simplicity. However, the purpose of almost all of those studies was to evaluate conventional macroscopic fracture mechanics parameters such as the stress intensity factor or the J-integral. As described in Chapter 3, it is difficult to reproduce the brittle crack arrest phenomenon with macroscopic parameters of this type, and it is necessary to establish a technique which enables highly accurate evaluation of the local stress in the vicinity of the crack front based on the local critical fracture stress criterion.

From the perspective outlined above, first, a systematic local stress analysis based on the nodal force release technique was carried out for the issue "(1) Accuracy of local stress evaluation" in section 7.1, focusing on the most basic 2-dimensional linear elastic solid, and the results were elucidated and a related solution method was proposed.

As shown in Figure 29, the nodal force release technique is a technique in which the reaction force at element nodal points where the crack front is located are released sequentially, but the proper reaction force history is not self-evident until the nodal force has been completely released. First, therefore, a systematic study of the history of the nodal reaction force which is to be released was conducted. As a result, it became clear that the technique of releasing the nodal reaction force F linearly at time t, as shown by the following equation, is a robust condition which is capable of stably providing high accuracy under a variety of conditions.

$$F(t) = F_0\left(1 - \frac{t - t_0}{\Delta t}\right) \qquad (4)$$

where, F_0 is the reaction force at the beginning of release of reaction force, t_0 is the time at the beginning of release of nodal force and Δt is the time required for release of nodal force (i.e., the length of the time step), as shown in Figure 29. As one example of a calculation result, Figure 30 shows a comparison with the method in which the nodal force is released instantaneously, when applied to the distribution of local tensile stress σ_{yy} ahead of a crack front. In comparison with the instantaneous release method, the linear nodal force release method can reduce the vibration of the stress field ahead of the crack front, but in comparison with an exact solution, vibration still exceeds $\pm 10\%$.

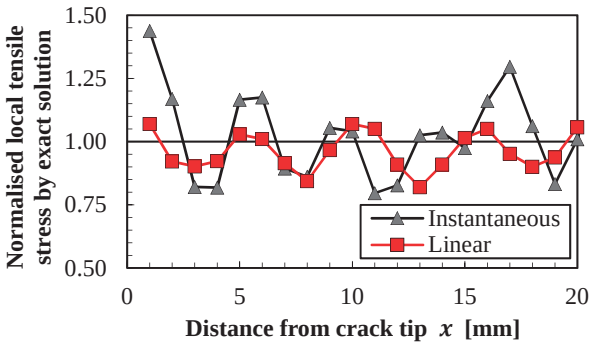

Figure 30　Local tensile stress field nodal force release technique, normalized by the result of the exact solution (non-negligible numerical vibration occurs even when the nodal reaction force history is optimized) [8)]

The vibration of the local stress field shown in Figure 30 is numerical vibration caused by discretization of the crack propagation process in the nodal force release method. This type of vibration cannot occur in the rapid crack propagation process of an intrinsic ideal continuum. Therefore, application of Rayleigh damping was studied as a means of effectively reducing this numerical vibration. Rayleigh damping is the mostly generally used artificial damping method in structural analyses, and makes it possible to independently define the artificial damping corresponding to the mass matrix and that corresponding to the stiffness matrix of a dynamic FEM analysis. The results of a systematic analysis verification, as shown in Figure 31, clarified the fact that numerical vibration of the local stress field can be reduced extremely effectively by setting damping appropriately, corresponding to the stiffness matrix.

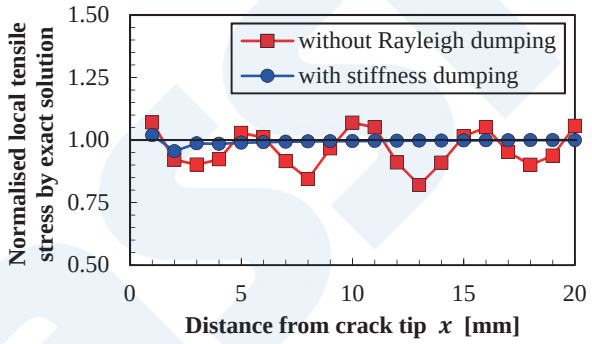

Figure 31　Improvement of numerical vibration of local tensile stress field by application of Rayleigh damping (numerical vibration is effectively reduced by applying damping appropriately, corresponding to the stiffness matrix) [8)]

In the crack propagation analysis described above, the crack velocity was given as an input parameter, and the local stress output was evaluated as the result. This is called the generation phase, and indicates the stage in which the basic accuracy verification of the technique is carried out. On the other hand, in order to reproduce actual rapid crack propagation behavior, it is necessary to set the local critical fracture stress criterion (the local stress in the vicinity of the crack front agrees with the local critical fracture stress) as the fracture criterion, and predict the crack propagation velocity and crack arrest position. This analysis, which is called the application phase, is an inverse analysis in which the relationship of the input and output data is the opposite of that in the generation phase, and the solution must be obtained implicitly by introducing an iterative solution. In order to verify the effectiveness of the numerical vibration reduction method by Rayleigh damping proposed above in the application phase, an application phase analysis of an elastic body was carried out using the local critical fracture stress criterion as the fracture criterion. Figure 32 shows an example of the results obtained. When Rayleigh damping was not applied, large vibration occurred in the crack velocity, finally producing a solution in which large divergence from the exact solution remained, and as a result, the calculations in this process ended in failure. In contrast to this, when appropriate Rayleigh damping was applied, an extremely stable calculation could be realized, and at the same time, the crack velocity history showed good agreement with the exact solution, confirming the validity of this approach.

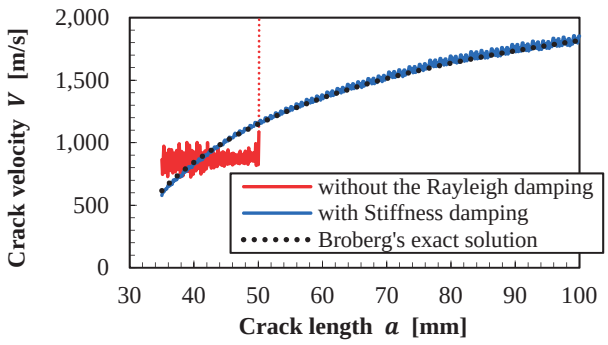

Figure 32　Effect of applying Rayleigh damping in an application phase analysis based on local critical fracture stress criterion [8)]

The basis for realizing stable, highly accurate rapid crack propagation analysis within the FEM framework was established by incorporating the nodal force release technique and appropriate Rayleigh damping, as described above.

7.3　Development of Dynamic Crack Propagation Technique based on Mesh Superposition Method (Improvement of Numerical Calculation Cost: 2D Model) [9)]

Referring to the research thus far, in a local stress evaluation based on the local critical fracture stress criterion, it is necessary to evaluation a region from 100 μm to 300 μm ahead of the crack front. On the other hand, if the dimension of a target member for structural design is approximately 2 m, a scale gap on the order of 10 000 times exists between the two. According to the preliminary study up to this point, it is necessary to arrange 3 to 5 finite elements between the crack front position and the local stress evaluation point in order to realize high accuracy. Assuming hypothetically that the element size is 50 μm, more than 30 million nodes must be arranged on the crack propagation plane alone in order to reproduce crack propagation with a length of 1 m in a steel plate with a thickness of 80 mm. Considering the total structure, this is equivalent to a finite element model with a scale of several 100 million to several billion degrees of freedom, even as a minimum estimate. Furthermore, the calculations must be repeated as many as 20 000 times in order to reproduce crack propagation. Since a calculation of this scale would require a very long period of time, even by massively parallel computing using a super computer, this approach is unsuitable for practical use as a structural design tool. Therefore, the issue “(2) Reduction of numerical calculation cost” in section 7.1 is an extremely important essential task.

In order to solve this problem, we focused on the mesh superposition method [24)], which is one numerical analysis technique within the FEM framework. The mesh superposition method (hereinafter, s-version of FEM) is a technique in which the target domain as a whole is discretized by a global mesh consisting of comparatively coarse elements, and a local mesh of finer elements is superimposed on a target position such as a stress concentration.

Because this approach makes it possible to define local meshes flexibly in order to realize a local highly accurate evaluation, in this research, we attempted to construct a new fracture mechanics model by applying the concept of mesh superposition to a dynamic crack propagation problem for the first time. A schematic diagram of the model is shown in Figure 33. The local mesh is defined only for the vicinity of the rapidly-moving crack front using the minimum number of degrees of freedom necessary in order to incorporate the local critical fracture stress criterion with high accuracy. Therefore, the local mesh moves together with the propagation of the crack.

In the dynamic structural analysis based on the mesh superposition method, displacement $\mathbf{u}(\mathbf{x})$ and acceleration $\ddot{\mathbf{u}}(\mathbf{x})$ are approximated by the following equations.

$$\mathbf{u}(\mathbf{x}) = \begin{cases} \mathbf{u}^{\mathrm{G}}(\mathbf{x}) & \text{in } \Omega^{\mathrm{G}} \setminus \Omega^{\mathrm{L}} \\ \mathbf{u}^{\mathrm{G}}(\mathbf{x}) + \mathbf{u}^{\mathrm{L}}(\mathbf{x}) & \text{in } \Omega^{\mathrm{L}} \end{cases} \tag{5}$$

$$\ddot{\mathbf{u}}(\mathbf{x}) = \begin{cases} \ddot{\mathbf{u}}^{\mathrm{G}}(\mathbf{x}) & \text{in } \Omega^{\mathrm{G}} \setminus \Omega^{\mathrm{L}} \\ \ddot{\mathbf{u}}^{\mathrm{G}}(\mathbf{x}) + \ddot{\mathbf{u}}^{\mathrm{L}}(\mathbf{x}) & \text{in } \Omega^{\mathrm{L}} \end{cases} \tag{6}$$

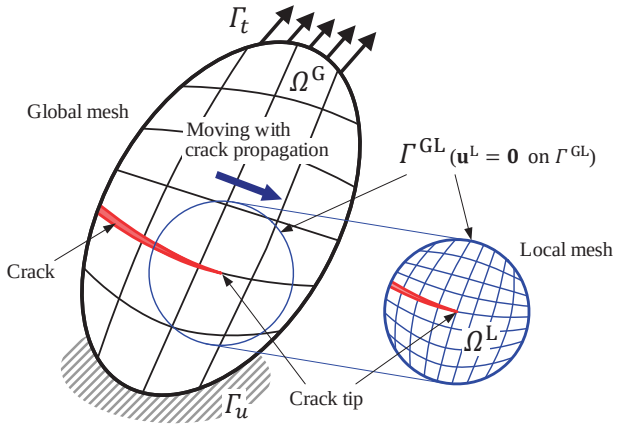

Figure 33 Concept of dynamic crack propagation based on mesh superposition method [9)]

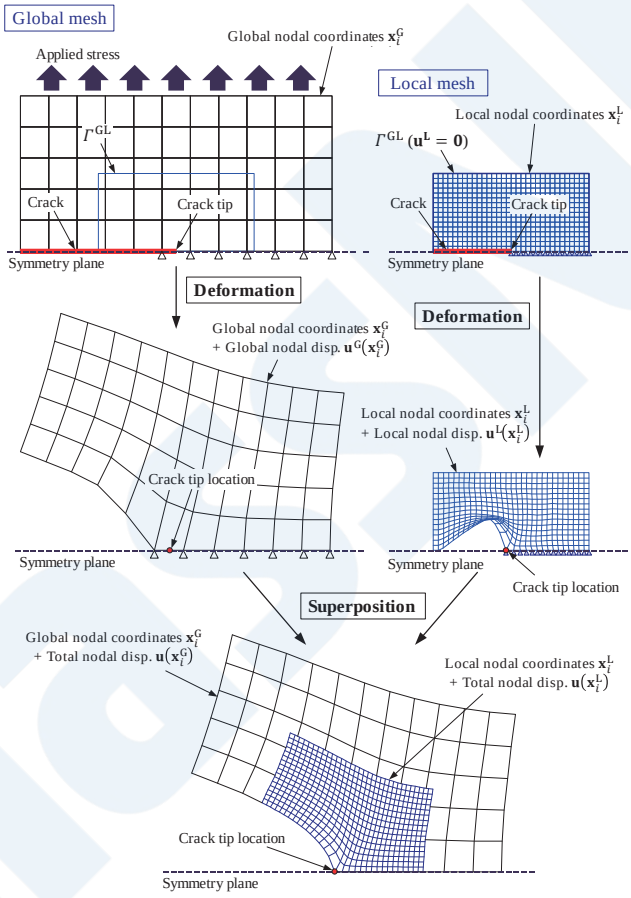

Figure 34 Reproduction of displacement field near the crack front by mesh superposition method [9)]

In this manner, it is possible to obtain approximations of displacement and acceleration simply by superimposing the FE approximations of the two on the domain where the local mesh is superimposed on the global mesh. Moreover, in order to guarantee the continuity of displacement $\mathbf{u}(\mathbf{x})$ and acceleration $\ddot{\mathbf{u}}(\mathbf{x})$ in the boundary Γ^{GL} of the local mesh, it is also necessary to satisfy the Dirichlet boundary conditions shown by the following equations:

$$\mathbf{u}^{\mathrm{L}}(\mathbf{x}) = \mathbf{0} \qquad \text{on } \Gamma^{\mathrm{GL}} \tag{7}$$

$$\ddot{\mathbf{u}}^{\mathrm{L}}(\mathbf{x}) = \mathbf{0} \qquad \text{on } \Gamma^{\mathrm{GL}} \tag{8}$$

Figure 34 shows a schematic diagram of the deformation of the field near the crack front modeled based on the formulation by the mesh superposition method defined above. It can be understood that the field near the crack front, including the crack opening, is reproduced smoothly and in detail by superimposition of the local mesh and global mesh.

Based on the modeling described above, design variables for definition of the local mesh were set, and the domain of the local mesh was minimized under the constraint condition that it should be possible to provide the same local stress evaluation accuracy as in a conventional FEM analysis. The minimum mesh size was set at 50 μm, and the necessary degrees of freedom (DOF) when performing a crack propagation analysis for various crack lengths by the proposed method using the minimized local mesh ($DOF_{s\text{-}method}$) and the conventional method using the normal FEM method (DOF_{FEM}) were compared. The results are shown in Figure 35. The superiority of the proposed method based on the s-version of FEM became remarkable as the crack length increased, and in case of a crack length of 500 mm (10 000 steps), which was the longest crack length in the range of this study, the results showed that DOF can be reduced to only 7 % of that with the conventional technique. On the assumption that computational time depends only on DOF, considering the fact that the computational time by a linear solver is roughly proportional to the third power of DOF, this result suggests that it is possible to reduce computational time to 0.034 % of that with the conventional method by using the proposed method, showing that an extremely large numerical calculation cost improvement effect can be expected.

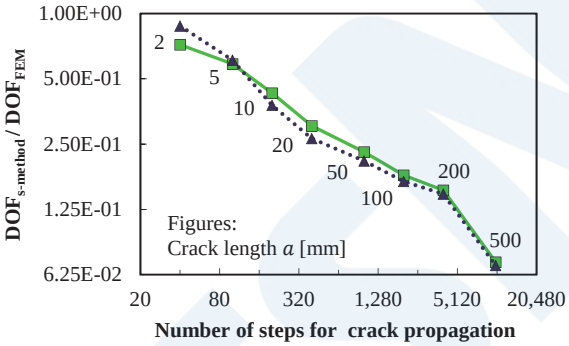

Figure 35　Numerical calculation cost improvement effect of proposed method based on s-version of FEM (mesh superposition method; here, DOF by the proposed method was normalized by DOF based conventional FEM) [9)]

7.4　Development of Dynamic Crack Propagation Analysis Method Based on S-Version of FEM (Expression of Crack Front Shape: 3D Model) [10)]

When considering actual brittle crack propagation phenomena, the crack front shape is assumed to be a curved curvilinear shape, and is not a shape which is known in advance. As methods for expressing this kind of crack front shape using conventional FEM, the following two approaches can be considered, as illustrated in Figure 36(a) and (b).

(1) A mesh in which the element boundaries are orthogonal at each node is adopted, corresponding to the structure, and nodes are not arranged along the crack front (rectangular mesh method, Fig. 36(a))

(2) Nodes are arranged with respect to the crack front, and remeshing is performed repeatedly accompanying crack propagation (remesh method, Fig. 36(b))

In the case of (1), mesh generation (modeling) is simple, but because the element boundary is not arranged on the crack front, the accuracy of the stress field around the crack front is sharply reduced. Therefore, this approach is inadequate for use in the application phase described in section 7.2, and application of the local critical fracture stress criterion is considered to be realistically impossible. On the other hand, in the case of (2), first, it is feared that the necessity of remeshing in each step will lead to an extremely high numerical calculation cost. Although retreat of the crack front due to the low plastic constraint placed on the region around the crack front is conceivable, because the mesh distortion in this area becomes remarkable, decreased evaluation accuracy is a concern. Moreover, generation of the mesh around the crack front by a simple plate structure is comparatively simple, but implementation of an extremely complicated mesh generation algorithm which considers the interaction with the crack front shape is necessary for application to arbitrary structural designs containing discontinuities, which is the ultimate goal of this research.

The advantages of developing a dynamic crack propagation analysis model based on the s-version of FEM are not limited to

the large "(2) Improvement of numerical calculation cost" described in the previous section, but also include rationally realizing "(3) Expression of crack front shape," which is difficult with conventional FEM techniques, as outlined above. The method of expressing the crack front shape based on the s-version of FEM is shown in Figure 36(c), which also shows the two above-mentioned conventional FEM approaches. The proposed method based on the s-version of FEM is considered to have superior features which cannot coexist in approaches based on conventional normal FEM, namely, (a) high accuracy, (b) low numerical calculation cost, (c) simple modeling and (d) simple algorithm.

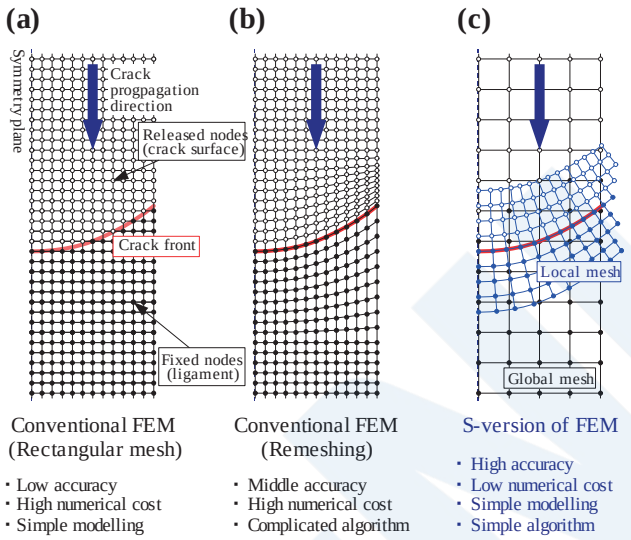

Figure 36 Expression of the crack front shape in proposed method based on the conventional method and s-version of FEM using normal FEM[10)]

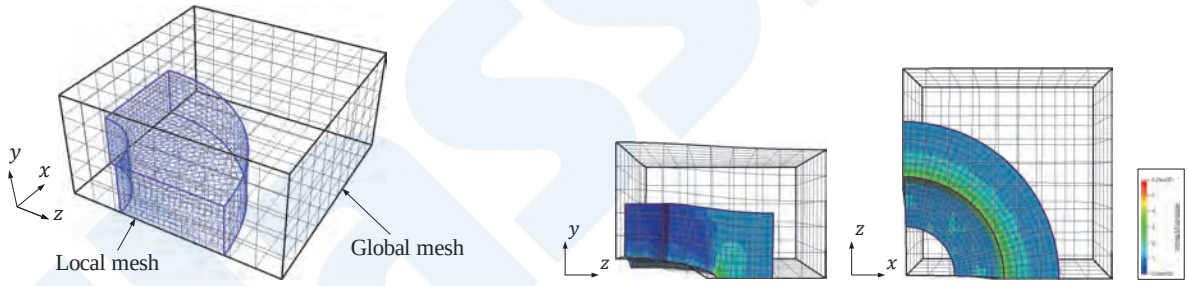

(a) Finite element mesh (b) Maximum principal stress distribution

Figure 37 Verification of accuracy of the 3-dimensional crack analysis model based on the s-version of FEM (showing only the local mesh for the stress field) [10)]

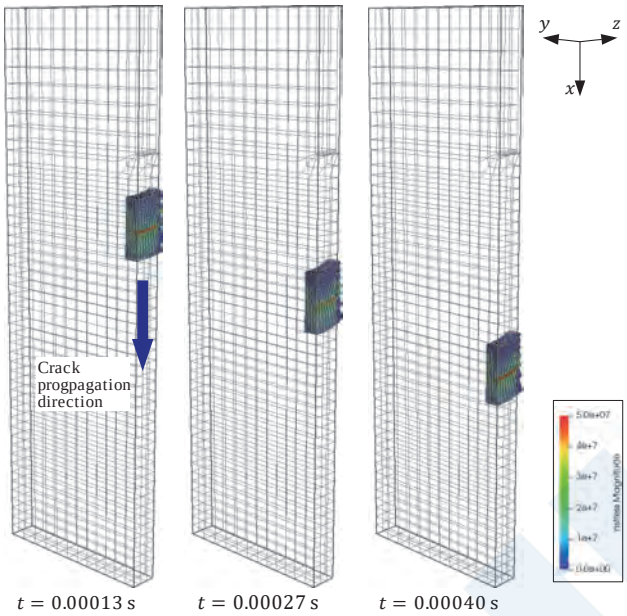

Figure 38　Application of the 3-dimensional crack analysis model based on the s-version of FEM to a rapid crack propagation test using a PMMA specimen (showing only the local mesh for the stress field) [10)]

Based on the concept described above, a dynamic crack propagation model for 3-dimensional elastic bodies was developed based on the s-version of FEM. First, as a basic study, the accuracy of the model was verified with a circular crack in an infinite solid with a known exact solution for the displacement field and the stress field. Figure 37 shows the mesh used and an example of the results of a stress analysis. As a difference from the 2-dimensional problem described in section 7.2, it was feared that this approach would affect accuracy if the global mesh and the local mesh intersect 3-dimensionally at the location ahead of the crack front. However, this analysis demonstrated that it is also possible to realize high accuracy equal to the case of 2 dimensions under any local stress condition. Figure 38 shows an example of a reproduction analysis of a crack propagating at high speed in a 3-dimensional plate structure assuming PMMA. As shown here, the basis of an unprecedented rapid crack propagation model, which can realize stress analysis satisfying both high accuracy and high efficiency in analyses of complex crack propagation behaviors, was successfully established.

8. CONCLUSIONS

This paper, entitled “Elucidation of the Mechanism of Brittle Crack Arrest and Recent Trends in Research for Establishment of a Method for its Rational Control,” has presented an overview centering on the results obtained by a group consisting of the author and others in the projects “Fracture mechanics research for elucidation of the long crack problem (August 2014 to March 2018)” and “Development of a fracture mechanics model for realization of structural arrest design (April 2018 to present, now continuing)” carried out with ClassNK as “Joint research at the request of industry.”

With the exception of the results reported in section 7.3 of this paper, all of these results have already been reported in leading international journals in the fields of fracture mechanics, mechanical engineering, material engineering or computational mechanics. On the occasion of this paper, the author will be happy if readers who have an interest in the respective research issues and results refer to the literature listed in References (Results Related to this Paper), which summarize these topics in detail.

In the development of the crack propagation models based on the mesh superposition method (s-version of FEM) described in Chapter 7, at present, the scope of application of this method is limited to elastic analysis, and extension to elastoplastic analysis applicable to steel structural members, which is the ultimate goal of this research, is still in the developmental stage. In study of the effects of microstructural factor of steel materials on brittle crack arrestability described in Chapter 5, only a very small portion of this problem has been elucidated so far, and further study is considered necessary in the future.

It goes without saying that control of the brittle crack propagation phenomenon is the most fundamental and important issue for securing the safety of basic structures, beginning with ships. Promotion of research aimed at elucidating the mechanism of this phenomenon and establishing a rational method for its control by collaboration between industry and academia is considered to be an extremely effective framework for linking new technologies created from the academic perspective to practical application as quickly as possible. The author hopes to make ongoing contributions to this goal by continuing the above-mentioned joint research.

REFERENCES

Results Related to this Paper

1) K. Shibanuma, F. Yanagimoto, T. Namegawa, K. Suzuki, S. Aihara, Brittle crack propagation/arrest behavior in steel plate - Part I: Model formulation, Engineering Fracture Mechanics 162 (2016), 324-340.
2) K. Shibanuma, F. Yanagimoto, T. Namegawa, K. Suzuki, S. Aihara, Brittle crack propagation/arrest behavior in steel plate - Part II: Experiments and model validation, Engineering Fracture Mechanics 162 (2016), 341-360.
3) F. Yanagimoto, K. Shibanuma, K. Suzuki, T. Matsumoto, S. Aihara. Local stress in the vicinity of the propagating cleavage crack tip in ferritic steel, Materials & Design 144 (2018), 361-373.
4) K. Shibanuma, F. Yanagimoto, K. Suzuki, S. Aihara, Brittle crack propagation/arrest behavior in steel plate - Part III: Discussions on arrest design, Engineering Fracture Mechanics 190 (2018), 104-119.
5) K. Shibanuma, Y. Suzuki, K. Kiriyama, K. Suzuki, H. Shirahata, A model of cleavage crack propagation in a BCC polycrystalline solid based on the extended finite element method, Acta Materialia 176 (2019) 232-241.
6) F. Yanagimoto, T. Hemmi, Y. Suzuki, Y. Takashima, T. Kawabata, K. Shibanuma, Contribution of grain size to resistance against cleavage crack propagation in ferritic steel, Acta Materialia 177 (2019), 96-106.
7) K. Kishi, F. Yanagimoto, T. Fukui, T. Matsumoto, K. Shibanuma, Analysis of rapid crack arrestability enhancement by structural factors in cross-joint components using a transparent elastic solid. International Journal of Mechanical Sciences 174 (2020), 105502.
8) F. Yanagimoto, K. Shibanuma, Y. Nishioka, Y. Shirai, K. Suzuki, T. Matsumoto, Local stress evaluation of rapid crack propagation in finite element analyses, International Journal of Solids and Structure 144-145 (2018), 66-77.
9) K. Kishi, Y. Takeoka, T. Fukui, T. Matsumoto, K. Suzuki, K. Shibanuma, Dynamic crack propagation analysis based on the s-version of the finite element method, Computer Methods in Applied Mechanics and Engineering 366 (2020), 113091.
10) K. Kishi, Rapid crack propagation experiments and development of mesh superposition model for structural arrest design, University of Tokyo Graduate School, master's thesis, 2020.

Others

11) Nippon Kaiji Kyokai (ClassNK), "Guidelines for brittle crack arrest design," (2009).
12) IACS. S33 Requirements for use of extremely thick steel plates. Requirements concerning strength of ships, 2013.
13) T. Inoue, T. Ishikawa, S. Imai, T. Koseki, K. Hirota, M. Tada, H. Kitada, Y. Yamaguchi, H. Yajima, Long crack arrestability of heavy-thick shipbuilding steels, Proceedings of the 16th International Offshore and Polar Engineering Conference, 2006
14) T. Kanazawa, S. Machida, H. Yajima, M. Aoki, Study on brittle crack arrester: Considerations on the arrest of a very long crack, Selected Papers from the Journal of the Society of Naval Architects of Japan 11 (1973), 135-47.
15) S. Machida, H. Yoshinari, S. Yasuda, S. Aihara, H. Mabuchi, Fracture mechanical modeling of brittle crack propagation and arrest of steel (1): A fundamental model, Journal of the Society of Naval Architects of Japan 177 (1995), 243-258.
16) K. Sugimoto, H. Yajima, S. Aihara, H. Yoshianri, K. Hirota, M. Toyoda, T. Kiyose, T. Inoue, T., Handa, T. Kawabata, T. Tani, A. Usami, Thickness effect on the brittle crack arrest toughness value (K_{ca}): Brittle crack arrest design for large container ships - 6, Proceedings of the 23rd International Offshore and Polar Engineering Conference, 2012.
17) F. Yanagimoto, K. Shibanuma, T. Matsumoto, K. Suzuki, Governing factors of the local tensile stress in the vicinity of a rapidly propagating crack tip in elastic-viscoplastic solids, Engineering Fracture Mechanics 218 (2019), 106548.

18) S. Aihara, Y. Tanaka, A simulation model for cleavage crack propagation in bcc polycrystalline solids, Acta Materialia 59 (2011), 4641-4652.
19) T. Handa, S. Suzuki, N. Kiji, M. Toyoda, T. Miyata, Effect of unwelded length on behaviour of brittle crack arrest in T-joint structure, Welding International 23 (2009), 640-647.
20) T. Handa, S. Igi, K. Oi, T. Tagawa, F. Minami, Brittle crack propagation/arrest behavior in T-joint structure of heavy gauge steel plate, Welding in the World 59 (2015), 823-838.
21) N. Moës, A. Gravouil, T. Belytschko, Non-planar 3D crack growth by the extended finite element and level sets - Part I: Mechanical model, International Journal of Numerical Methods in Engineering 53 (2002), 2549-2568.
22) A. Gravouil, N. Moës, T. Belytschko, Non-planar 3D crack growth by the extended finite element and level sets - Part II: Level set update, International Journal of Numerical Methods in Engineering 53 (2002), 2569-2586.
23) V. F. González-Albuixech, E. Giner, J. E. Tarancón, F. J. Fuenmayor, A. Gravouil, Domain integral formulation for 3-D curved and non-planar cracks with the extended finite element method, Computer Methods in Applied Mechanics and Engineering 264 (2013), 129-144.
24) J. Fish, The s-version of the finite element method, Computers & Structures 43 (1992), 539-547.

Simple Evaluation Method for Ultimate Strength of Rectangular Plates under Combined Load

Kinya ISHIBASHI* Toshifumi IKEMOTO** Akira TATSUMI*** Masahiko FUJIKUBO***

1. INTRODUCTION

Accurate evaluation of the buckling strength of plates and stiffeners, which are basic elements of the ship hull structure, is extremely important for safety assessments of ships. Conventionally, in ship classification rules, the ability of the various members comprising the hull structure to withstand compressive load was verified as a criterion for elastic buckling of plates, but because this approach results in an overly-conservative evaluation, particularly in the case of thin plates, criteria based on ultimate strength, which consider residual strength from elastic buckling until collapse, have become the general practice for plate buckling evaluations in recent years.

One technique for estimating the ultimate strength of plates under uniaxial compressive load is Faulkner's formula [1]. Faulkner clarified the fact that the buckling phenomena are arranged by the slenderness ratio based on discussions in collapse experiments, and proposed a simple, practical formula in which only the slenderness ratio β is used as a parameter. In formulas of this type, the boundary conditions, initial deflection conditions, etc. of the test specimen used in the experiment are implicitly reflected in the estimation formula. Subsequently, various other researchers [2) 3) 4)] proposed ultimate strength estimation formulas based on more rational boundary conditions and initial deflection conditions.

In order to design more optimal hull structures, the finite element method (FEM) has been used in recent years because direct consideration of complex structures and load distributions is possible. In this approach, the ultimate strength evaluation is carried out considering the combined load acting on a plate derived from FEM results. Simple, practical ultimate strength formulas which can consider this kind of combined load have also been proposed [5) 6) 7)] based on experimental research and numerical simulations and some have been adopted in the rules of ship classification societies. However, evaluation formulas do not provide an analytically explicit description of buckling and post-buckling behavior or the effects of plasticity. As a strength evaluation method which clarifies the physical background of these behaviors, Byklum et al.[8)] reproduced the buckling response after elastic buckling by an elastic large deflection analysis, and proposed a method for estimating ultimate strength by judging the onset of yielding at a predetermined position. This approach has also been extended to stiffened panels. However, since it is necessary to solve multi-variable simultaneous cubic equations when applying these techniques, numerical analysis methods, for example, using the Newton-Raphson method, is required.

Therefore, the authors developed an evaluation method for the ultimate strength of rectangular plates by formulating the controlling factors for ultimate strength, namely, elastic buckling, initial imperfections and yielding, as physically as possible, and express this method in an explicit formula which does not depend on numerical analysis techniques such as iterative convergent calculations.

In this paper, first, we carried out a series of nonlinear FEM calculations using a rectangular plate model applying simple support and "remain-straight-line" conditions along the edges of the plate in order to investigate the buckling behavior and collapse behavior of a rectangular plate under combined biaxial compressive/tensile and shear load. Based on the results of this series of calculations, we make a detailed investigation of the behaviors in the state when compressive load in plate longitudinal direction is dominant and the state when compressive load in the transvers direction is dominant, and identified the buckling phenomenon, which must be considered for an accurate strength evaluation, and the yielding phenomenon, which becomes the trigger for the buckling. Based on the results of this investigation, we propose a formula which can reproduce the buckling response of the plate under combined load and accurately evaluate ultimate strength by a judgment of yielding at a predetermined position. It should be noted that for the judgment of yielding we consider not only membrane stress but also out-plane bending stress, which is known to become a trigger for the collapse of thick plates.

* Hull Rules Development Dept., ClassNK
** Shin Kurushima Dockyard Co., Ltd.
*** Osaka University Graduate School of Engineering

2. COLLAPSE BEHAVIOR OF RECTANGULAR PLATES UNDER COMBINED LOAD

2.1 Analysis Conditions of Series Calculation

The behavior of rectangular plates from the occurrence of buckling until collapse was investigated by a collapse analysis by FEM taking into account the material and geometrical non-linearity. As the analysis model, a plate panel surrounded by stiffeners was considered, as shown in Figure 1, and simple support conditions were applied to the edges of the model. Further, "remain-straight-line" conditions were applied to the edges considering continuity with adjoining panels. Combined loads by 84 patterns of biaxial compressive/tensile and shear load was applied to rectangular plates with aspect ratios of 1.5 to 9 and plate thicknesses of 7.5 mm to 30 mm, and an analysis of the behavior of the rectangular plates until the plates collapsed and reduction of load carrying capacity was carried out by the incremental arc-length method. Table 1 shows the conditions of the analysis. As the initial deflection in this analysis, deflection of sine 1/2-half wave was assumed at the longitudinal edges, and cylindrical-shaped deflection was assumed in the central area, as shown by Eq. (5), which is presented later.

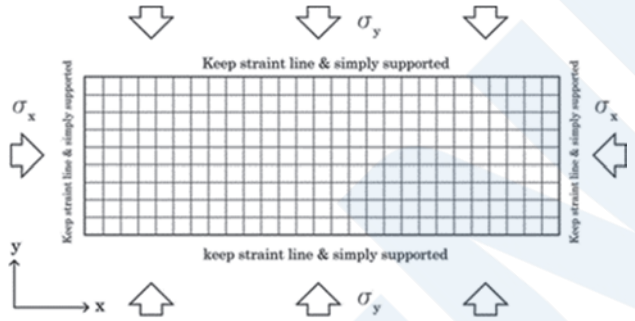

Figure 1 Analysis model.

Table 1 Model information and analysis conditions.

Dimensions (mm)	1200×800, 2400×800, 7200 × 800
Thickness (mm)	8 types of plate thickness: 7.5, 10.0, 12.5, 15.0, 17.5, 20.0, 25.0 and 30.0
Material	Yield stress 315MPa, Elasto–perfectly plastic material
Initial deflection	Cylindrical deflection mode
Amplitude of initial deflection	$0.005\beta^2 t$ β : Slenderness ratio
Load conditions	84 types of combined load conditions: $[\sigma_x; \sigma_y; \tau_{xy}] = [\cos\alpha_{xy}\,; \sin\alpha_{xy}\,; \alpha_\tau \tau_Y]$ $\alpha = 0,10,20,30,40,45,50,60,70,80,90,105,$ $120,135,150,165,285,300,315,330,345\ deg$ $\alpha_\tau = 0, 0.25, 0.5, 0.75$
Analysis Method	MSC.MARC, Arc-length method

2.2 Analysis Conditions of Series Calculations

2.2.1 Thin plates

In the case of a thin rectangular plate (thickness: 7.5 mm) subjected to compressive load in the longitudinal direction, deflection increases slightly, even under a low level of loading less than its elastic buckling strength, due to the existence of initial deflection, and when a larger compressive load is applied, the state exceeds the elastic buckling strength. In this stage, deflection in the multiple half-wave mode (m-half-wave × 1-half-wave sine mode) appears clearly in the longitudinal direction, corresponding to the aspect ratio of the plate, and deflection increases rapidly (Fig. 2(a)). Due to the tensile membrane stress caused by this large deflection, effectiveness for in-plane compressive stiffness decreases around the centerline in the

longitudinal direction of the rectangular plate, and in its place, compressive stress larger than the average compressive stress acts near the long sides (Fig. 2(a)). As a result, the plate collapses because full cross-section yielding occurs near the longitudinal sides, mainly due to in-plane compressive stress (Fig. 2(c)) and the area around the centerline cannot effectively support the in-plane compressive load as described above.

2.2.2 Thick plates

A rapid increase in deflection is not observed in a thick rectangular plate (thickness: 15 mm) subjected to compressive load in the longitudinal direction because the elastic buckling strength of thick plates is larger than that of thin plates. As in the thin plate, multiple half-wave deflection increases in the longitudinal direction, but before the distribution of longitudinal stress becomes remarkable (Fig. 3(a)) due to its effect, yielding occurs in the vicinity of the longitudinal centerline, mainly as a result of bending (Fig. 3(c)). Thus, in thick plates, it is thought that bending yielding at this position becomes the trigger of collapse of the rectangular plate.

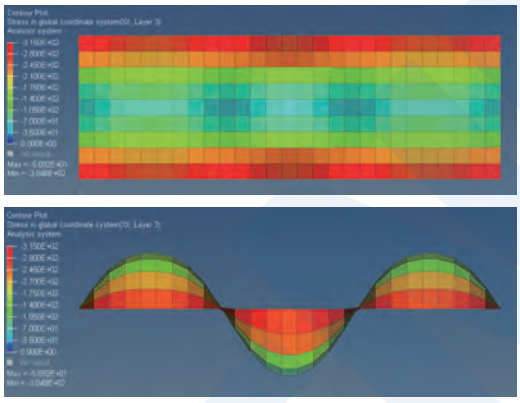

(a) Deformation (20 times) and component stress σ_x at thickness center

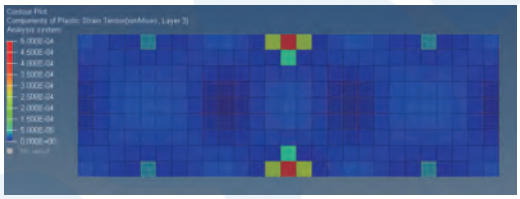

(b) Equivalent plastic strain at center of plate thickness

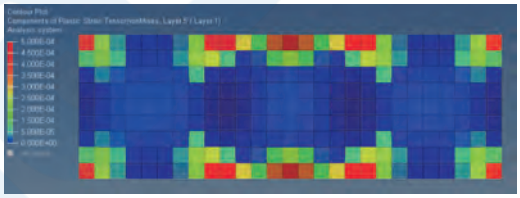

(c) Equivalent plastic strain at plate surface

Figure 2 Structural response of thin plate (7.5mm) at collapse stage

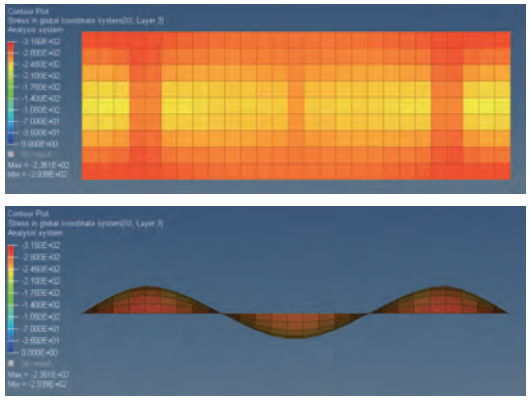

(a) Deformation (20times) and component stress σ_x at thickness center.

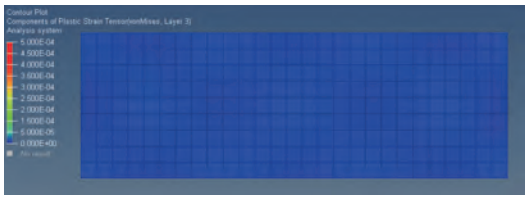

(b) Equivalent plastic strain at thickness center.

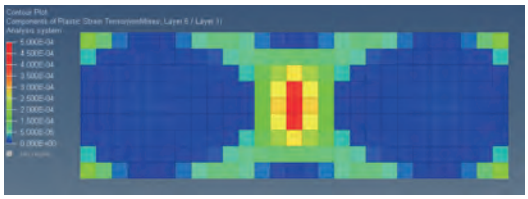

(c) Equivalent plastic strain at plate surface.

Figure 3　Structural response of thick plate (15.0mm) at collapse stage.

2.3　Collapse Behavior under Transverse Compressive Load

2.3.1　Thin plates

If a relatively thin rectangular plate is subjected to compressive load in the transverse direction, deflection increases even in under low-level compressive load because the elastic buckling strength of the plate is low, and as deflection increases, the buckling mode transitions from the sine wave mode of 1-half-wave × 1-half-wave to a roof-shape mode buckling shape as shown in Figure 4 (a). The in-plane stiffness near the center of the rectangular plate is reduced by the effect of this buckling deflection, and compressive stress exceeding the average compressive stress acts (Fig. 4(a)). Therefore, the rectangular plate collapses because full cross-sectional yielding occurs near the short sides, mainly due to in-plane compressive load (Fig. 4(b)) and the central part of the plate cannot effectively support the in-plane compressive load due to large buckling deflection.

2.3.2　Thick plates

In thick rectangular plates, the increase in deflection is not as rapid as in thin plates because the thick plates have greater elastic buckling strength than that of thin plates. Although buckling deflection in the sine mode of 1-half-wave × 1-half-wave is generated similar to that in thin plates, before the change in the buckling mode and distribution of stress in the transverse direction (Fig. 5(a)) become remarkable, yielding occurs in the central part of the plate, mainly due to bending (Fig. 5(c)). In thick plates, it is thought that yielding at this position becomes the trigger for collapse of rectangular plates.

2.3.3　Change of buckling mode

As a difference from the buckling behavior observed under longitudinal compressive load, in the case of transverse compressive load, the buckling mode changes from the sine-wave mode to the roof-shape mode as buckling deflection increases. The buckling shape function was defined as shown in Figure 6 to quantitatively express the buckling mode, which changes continuously. When the end-part length c, which shows the total length of Area I in the function, is equal to a, the buckling mode becomes the sine-wave mode of 1-half-wave × 1-half-wave. Using the least-squares method, the length c shown in Figure 6 in each of the loading states was calculated from the distribution of buckling deflection obtained by nonlinear FEM analysis, and the transition of the length c from the occurrence of elastic buckling until collapse of the plate was graphed as shown in Figure 7.

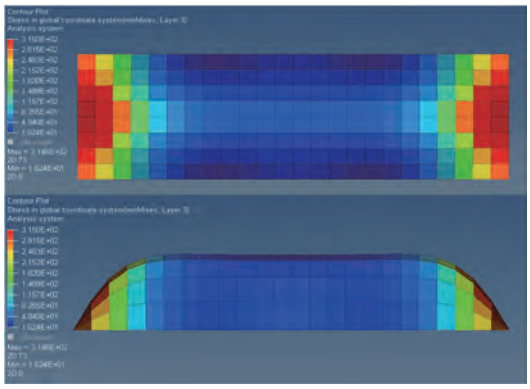

(a) Deformation (20 times) and component stress σ_x at thickness center

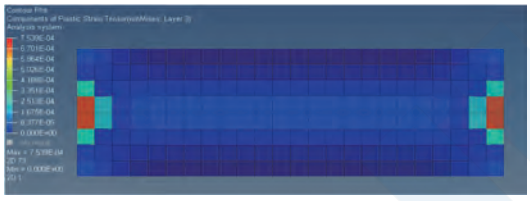

(b) Equivalent plastic strain at center of plate thickness

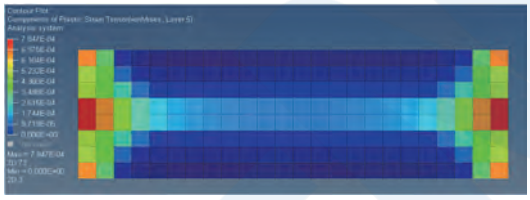

(c) Equivalent plastic strain at plate surface

Figure 4 Structural response of thin plate (7.5mm) at collapse stage

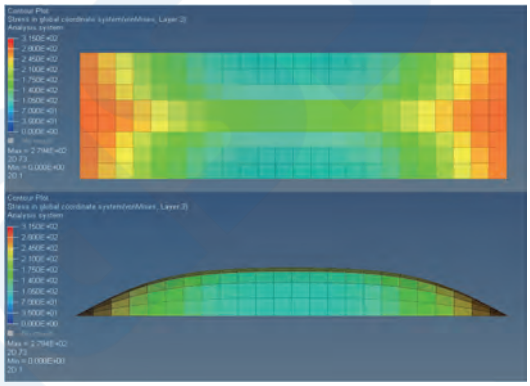

(a) Deformation (20 times) and component stress σ_x at thickness center

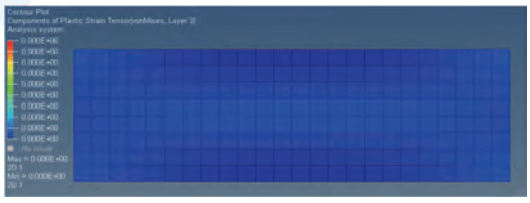

(b) Equivalent plastic strain at thickness center

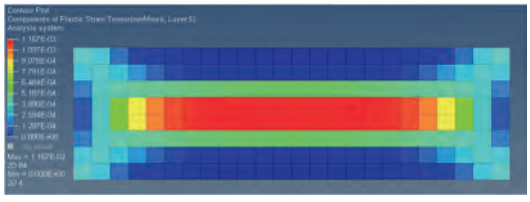

(c) Equivalent plastic strain at plate surface

Figure 5 Structural response of thick plate (15.0mm) at collapse stage

Here, the right end of each curve shows the end-part length c and the load value at the time of ultimate strength. The abscissa shows values obtained by nondimensionalizing the compressive load by the elastic buckling stress. Although the transition of the end-part length c follows almost the same curve independent of the plate thickness, the timing when ultimate strength is reached differs depending on the plate thickness. That is, in the thin plate, the end-part length c has a value close to the plate width b, whereas in the thick plate, c approaches the plate length a, which means that collapse occurs in a mode approximating the 1 half-width × 1 half-width mode. In the case of a long, slender rectangular plate with an aspect ratio of 9, the change in the buckling mode is more rapid, and the timing of the transition to the roof-shape mode is earlier.

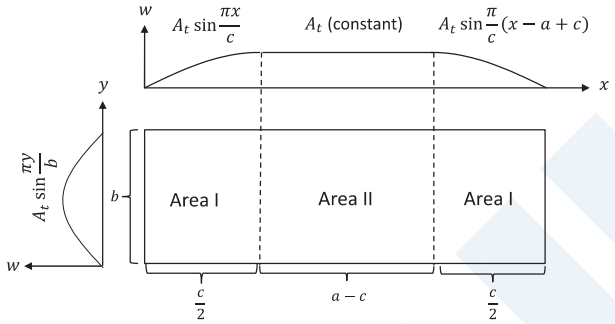

Figure 6　Definition of buckling shape function

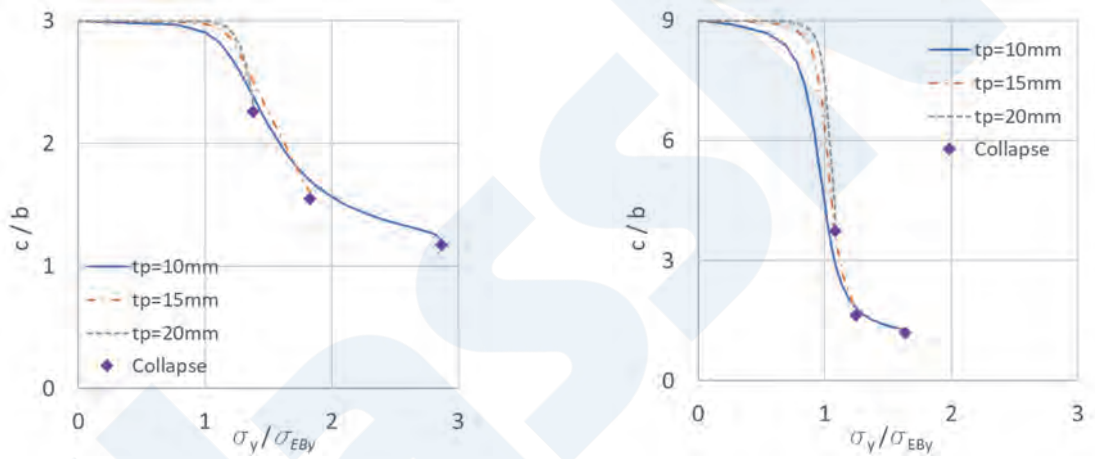

(a)　Aspect ratio 3 (2400×800mm)　　(b)　Aspect ratio 9 (7200x800mm)

Figure 7　End-part length c and load relationship

3.　REPRODUCTION OF STRUCTURAL RESPONSE OF RECTANGULAR PLATE BY ELASTIC LARGE DEFLECTION THEORY

3.1　Evaluation Method Based on Mathematical Expression Reproducing Buckling Response

As described in Chapter 2, a decrease in in-plane stiffness and change in the stress distribution occur due to the effects of buckling and large deflection in rectangular plates with initial deflection and are subjected to longitudinal compressive load or transverse compressive load. However, large-scale yielding does not occur until immediately before the plate collapses, and the yielding region expands suddenly immediately just before collapse. Considering this general feature of the collapse behavior of rectangular plates, if it is possible to carry out an elastic large deflection analysis and to make a judgment of yielding at the position which becomes the trigger of collapse based on the results of that analysis, it is thought that an evaluation method consisting of physically meaningful formulas can be proposed. The method proposed by Byklum et al.[8] mentioned in the Introduction takes such an approach. However, this method doesn't become a simple ultimate strength estimation method, as it is necessary to adopt a numerical analysis method, for example, using the incremental method, to solve multi-variable

simultaneous cubic equations. Therefore, the authors carried out an elastic large deflection analysis, for which we selected the one deflection mode that makes the largest contribution to collapse, and attempted to estimate the ultimate strength of a rectangular plates with high accuracy by making yielding judgments.

3.2 Case in which Longitudinal Compressive Load is Dominant

Based on the policy described in section 3.1, the function expressing the sine wave mode of m-half-wave × 1-half-wave, which is the deflection shape with the smallest buckling mode corresponding to longitudinal compressive load, and the function expressing the initial deflection are defined as shown in Eq. (1) and Eq. (2), respectively. The Airy stress function is then obtained by inserting these equations into an equation of compatibility that considers the effect of large deflection, which is expressed by Eq. (3), and the in-plane stress components and in-plane strain components due to the influence of large deflection can be obtained.

$$w = A_l \sin\frac{m\pi x}{a} \sin\frac{\pi y}{b} \tag{1}$$

$$w_0 = A_{l0} \sin\frac{m\pi x}{a} \sin\frac{\pi y}{b} \tag{2}$$

$$\frac{\partial^4 F}{\partial x^4} + 2\frac{\partial^4 F}{\partial x^2 \partial y^2} + \frac{\partial^4 F}{\partial y^4} = E\left\{\left(\frac{\partial^2 w}{\partial x \partial y}\right)^2 - \left(\frac{\partial^2 w}{\partial x^2}\right)\left(\frac{\partial^2 w}{\partial y^2}\right) - \left(\frac{\partial^2 w_0}{\partial x \partial y}\right)^2 + \left(\frac{\partial^2 w_0}{\partial x^2}\right)\left(\frac{\partial^2 w_0}{\partial y^2}\right)\right\} \tag{3}$$

The results are added to the stress components and strain components due to the normal linear response, and the quantities of work of external force and internal force when small deflection δA_l occurs is calculated, taking into account these nonlinear stress and strain components. According to the principle of virtual work, these quantities of work have the same value. Therefore, Eq. (4) can be derived as a cubic equation showing the relationship between the biaxial average stresses σ_{x0}, σ_{y0} acting on a rectangular plate and deflection A_l. The derivation process of Eq. (4) is presented in Appendix 1.

$$\alpha_2 A_l^3 + (\alpha_3 - \alpha_1 - A_{l0}^2 \alpha_2) A_l - A_{l0}\alpha_3 = 0 \tag{4}$$

$$\alpha_1 = \frac{\pi^2}{4}\left(\sigma_{x0}\frac{m^2 b}{a} + \sigma_{y0}\frac{a}{b}\right)t \tag{4a}$$

$$\alpha_2 = \frac{\pi^4 E}{64}\left(\frac{m^4 b}{a^3} + \frac{a}{b^3}\right)t \tag{4b}$$

$$\alpha_3 = \frac{\pi^4 E}{48(1-\nu^2)}\left(\frac{m^4 b}{a^3} + \frac{a}{b^3} + \frac{2m^2}{ab}\right)t^3 \tag{4c}$$

Here, it may be noted that deflection A_l in the cubic equation shown in Eq. (4) can be obtained easily by using Cardano's formula (see Appendix 2). Furthermore, as shown in Eq. 4(a), this equation can consider not only longitudinal compressive load, but also the effect of transverse load.

In order to verify Eq. (4), the deflection obtained by Eq. (4) was compared with the result of a nonlinear FEM analysis. Figure 8(a) shows the comparison of the deflection obtained by Eq. (4) and a nonlinear FEM analysis considering the same initial deflection shape, where the abscissa shows the longitudinal compressive load applied to the rectangular plate. In the nonlinear FEM results shown by the broken lines, the rectangular plate collapses and deflection increases accompanied by a decrease in the load carrying capacity. In contrast, with Eq. (4), load and deflection continue to increase without this decrease in the load carrying capacity because the effect of yielding is not considered. However, the results show substantially the same response until the timing of ultimate strength and the yield strength decrease obtained by the nonlinear FEM analysis.

Figure 8(b) shows the transition of the longitudinal stress in the vicinity of the edges, which is thought to trigger collapse in thin plates. In this comparison as well, the results obtained with Eq. (4) show good agreement with the results of the nonlinear

FEM analysis until immediately before collapse of the rectangular plate. In the nonlinear FEM analysis, the fact that collapse occurs before the longitudinal stress reaches yield stress σ_Y is attributed to the compressive stress generated in the longitudinal direction due to the large deflection caused by buckling at the said position, together with the tensile stress generated in the transverse direction.

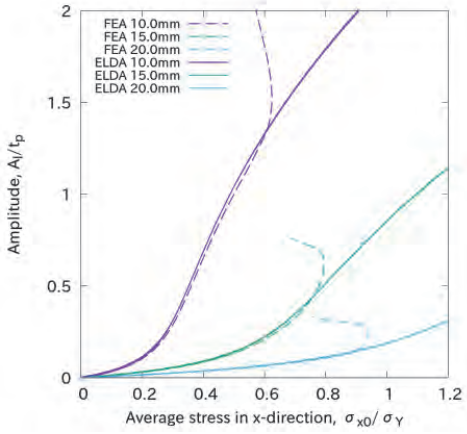

(a) Average stress – deflection

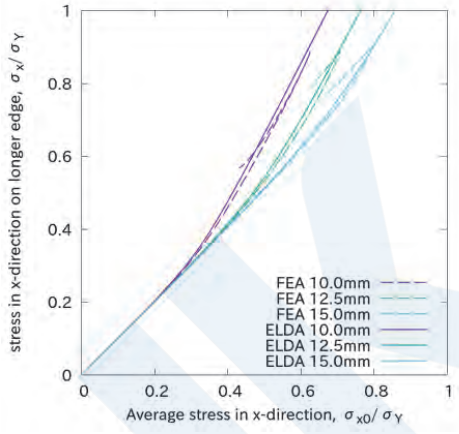

(b) Average stress - component stress σ_x at longer edge

Figure 8　Comparison between NLFEA and ELDA based formula

3.3　Case in which Compressive Load in Transverse Direction is Dominant

In cases where transverse compressive load is dominant, the buckling mode changes when buckling deflection is developed, as described in section 2.3. A method which can consider this change is necessary. The stress components and strain components generated as effects of large deflection were calculated by the same method as in section 3.2 using Eq. (5), which is a deflection shape function that can continuously express the change in the buckling mode shown in Figure 6.

$$w_I = A_t \sin\frac{\pi x}{c} \sin\frac{\pi y}{b} \qquad \text{for } x < \frac{c}{2} \tag{5a}$$

$$w_I = A_t \sin\frac{\pi}{c}(x - a + c) \sin\frac{\pi y}{b} \qquad \text{for } a - \frac{c}{2} < x \tag{5b}$$

$$w_{II} = A_t \sin\frac{\pi y}{b} \qquad \text{for } \frac{c}{2} \le x \le a - \frac{c}{2} \tag{5c}$$

Based on the principle of virtual work, a cubic equation showing the relationship between the biaxial average stresses σ_{x0}, σ_{y0} acting on a rectangular plate and deflection A_t is derived, as shown in Eq. (6). The derivation process of Eq. (6) is presented in Appendix 1.

$$\alpha_2 A_t^3 + (\alpha_3 - \alpha_1 - A_{t0}^2\alpha_2)A_t - A_{t0}\alpha_3 = 0 \tag{6}$$

$$\alpha_1 = \frac{\pi^2}{4}\left(\sigma_{x0}\frac{b}{c} + \sigma_{y0}\frac{2a - c}{b}\right)t \tag{6a}$$

$$\alpha_2 = \frac{\pi^4 E}{64}\left(\frac{b}{c^4} + \frac{3c}{b^3} - \frac{2c^2}{ab^3}\right)t \tag{6b}$$

$$\alpha_3 = \frac{\pi^4 E}{48(1-\nu^2)}\left(\frac{2a}{b^3} + \frac{b}{c^3} - \frac{c}{b^3} + \frac{2}{bc}\right)t^3 \tag{6c}$$

The deflection A_t in the cubic equation shown in Eq. (6) can be obtained easily by applying Cardano's formula (see Appendix 2) if the dimensions of the rectangular plate, the stresses σ_{x0}, σ_{y0} and the end-part length c expressing the buckling shape are given.

For verification of Eq. (6), the deflection calculated by Eq. (6) was compared with the solution of the nonlinear FEM analysis, which does not consider yielding.

Figure 9 is a comparison of the deflection obtained by the nonlinear FEM analysis and the deflection obtained by an elastic large deflection analysis by Eq. (6), where the abscissa shows the transverse compressive load applied to the rectangular plate. In the calculations using Eq. (6), deflections were calculated for several different end-part lengths c, which express the buckling mode. From Figure 9, good agreement between the envelope of the results of the elastic large deflection analysis obtained with the various values of end-part length c and the results of the nonlinear FEM analysis can be confirmed. In addition, the end-part length c of the elastic large deflection solution which showed good agreement with the amount of deflection also showed good agreement with the buckling mode obtained by the nonlinear FEM analysis at that timing. Some degree of error will occur if consideration is limited to only the end-part length c for the two cases when buckling deflection occurs and when deflection is sufficiently developed, for example, as shown in Figure 9, only c/b = 3.0 (sine wave mode of 1-half-wave × 1-half-wave) and c/b = 1.0. Nevertheless, it is considered possible to approximate deflection with generally good accuracy in the stress region that must be considered when evaluating ultimate strength. When reproducing the behavior of buckling mode changes by an elastic large deflection analysis, it is usually necessary to set the multiple buckling mode amplitudes as unknown quantities, which results in a multi-variable cubic equation that requires iterative convergent calculations. In this paper, the authors propose an explicit method for estimation of deflection which does not require iterative calculations by considering the buckling modes of two typical cases individually.

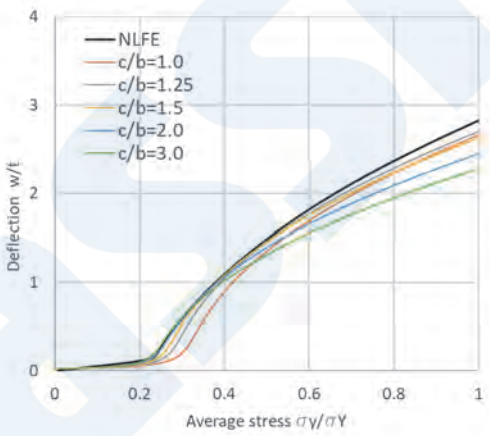

Figure 9 Comparison on buckling deflection between NLFEA and ELDA based formula, 2400×800×15.0mm

4. JUDGMENT OF RECTANGULAR PLATE COLLAPSE

4.1 Two Types of Collapse Judgment

Under both longitudinal compressive load and transverse compressive load, it is thought that the deflection mode until ultimate strength is achieved can be approximated by the deflection modes assumed in Chapter 3. Furthermore, based on the observation of the collapse behavior described in Chapter 2, it can be thought that the occurrence of the two types of yielding shown in Table 2 acts as the trigger for collapse. Therefore, we propose a new estimation method for the ultimate strength of rectangular plates, as described in the following sections.

Table 2　Two types of collapse conditions

Collapse condition A	Yielding due to in-plane compression from a position (Point A_1), which is the center of a longitudinal buckling half-wave along the longer edge, or in the vicinity of the transverse center along the shorter edge (Point A_2)
Collapse condition B	Yielding due to bending around the central part (Point B) of the rectangular plate

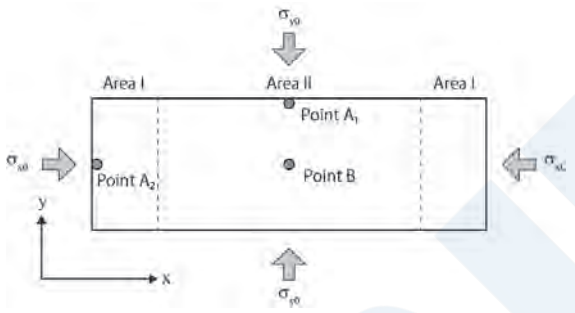

Figure 10　Positions of check point

4.2　Collapse by In-Plane Compression (Collapse Condition A)

Referring to the distribution of plastic strain at the instant of collapse shown in Figure 2(b) and Figure 4(b), in collapse condition A in Table 2, it is judged that a rectangular plate collapses when the von Mises equivalent stress associated with in-plane stress at Point A_1 or Point A_2 reaches the yield stress of the material.

More specifically, in cases where longitudinal compressive load is dominant, the additional stresses σ_{xm} and σ_{ym} expressed by Eq. (7a) and Eq. (7b), which consider the effect of the large deflection discussed in Chapter 3, are added to the biaxial average compressive stresses σ_{x0} and σ_{y0}, and a judgment is made from Eq. (7), which is used to obtain the von Mises equivalent stress. Due to large deflection, compressive stress acts in the longitudinal direction and tensile stress acts in the transverse direction at Point A_1, as shown in Eq. (7a) and Eq. (7b), resulting in a condition of combined tensile stress and compressive stress, and yielding occurs rapidly.

When transverse compressive load is dominant, the judgment is also made by Eq. (7), considering the additional stresses σ_{xm} and σ_{ym} expressed by Eq. (7c) and Eq. (7d) generated at Point A_2.

$$(\sigma_{x0}+\sigma_{xm})^2-(\sigma_{x0}+\sigma_{xm})(\sigma_{y0}+\sigma_{ym})+(\sigma_{y0}+\sigma_{ym})^2=\sigma_Y^2 \tag{7}$$

The additional stresses at Point A_1:

$$\sigma_{xm}=\frac{(A_l^2-A_{l0}^2)E}{8}\left(\frac{m\pi}{a}\right)^2 \tag{7a}$$

$$\sigma_{ym}=-\frac{(A_l^2-A_{l0}^2)E}{8}\left(\frac{\pi}{b}\right)^2 \tag{7b}$$

The additional stresses at Point A_2:

$$\sigma_{xm}=-\frac{(A_t^2-A_{t0}^2)E}{8}\left(\frac{\pi}{c}\right)^2 \tag{7c}$$

$$\sigma_{ym}=\frac{(A_t^2-A_{t0}^2)E}{8}\left(\frac{\pi}{b}\right)^2\left(2-\frac{c}{a}\right) \tag{7d}$$

4.3　Collapse by Bending (Collapse Condition B)

Referring to the plastic strain distribution at the instant of collapse of a comparatively thick plate, under collapse condition B in Table 2, it is judged that yielding occurs as a result of bending moment and in-plane force in two axial directions at Point B

in Figure 10. When a plate is subjected simultaneously to a bending moment and in-plane force, initial yielding occurs at the surface of the plate, the yielding region then expands toward the center-of-thickness of the plate, and yielding finally reaches a condition of full cross-section yielding. However, in order to judge that a plate has collapsed, it is necessary to specify what state in this process represents plate collapse.

Figure 11 shows the solutions of an elastic large deflection FEM analysis, an elastoplastic large deflection FEM analysis and an elastic large deflection analysis using Eq. (6), where the abscissa shows transverse compressive load and the ordinate shows deflection. The timing of initial yielding is in good agreement in the elastic large deflection analyses by nonlinear FEM and the equation. Initial yielding occurs on the plate surface on the compression side of bending, which is superimposed on in-plane compressive load, as in Figure 12. After initial yielding, the amount of deflection in the solution by nonlinear FEM which considers yielding increases in comparison with the other solutions because the bending stiffness decreases due to yielding. The stress state at the timing of ultimate strength is a state in which yielding also occurs at the surface on the tension side of bending, which has a mutually cancelling effect with in-plane compressive load. On the other hand, the elastic large deflection analysis, the timing of full cross-section yielding obtained occurs later than the actual ultimate strength. The factors responsible for this difference are thought to be an increase in deflection caused by the decrease in stiffness due to yielding, and collapse of the plate in a yielding state prior to full cross-section yielding. From this discussion, it can be understood that the rectangular plate collapses and ultimate strength is reached between the timing of initial yielding and full cross-section yielding obtained from the elastic large deflection analysis. Accordingly, an equation which combines the initial yielding condition expressed by Eq. (8) and the full cross-section yielding condition [9] is adopted as the collapse judgment method for collapse condition B. Here, a uniform value of $\alpha = 0.5$ was adopted for α in Eq. (8) based on the nonlinear FEM solution.

$$Y^2 = \alpha Y_0^2 + (1-\alpha) Y_1^2 = 1 \tag{8}$$

$$Y_0^2 = Q_n + 2.25 Q_m + 3|Q_{nm}| \tag{8a}$$

$$Y_1^2 = Q_n + 0.5 Q_{nm} + \sqrt{0.25 Q_m^2 + Q_{nm}^2} \tag{8b}$$

$$Q_n = n_x^2 - n_x n_y + n_y^2 \tag{8c}$$

$$Q_m = m_x^2 - m_x m_y + m_y^2 \tag{8d}$$

$$Q_{nm} = n_x m_x - n_y m_y - 0.5(n_x m_y + n_y m_x) \tag{8e}$$

$$n_x = (\sigma_x + \sigma_{xm})/\sigma_Y, \quad n_y = (\sigma_y + \sigma_{ym})/\sigma_Y \tag{8f}$$

$$m_x = \frac{M_x}{M_P}, m_y = \frac{M_y}{M_P}, \qquad M_P = \frac{t^2}{4}\sigma_Y \tag{8g}$$

In case longitudinal compressive load is dominant:

$$\sigma_{xm} = -\frac{(A_l^2 - A_{l0}^2)E}{8}\left(\frac{m\pi}{a}\right)^2 \tag{8h}$$

$$\sigma_{ym} = -\frac{(A_l^2 - A_{l0}^2)E}{8}\left(\frac{\pi}{b}\right)^2 \tag{8i}$$

$$M_x = \frac{(A_l - A_{l0})E}{12}\left(\frac{m\pi}{a}\right)^2 t^3 \tag{8j}$$

$$M_y = \frac{(A_l - A_{l0})E}{12}\left(\frac{\pi}{b}\right)^2 t^3 \tag{8k}$$

In case transverse compressive load is dominant:

$$\sigma_{xm} = 0 \tag{8l}$$

$$\sigma_{ym} = -\frac{(A_t^2 - A_{t0}^2)E}{8}\left(\frac{\pi}{b}\right)^2 \frac{c}{a} \tag{8m}$$

$$M_x = 0 \tag{8n}$$

$$M_y = \frac{(A_t - A_{t0})E}{12}\left(\frac{\pi}{b}\right)^2 t^3 \tag{8o}$$

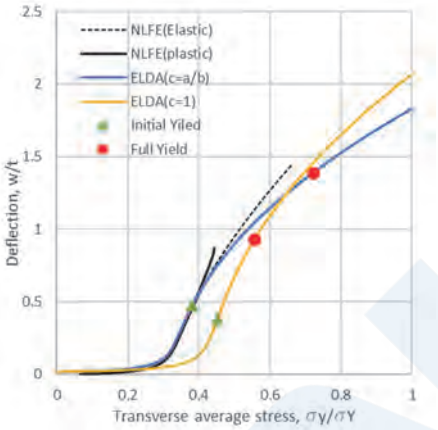

Figure 11　Deflection – load relationship and timings of initial yielding and fully yielding (2400×800×17.5mm)

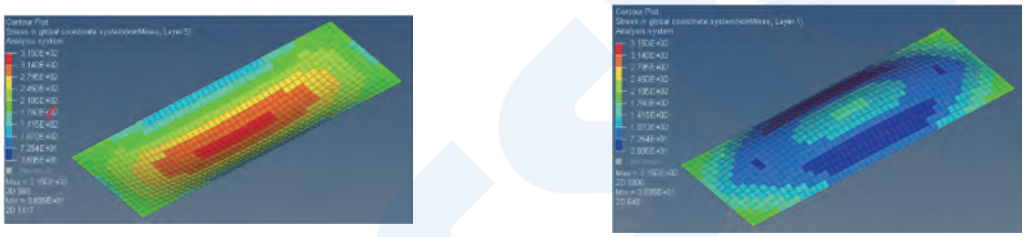

(a)　Compression side　　(b)　Tension side

Figure 12　Von Mises stress at initial yielding stage (2400×800×17.5mm)

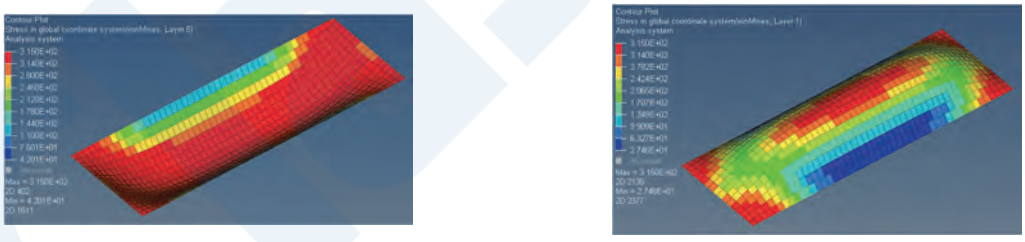

(a)　Compression side　　(b)　Tension side

Figure 13　Von Mises stress at ultimate strength

4.4　Verification of Collapse Condition

In order to verify the accuracy of the collapse judgment method for evaluation of the ultimate strength of rectangular plates proposed in sections 4.2. and 4.3, the results of this method were compared with the ultimate strength obtained by nonlinear FEM analysis under various conditions. When deriving the ultimate strength of a rectangular plate by this collapse judgment method, it is necessary to change the load acting on the rectangular plate and find a value which satisfies the collapse judgment equation. The ultimate strength correlation equation provided in the IACS Common Structural Rules Chapter 8, Section 5.3 uses the same approach.

Figure 14 shows a comparison of the ultimate strength under a condition of longitudinal uniaxial compression for the two collapse conditions A and B, where the slenderness ratio β is shown on the abscissa. The deflection shape used in the evaluation method is the deflection shape of the sine wave mode of 3-half-wave × 1-half-wave, which gives the smallest buckling strength

for plates with an aspect ratio of 3. The blue and orange curves in the graph show the values of ultimate strength derived by collapse conditions A and B in Table 2, respectively. All values on the lower side are the estimated values of ultimate strength given by the evaluation method proposed in this paper. The results show good agreement with the nonlinear FEM results, independent of the magnitude of the slenderness ratio. Moreover, the respective collapse behaviors of thick plates and thin plates shown in section 2.2 also show good agreement when the magnitudes of the ultimate strength for collapse condition A (collapse by in-plane compression) and collapse condition B (bending collapse) are replaced according to the slenderness ratio. Figure 14 also shows the estimated values of ultimate strength calculated by Faulkner's formula. It is known that Faulkner's formula shows somewhat low strength values because the initial imperfections in the crushing tests were large, among other factors.

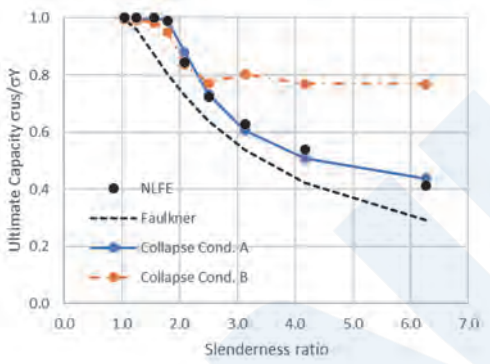

Figure 14 Comparison of ultimate strength against longitudinal compression between NLFEA and ELDA based formula (2400x800mm)

Figure 15 shows the accuracy of the proposed estimation method for ultimate strength under transverse uniaxial compressive load, where the slenderness ratio β is shown on the abscissa. As an object of comparison, the figure also shows the plots for a nonlinear FEM solution and the values given by the ultimate strength estimation equation shown in Eq. (9), which was developed by one of the authors.

$$\frac{\sigma_{us}}{\sigma_Y} = \frac{a}{b}\left(\frac{2.4}{\beta} - \frac{1.4}{\beta^2}\right) + \left(1 - \frac{a}{b}\right)\left(\frac{0.06}{\beta} + \frac{0.6}{\beta^2}\right) \qquad (9)$$

The orange and blue curves in the graphs are the results when the length c in Figure 6, which shows the various buckling modes, was replaced with a and b, respectively. When the slenderness ratio is large, the estimated value of the ultimate strength given by $c = b$ is smaller than that for $c = a$, and when the slenderness ratio is small, this relationship is reversed. Moreover, the estimated ultimate strength value of the smaller of the two shows results with good agreement with the nonlinear FEM solution. This tendency is also consistent with the relationship between the plate thickness and buckling mode at the time of ultimate strength described in section 3.3. The large aspect ratio (Fig. 15(b)) and small aspect ratio (Fig. 15(c)) also show the same tendency, and good agreement with the nonlinear FEM results was obtained regardless of the aspect ratio of the rectangular plate. Thus, these results confirmed that a judgment with good accuracy is possible if collapse judgments are made for the two cases c = a and c= b, and the lower estimated ultimate strength is adopted. Although Eq. (9) gives a comparatively good approximation on the conservative side, the proposed method shows closer agreement with the FEM analysis results.

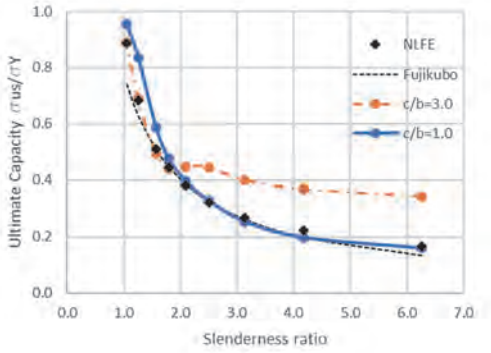

(a) Aspect ratio 3 (2400×800mm)

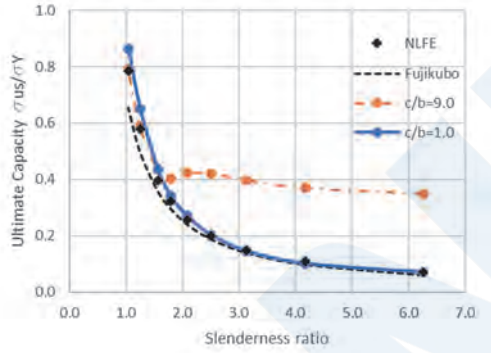

(b) Aspect ratio 9 (7200×800mm)

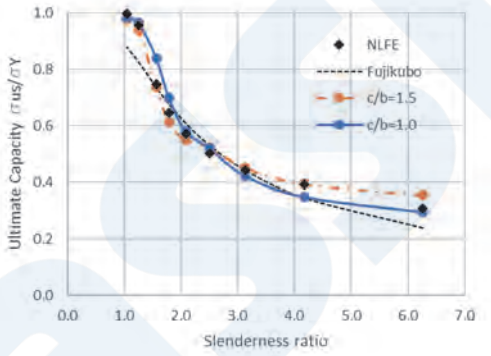

(c) Aspect ratio 1.5 (1200×800mm)

Figure 15 Comparison of ultimate strength against uniaxial compression between NLFEA and ELDA based formula

Next, Figure 16 shows the results of a verification by comparison with the nonlinear FEM results under biaxial in-plane load. In these graphs, the abscissa shows longitudinal load, and the ordinate shows transverse load. These graphs show the ultimate strength correlation curves obtained by the proposed evaluation method corresponding to longitudinal compressive load and transverse compressive load, which are compared with the nonlinear FEM solutions.

In the ultimate strength correlation equations corresponding to longitudinal compressive load and transverse compressive load, the results show good agreement with the nonlinear FEM solutions when the respective assumed collapse modes are in agreement. However, when the collapse modes are not in agreement, the equations give a non-conservative evaluation of ultimate strength. As a result, an accurate evaluation is possible if the values on the lower sides of two curves of the ultimate strength correlations are adopted.

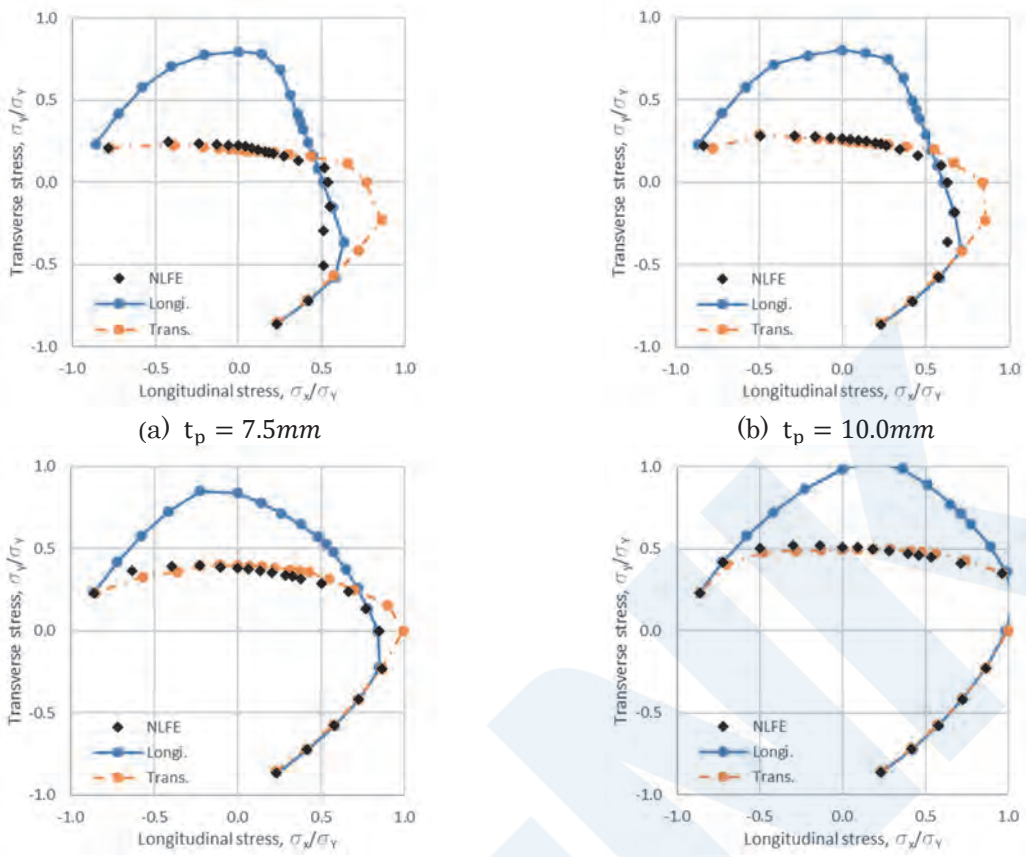

(a) $t_p = 7.5mm$ (b) $t_p = 10.0mm$

(c) $t_p = 15.0mm$ (d) $t_p = 20.0mm$

Figure 16 Comparison of correlation curves of ultimate strength (2400×800mm)

The treatment of the evaluation results for $c = a$ and $c = b$ in the evaluation method corresponding to transverse compressive load, and the treatment of the results of the evaluation methods corresponding to longitudinal compressive load and transverse compressive load described above, are both the same. That is, an accurate estimation is possible if the evaluations for the two cases are carried out separately, and the case with the lower estimated strength is used. The proposed evaluation method has this feature because it consists of physically-meaningful equations. Because buckling collapse has the physical property of occurring in the weakest mode, in which buckling occurs most easily, an estimation with high accuracy is possible if a shape function close to the weakest mode is considered. Conversely, if the shape function is substantially different from the weakest mode, strength will be overestimated, resulting in an unsafe estimation.

In the case of longitudinal compressive load and transverse tensile load, the proposed evaluation method may give a somewhat unsafe evaluation; this is particularly remarkable in thin plates, as shown in Figure 16(a). Under this load condition, the deflection mode changes in the loading process, as shown in Figure 17, deflection in the 5-half-wave mode develops, and the plate collapses. Here, the fact that the buckling mode is different from the sine wave mode of 3-half-wave × 1-half-wave for a plate panel with an aspect ratio of 3 assumed in the proposed evaluation method becomes an error factor. However, we have confirmed that an accurate estimation is possible, even under this load condition, if the evaluation is conducted assuming a deflection function of the 5-half-wave mode.

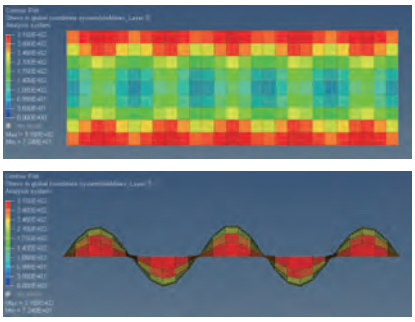

Figure 17　von Mises equivalent stress and deformations($t_p = 12.5mm$, compression/tension condition)

5. CONCLUSION

With the aim of developing a simple technique consisting of physically-meaningful equations that can estimate the ultimate strength of rectangular plates under various types of combined load, in this paper, the authors proposed evaluation methods for states in which longitudinal compressive load is dominant and states in which traverse compressive load is dominant.

First, nonlinear FEM series calculations were performed in order to investigate the collapse behavior of rectangular plates under longitudinal compressive load and transverse compressive load, respectively.

Next, deflection shape functions expressing the buckling mode were defined corresponding to longitudinal compressive load and transverse compressive load, respectively. Equations for estimating the load-deflection relationship and the load-additional stress relationship were derived based on elastic large deflection theory, and their accuracy was verified by comparison with the results of a nonlinear FEM analysis.

In addition, an ultimate strength judgment method was also proposed based on two types of collapse trigger mechanisms, namely, a membrane yielding type trigger and a bending yielding type trigger. The ultimate strength obtained by this method was compared with the results of a nonlinear FEM analysis, the accuracy of this method was verified. The knowledge obtained through this research is summarized below.

(1) In a rectangular plate subjected to longitudinal compressive load, under the initial deflection assumed here, initial buckling occurs in the sine wave mode of m-half-wave × 1-half-wave, corresponding to the aspect ratio of the rectangular plate, and can be approximated by increasing the deflection of the plate with no change in the buckling mode until ultimate strength is achieved.

(2) In a rectangular plate subjected to transvers compressive load, initial buckling occurs in the sine wave mode of 1-half-wave × 1-half-wave and then transitions to the roof-shape mode on the development of buckling deflection.

(3) The timing of the above-mentioned buckling mode transition differs depending on the thickness and aspect ratio of the plate. In thin plates, collapse occurs after the transition to the roof-shape mode, whereas in thick plates, collapse occurs in a state close to the sine wave mode of 1-half-wave × 1-half-wave. Furthermore, the timing of the change to the roof-shape mode is earlier in the case of high aspect ratios.

(4) For a buckling response that the buckling mode changes in the middle of loading process, elastic large deflection analyses were carried out separately assuming the two cases of the deflection mode at the time of initial buckling and the deflection mode when deflection has been sufficiently developed. If the case with the larger deflection is adopted, the amount of deflection to be increased by changing the buckling mode can be estimated by an explicit calculation method.

(5) As two types of buckling behavior of rectangular plates under compression, this study presented collapse triggered by yielding caused by in-plane compressive load near the supporting edges of a rectangular plate, and collapse triggered by bending yielding near the centerline of a rectangular plate, which occurs in comparatively thick plates.

(6) This study also demonstrated that it is possible to estimate the ultimate strength of plates in all biaxial stress states with good accuracy, independent of the plate thickness, by two types of collapse judgment methods corresponding to the collapse behaviors mentioned in (5).

In ultimate strength evaluations of panels supported by stiffeners, the general practice is to consider the effect of the stiffness of the stiffeners on plate panels. Therefore, it is also necessary to study a method which considers the effect of stiffeners.

REFERENCES

1) Faulkner, D.:A Review of Effective Plating for Use in the Analysis of Stiffened Plating in Bending and Compression, J. of Ship Research, Vol. 19, No.1 (1975), pp.1-17.
2) Y. Ueda, W. Yasukawa, T. Yao et al.: Ultimate Strength of Square Plates Subjected to Compression (2nd Report): Comprehensive Study on Effects of Initial Imperfection, J. Soc. Naval Architects of Japan, No. 140 (1976), pp. 205-209.
3) C. Guedes Soares : Design equation for ship plate elements under uniaxial compression, Journal of Constructional Steel Research, Vol. 22, Issue 2, 1992, pp. 99-114.
4) H. Ohtsubo, Y. Yamamoto, Y.-J. Lee: Ultimate Compressive Strength of Wide Rectangular Plates, J. Soc. Naval Architects of Japan, No. 142 (1977), pp. 279-289.
5) H. Ohtsubo, J. Yoshida: Ultimate Strength of Rectangular Plates under Combination of Loads (Part 1): Biaxial Compression, J. Soc. Naval Architects of Japan, No. 156 (1984), pp. 323-329.
6) Masahiko Fujikubo, Tetsuya Yao, Mohammad Reza Khedmati, Minoru Harada and Daisuke Yanagihara : Estimation of ultimate strength of continuous stiffened panel under combined transverse thrust and lateral pressure Part 1: Continuous plate, Marine Structures 2005, pp.383-410.
7) Nippon Kaiji Kyokai: Common Structural Rules for Bulk Carriers and Oil Tankers (CSR-B&T), Vol. 1, Ch. 8, 2019
8) E.Byklum and J. Amdahl : A Simplified method for elastic large deflection analysis of plates and stiffener plate due to local buckling, Thin-Walled Structures, 2000;40(11), pp.925-953.
9) H.Egger, B.Kröplin : Yielding of Plate with Hardening and Large Deformation, Int. J. Num. Meths. in Engrg., Vol. 12 (1978), pp.739-750.

APPENDIXES

Appendix 1 Derivation of Load-Deflection Relationship

In cases where longitudinal compressive load is dominant, the Airy stress function F for a rectangular plate in which deflection is generated can be derived by substituting Eq. (1) and Eq. (2) for Eq. (3) as shown in Eq. (a1).

$$F = \frac{\left(A_l^2 - A_{l0}^2\right)E}{32}\left(\frac{a^2}{m^2b^2}cos\frac{2m\pi}{a}x + \frac{m^2b^2}{a^2}cos\frac{2\pi}{b}y\right) - \frac{\sigma_{x0}}{2}y^2 - \frac{\sigma_{y0}}{2}x^2 \quad \text{(a1)}$$

Based on the definition of the stress function, the in-plane stress generated by deflection is obtained by the following equations.

$$\sigma_x = \frac{\partial^2 F}{\partial y^2} = -\left(A_l^2 - A_{l0}^2\right)\frac{m^2\pi^2 E}{8a^2}cos\frac{2\pi}{b}y - \sigma_{x0} \quad \text{(a2)}$$

$$\sigma_y = \frac{\partial^2 F}{\partial x^2} = -\left(A_l^2 - A_{l0}^2\right)\frac{\pi^2 E}{8b^2}cos\frac{2m\pi}{a}x - \sigma_{y0} \quad \text{(a3)}$$

Further, the amount of compressive displacement of a rectangular plate in which deflection is generated under in-plane load can be expressed as follows.

$$u = \frac{1}{b}\int_0^a\int_0^b \epsilon_{xm} - \frac{1}{2}\left(\frac{\partial w}{\partial x}\right)^2 dxdy \quad \text{(a4)}$$

$$v = \frac{1}{a}\int_0^a\int_0^b \epsilon_{ym} - \frac{1}{2}\left(\frac{\partial w}{\partial y}\right)^2 dxdy \quad \text{(a5)}$$

From Eqs. (a4) and (a5), the displacement when small deflection is generated is as shown by the equations below.

$$\delta u = -\delta A_l \cdot A_l \frac{m^2\pi^2}{4a} \tag{a6}$$

$$\delta v = -\delta A_l \cdot A_l \frac{\pi^2}{4b} \tag{a7}$$

Because the amounts of work of external force and internal force generated by small deflection δA_l can be calculated by Eq. (a8) and Eq. (a9), respectively, Eq. (a10) and Eq. (a11) can be derived by substituting the respective stress components and strain components derived from the Airy stress function, etc.

$$\delta W_e = (-\sigma_{x0})bt \cdot \delta u + (-\sigma_{y0})at \cdot \delta v \tag{a8}$$

$$\delta W_i = \int_V (\sigma_{xm} + \sigma_{xb})(\delta\epsilon_{xm} + \delta\epsilon_{xb}) + (\sigma_{ym} + \sigma_{yb})(\delta\epsilon_{ym} + \delta\epsilon_{yb})dV \tag{a9}$$

$$\delta W_e = \delta A_l \cdot A_l \frac{\pi^2}{4}\left(\sigma_{x0}\frac{m^2 b}{a} + \sigma_{y0}\frac{a}{b}\right)t \tag{a10}$$

$$\delta W_i = \delta A_l \left[(A_l^2 - A_{l0}^2)A_l \frac{\pi^4 E}{64}\left(\frac{m^4 b}{a^3} + \frac{a}{b^3}\right)t + (A_l - A_{l0})\frac{\pi^4 E}{48(1-\nu^2)}\left(\frac{m^4 b}{a^3} + \frac{a}{b^3} + \frac{2m^2}{ab}\right)t^3\right] \tag{a11}$$

According to the principle of virtual work, the work of external force and internal force are identical, as shown in Eq. (a12). Therefore, Eq. (4) can be derived.

$$\delta W_e = \delta W_i \tag{a12}$$

Next, the load-deflection relational expression is also obtained by the development of the same formula for cases where transverse compressive load is dominant. The Airy stress function F can be derived as follows by substituting Eq. (5) for Eq. (3).

$$F_I = \frac{(A_t^2 - A_{t0}^2)E}{32}\left(\frac{c^2}{b^2}\cos\frac{2\pi x}{c} + \frac{b^2}{c^2}\cos\frac{2\pi y}{b}\right) - \frac{\sigma_{x0}}{2}y^2 - \frac{\sigma_{y0}}{2}x^2 \tag{a13}$$

$$F_{II} = -\frac{\sigma_{x0}}{2}y^2 - \frac{\sigma_{y0}}{2}x^2 \tag{a14}$$

Using these equations, the in-plane stress generated by deflection is obtained as shown in the following equations.

$$\sigma_{xI} = \frac{\partial^2 F}{\partial y^2} = -(A_t^2 - A_{t0}^2)\frac{\pi^2 E}{8c^2}\cos\frac{2\pi y}{b} - \sigma_{x0} \tag{a15}$$

$$\sigma_{yI} = \frac{\partial^2 F}{\partial x^2} = -(A_t^2 - A_{t0}^2)\frac{\pi^2 E}{8b^2}\left(\cos\frac{2\pi x}{c} + \frac{a-c}{a}\right) - \sigma_{y0} \tag{a16}$$

$$\sigma_{xII} = -\sigma_{x0} \tag{a17}$$

$$\sigma_{yII} = -(A_t^2 - A_{t0}^2)\frac{\pi^2 E}{8b^2}\frac{c}{a} - \sigma_{y0} \tag{a18}$$

The displacement when small deflection is generated is expressed by the equations shown below.

$$\delta u = -\delta A_t \cdot A_t \frac{\pi^2}{4c} \tag{a19}$$

$$\delta v = -\delta A_t \cdot A_t \frac{\pi^2}{4} \frac{2a-c}{ab} \tag{a20}$$

The amounts of work of external force and internal force when small deflection δA_t is generated can be derived from Eq. (a21) and Eq. (a22), respectively.

$$\delta W_e = \delta A_t \cdot A_t \frac{\pi^2}{4} \left(\sigma_{x0} \frac{b}{c} + \sigma_{y0} \frac{2a-c}{b} \right) t \tag{a21}$$

$$\begin{aligned} \delta W_i = \delta A_t \Bigg[& (A_t^2 - A_{t0}^2) A_t \frac{\pi^4 E}{64} \left(\frac{b}{c^3} + \frac{3c}{b^3} - \frac{2c^2}{ab^3} \right) t \\ & + (A_t - A_{t0}) \frac{\pi^4 E}{48(1-\nu^2)} \left(\frac{2a}{b^3} + \frac{b}{c^3} - \frac{c}{b^3} + \frac{2}{bc} \right) t^3 \Bigg] \end{aligned} \tag{a22}$$

Appendix 2 Calculation of Deflection by Cardano's Formula

In order to apply Cardano's formula to the cubic equation for deflection A_l shown in Eq. (4), the coefficients of the cubic equation are arranged as shown in Eq. (b1).

$$A^3 + 3pA + 2q = 0 \tag{b1}$$

$$p = -\frac{1}{3\alpha_2} (\alpha_1 + \alpha_2 A_0^2 - \alpha_3) \tag{b2}$$

$$q = -\frac{\alpha_3}{2\alpha_2} A_0 \tag{b3}$$

This equation as a maximum of 3 solutions, including real solutions and imaginary solutions. Among those solutions, however, the solution which is needed in this evaluation method is the largest real solution. Only that value can be obtained by using the following equations.

In case $q^2 + p^3 \geq 0$,

$$A = \sqrt[3]{-q + \sqrt{q^2 + p^3}} + \sqrt[3]{-q - \sqrt{q^2 + p^3}} \tag{b4}$$

In case $q^2 + p^3 < 0$,

$$A = 2 \cos \frac{\theta}{3} \sqrt{-p} \tag{b5}$$

$$\theta = \operatorname{arccot} \frac{-q}{\sqrt{-q^2 - p^3}} \tag{b6}$$

Trends in Utilization and Transportation Technologies for Hydrogen and Other Clean Fuels

Sadao AKAHOSHI*

1. INTRODUCTION

Today, the world depends on fossil fuels for more than 80 % of its energy supply (Fig. 1), and abnormal weather which appears to originate from the global warming of recent years has become a frequent occurrence. Against this backdrop, reduction of greenhouse gas (GHG) emissions has become an urgent challenge.

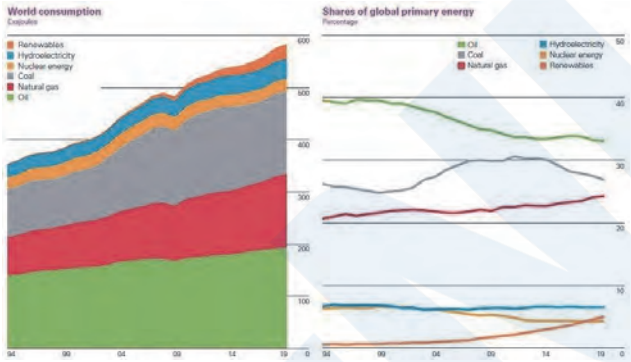

Figure 1 World energy consumption (by resources)
Source: bp – Statistical Review of World Energy

Operation of the Paris Agreement, which is the international framework for global warming measures that replaced the Kyoto Protocol, began this year. Although the Paris Agreement set a target of limiting temperature rise to less than 1.5 °C in comparison with the pre-Industrial Revolution level (Fig. 2), it will be necessary to reduce the carbon dioxide (CO_2) emissions of the developed countries to zero by 2050 in order to realize this target.

However, according to an announcement by the Secretary-General on September 9, there is an increasing probability that temperature rise will exceed 1.5 °C as early as within the next 5 years. Around the same time, news reports described large-scale forest fires in the United States. These developments, together with the withdrawal of the United States from the Paris Agreement and return to a policy of dependence on fossil fuels under President Trump stoked fears of a worsening of the condition of climate change.

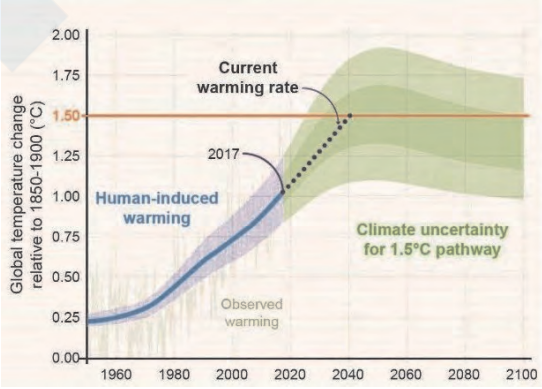

Figure 2 Transition of average global temperature and predictions of future temperature change
Source: IPCC – Global Warming of 1.5 °C

* Renewables and Environment Department, ClassNK

On the other hand, the EU has set a target of achieving substantially zero emissions of GHG by 2050. The EU is not only putting effort into a shift from power generation by combustion of fossil fuels to generation utilizing renewable energy but has also established a policy of broadly limiting GHG emissions in fields other than power generation with the aim of achieving this long-term target. A key technology for achieving this goal is utilization of hydrogen energy.

Japan has also set a CO_2 reduction target of ▲26.0 % in comparison with FY 2013, to be realized by FY 2030 (▲25.4 % in comparison with FY 2005) and achieving an 80 % reduction in the developed countries as a whole by 2050. In order to achieve an 80 % reduction in GHG emissions in the future, drastic efforts will be necessary in all fields of society, including zero emissions of CO_2 from electric power plants as far as possible, zero emissions from transportation equipment and significant reductions in CO_2 emissions from factories and homes. Since hydrogen and other clean fuels which do not discharge CO_2 are positioned as key technologies for achieving this goal, study of the production, transportation and use of clean energy is underway. At present, however, the production cost of clean fuels is high in comparison with fossil fuels, and how to curtail total CO_2 emissions, including the clean fuel production and transportation processes, has become an issue.

This paper presents the outlook for utilization of hydrogen and other clean fuels, which are expected to be used in the future, and also introduces the energy carriers (liquefied hydrogen, ammonia, organic hydrides, methanol, methane) that will be used in large volume transportation and storage.

2. JAPAN'S BASIC STRATEGY FOR HYDROGEN UTILIZATION

Unlike coal, natural gas and other fossil fuels, hydrogen forms water when burned, and does not generate carbon dioxide.

Considering this feature, hydrogen is expected to play a key role in decarbonization.

At present, the price of hydrogen is still high, and its distribution volume is small. However, Japan's national targets [1] aim firstly for developing supply chains for 300 000 tons/year by 2030, secondly aim for increasing to 10 million tons/year in the future and making it possible to supply hydrogen at a price about 20 % above the cost of natural gas.

The immediate main applications of hydrogen will be mixed combustion with conventional fossil fuels or mono-fuel combustion of hydrogen in electric power plants, fuel cells for vehicles, fuel cells for household use (Ene-Farm), *etc*.

It may also be noted that various production processes exist under the general name of "hydrogen."

Japan's hydrogen strategy begun from the perspective of diversifying the country's primary energy supply structure, which has been largely depended on fossils fuels and also heavily skewed toward imports from overseas sources. From this perspective, the focus of the Basic Strategy was unused fossil fuel resources, which exist in abundance in other countries. Concretely, these efforts include a joint demonstration project being carried out by Japan and Australia for a liquefied hydrogen supply chain, which involves production of hydrogen from brown coal (lignite) and marine transportation in the form of liquefied hydrogen, and also a joint project of Japan and Brunei for an organic hydride supply chain, including conversion of hydrogen to organic hydrides, transportation and dehydrogenation before use (Fig. 3). These projects are considered to have an extremely important meaning in terms of securing Japan's interests by acquiring stable overseas energy resources at a comparatively low cost.

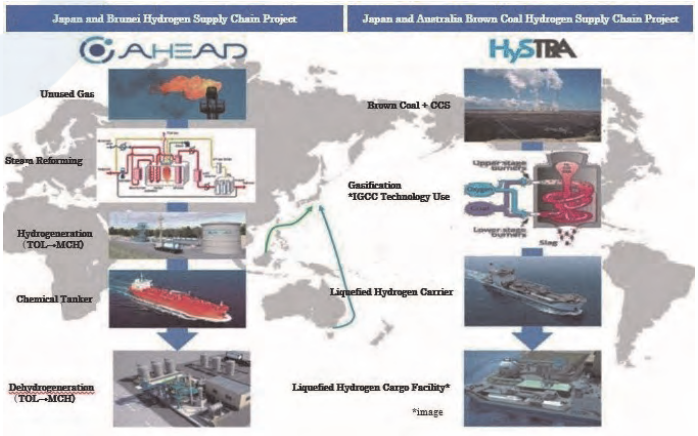

Figure 3　Hydrogenation projects utilizing unused resources from overseas

However, simply using hydrogen produced by reforming fossil fuels is inadequate from the viewpoint of CO_2-free clean energy. Therefore, it is necessary to combine hydrogen production with technologies for separation, recovery and storage of CO_2 generated in the hydrogen production process, particularly carbon dioxide capture and storage (CCS) or enhanced oil recovery (EOR). EOR is a technique for increasing the recovery rate of crude oil from oil wells which no longer produce naturally and has been widely adopted as a commercial technology in North America, but this technique ultimately leads to new fossil fuel extraction.

As in the techniques described above, fossil fuel-derived hydrogen which suppresses CO_2 emissions on a life cycle base by CCS, *etc.*, is generally called "blue hydrogen." In the standard for low-carbon hydrogen created in Europe, if more than half of the CO_2 generated in the processes from production of hydrogen by steam reforming of natural gas (including excavation, transportation and processing) to use of the hydrogen can be treated by CCS, *etc.*, the hydrogen is defined as blue hydrogen ($5.8tonCO_{2e}/tonH_2$ or less). Hydrogen (green hydrogen) produced by electrolysis of water using CO_2-free electric power produced by renewable energy is also considered low-carbon hydrogen, if the electricity for production is $58MWh/tonH_2$ or less.

The policy on the use of hydrogen in Japan [1] is based on the Basic Hydrogen Strategy (Fig. 4) established in December 2017.

Under the Basic Strategy, Japan plans to create a hydrogen society through a step-by-step process in the following three phases.

① Phase 1: Dramatic expansion of hydrogen use (from present)
By dramatically expanding the use of fixed fuel cells and fuel cell vehicles (FCVs), which it is now starting to realize, Japan will capture the global market for hydrogen and fuel cells, in which it leads the world.

② Phase 2: Full-fledged introduction of hydrogen power generation and establishment of a large-scale hydrogen supply system (by the second half of the 2020s)

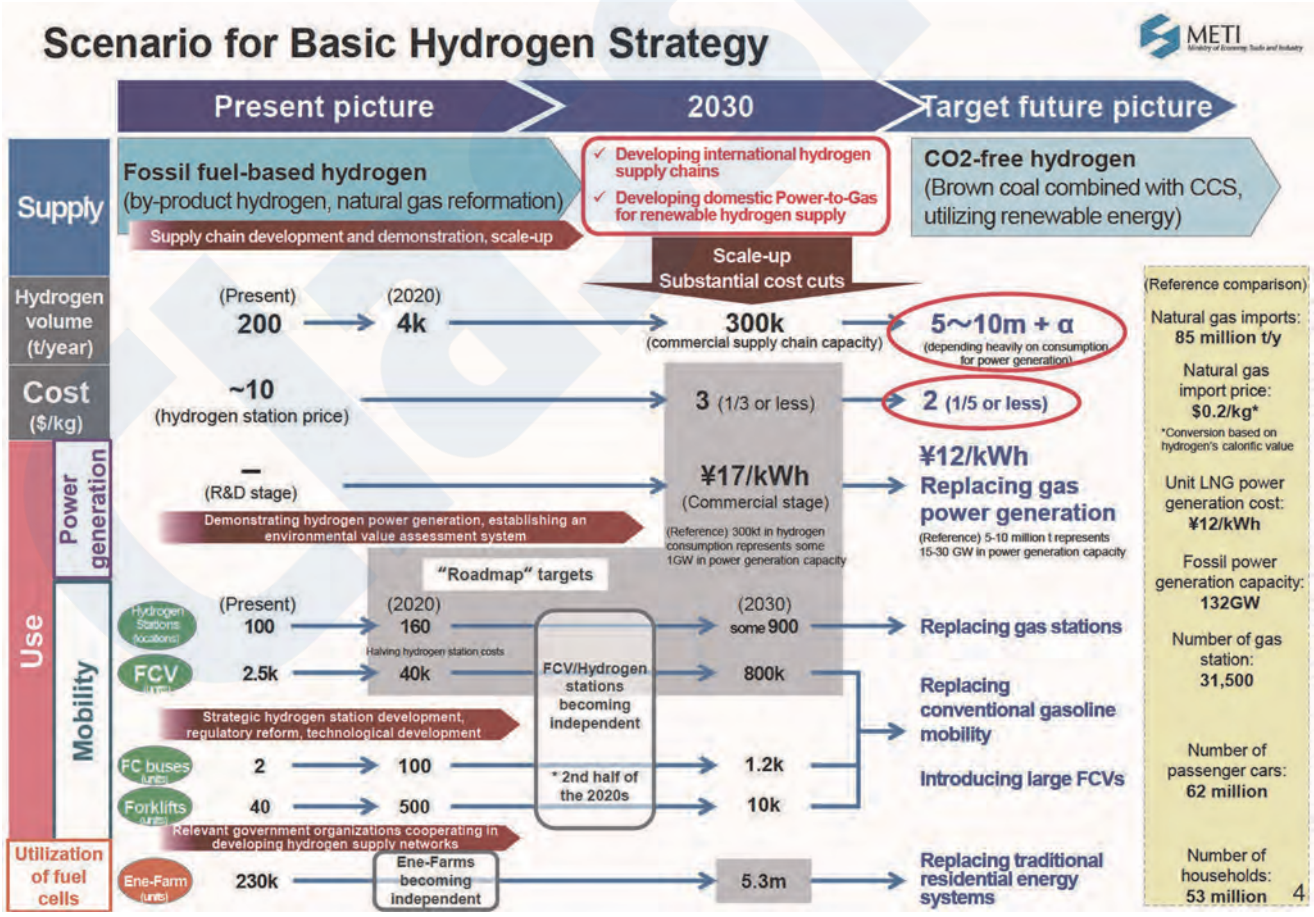

Figure 4　Scenario for Basic Hydrogen Strategy
Source: Basic Hydrogen Strategy (Dec. 2017)

While increasing hydrogen demand further, Japan will increase the scope of current hydrogen sources to include unused energy sources and establish a new secondary energy structure which adds hydrogen to the conventional electricity and heat.

③ Phase 3: Establishment of a CO_2-free hydrogen supply system on a total basis (by around 2040)
Japan will combine hydrogen production with CCS or use hydrogen from renewable energy to establish a totally CO_2-free hydrogen supply system.

3. ISSUES FOR POPULARIZATION OF HYDROGEN AND OTHER CLEAN ENERGY

The issues for popularization of hydrogen and hydrogen-derived energy are described in detail in the Basic Hydrogen Strategy mentioned above and the Strategic Road Map [2] for Hydrogen and Fuel Cells, which was drawn up subsequently in March 2019. The following describes the issues for popularization based on these two documents.

3.1 Hydrogen Cost

The current cost of hydrogen is ¥100/Nm^3, which is equivalent to approximately ¥1,100/kg. The running performance of fuel cell vehicles (FCVs) is generally considered to be about the same as vehicles using high octane gasoline. This effect is achieved in automobiles due to the high efficiency of FCVs, but if compared on a calorific value basis, the two are different. In recent years, the price of LNG imported by Japan has been on the level of $7-15/MMBtu, and the converted price of hydrogen on a calorific value basis is ¥9-20/Nm^3.

The strategy laid out by the government sets targets of reducing the price of hydrogen (plant delivery cost basis) to ¥30/Nm^3 by around 2030 and to ¥20/Nm^3 in the future.

3.2 Efficient Transportation Methods

As described previously, it is possible to construct international hydrogen supply chains by producing hydrogen from low-cost and unused fossil fuel resources, which exist in abundance in overseas and combining hydrogen production with CCS.

In this case, , it is important to construct efficient supply chains as well as reducing the cost of hydrogen production in order to reduce the supply cost of hydrogen energy to a level comparable with that of conventional energy. To achieve this, in addition to transportation in liquefied form, energy carriers (note: methods in which hydrogen is converted to other substances for easy transportation and storage) for efficient transportation of hydrogen energyare under study [3]. (Fig 5.)

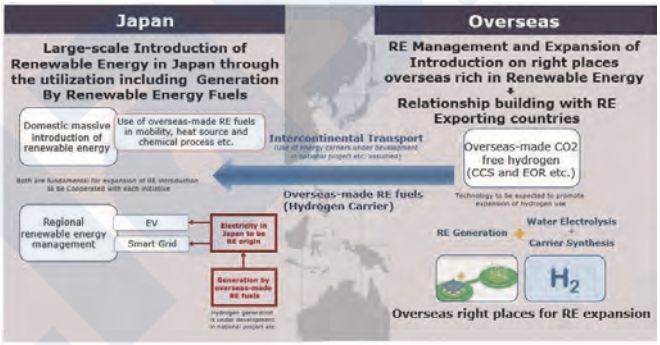

Figure 5 Large volume introduction of renewable energy-derived fuels from overseas

3.2.1 Liquefied Hydrogen

In order to liquefy hydrogen, hydrogen must be cooled to -253 °C. The volume of liquefied hydrogen is 1/800 that of hydrogen at normal pressure. Liquefied hydrogen will be transported in special dedicated heat-proofed ships. Since the cost of liquefaction accounts for approximately 30 % of the total cost of hydrogen with the existing hydrogen liquefaction technology, liquefied transportation is assumed to be a suitable method for large volume, long distance transportation. In case large volumes of hydrogen are to be stored at liquefied hydrogen offloading terminals, it is only possible to manufacture tanks with a scale of several 1 000 m^3 at present. However, if tanks of the same scale as LNG tanks can be manufactured in the future, this will contribute to reducing the cost of hydrogen.

Although the EU has made hydrogen utilization a key component of environmental measures, liquefaction is not necessary because a well-developed gas pipeline network already exists in Europe.

For small and medium size lots, the general practice is to compress hydrogen at a high pressure of 19.6 MPa (approximately 200 atm) or higher and transport the compressed gas by tank lorry or trailer containers equipped with hydrogen tanks. Because FCVs use high pressure hydrogen with a pressure of 700 atm, intermediate-stage compression for transport is not wasted (Table 1).

3.2.2 Ammonia

Like hydrogen, there are also two types of ammonia, blue ammonia and green ammonia.

Blue ammonia is produced by reforming air and natural gas. The CO_2 generated in this process is separated and recovered, and some is used as a feedstock for urea, while the remainder is stored underground or under the sea bottom by CCS or EOR. This method has already reached a large scale (2 000 to 3 000 t/d), achieving high efficiency. Approximately 70 % of the CO_2 generated in ammonia production is already separated and used as pure CO_2.

In the case of ammonia, the fact that international supply chains have already been established is a large merit. Current world ammonia production is approximately 180 million tons/year, of which 80 % is used as a feedstock for fertilizer, and about 16-19 million tons/year of ammonia are traded by seaborne trade. Large lots of 15 000 tons and larger are currently carried by refrigerated ships (LPG/LAG ships), while small ships are used for medium-sized lots of 200 to 1 000 tons, which are carried at a medium pressure of approximately 3 to 4 kg/cm^2 (3-4 atm) and a temperature of 0 °C. Small lots of around 10 tons are transported by tank lorry as high pressure products with a pressure of 18 kg/cm^2 or less. Since ammonia is already produced industrially from fossil resources at a certain scale, and transportation methods have also been established, there are no large limitations on the supply volume of blue ammonia if provided CCS or EOR is possible (Table 1).

It is also possible to utilize ammonia directly as a fuel without conversion to hydrogen. Based on this, there is a view that ammonia is the clean fuel which is closest to commercialization at the present point in time. In the 1940s, research and demonstration experiments using ammonia as a fuel were conducted in both Europe and the United States, but due to issues of efficiency, *etc*., the technology of the time failed to reach practical application. However, research on a high efficiency, low NOx ammonia combustion technology and so forth was carried out in Japan under the Cross-ministerial Strategic Innovation Promotion Program (SIP), "Energy Carriers" project of the national government for a 5-year period beginning in 2014. The Green Ammonia Consortium (GAC), which was established to commercialize the results of that research and development work, became independent as a General Incorporated Association in April 2019. Focusing on the future potential of ammonia, the GAC is developing efforts to popularize the use of ammonia with the participation of major shipping companies, including Nippon Yusen Kaisha (NYK Line), Mitsui O.S.K. Lines and others.

The current import price of ammonia is about ¥30,000 to ¥50,000 per ton and ammonia contains 17.8 wt% of hydrogen, if ammonia is considered as a hydrogen energy carrier, the cost of hydrogen is ¥170 to ¥450/kg-H_2. If ammonia is synthesized using CO_2-free hydrogen produced with renewable energy-derived electric power in Japan, the cost is extremely high in comparison with the current price of ammonia. Therefore, Japan is studying the concept of producing hydrogen by water electrolysis using low cost renewable energy-derived electric power and large volume importing by ship with overseas resources of solar, wind power and vast land areas. (Table 1).

Table 1　Comparison of hydrogen energy carriers

	Liquefied H_2	Ammonia (NH_3)	Methylcyclohexane (MCH)
1. Production methods	① Steam reforming of natural gas, brown coal or other fossil fuels + CCS or EOR (enhanced oil recovery) ② Formation by decomposition of water using renewable energy-derived electricity ③ R&D on a thermochemical method using solar thermal energy is now in progress.	① Produced by reforming natural gas and air. Most CO_2 generated in this process is separated, recovered and used + CCS or EOR. ② Ammonia is synthesized from hydrogen produced by water electrolysis using renewable energy-derived electricity and nitrogen produced by air separation as raw materials.	① Produced by bonding hydrogen to an aromatic compound such as toluene, *etc*. Hydrogen is extracted by a dehydrogenation reaction at the user's facility, and toluene is reused repeatedly.
2. Transportation efficiency	① In large volume transportation to Japan from overseas, hydrogen is liquefied (1/800 of volume at normal pressure) at -253 °C and transported by dedicated ships. A NEDO demonstration project is in progress. In Europe, etc., the main method is pipeline transportation. ② For small and medium lots, hydrogen is compressed to a high pressure of 19.6 MPa (approx. 200 atm) and transported by tank lorry, trailer containers equipped with liquefied hydrogen tanks or gas cylinder bundles.	① Ammonia liquefies at -33.3 °C under normal pressure, and at 20 °C under pressurization of 0.86 MPa. ② At present, reefers (LPG/LAG ships) are used to carry large lots of 15 000 tons or more. ③ Medium lots of 200 to 1 000 tons are transported by small ship as medium-pressure products (approx. 3-4 kg/cm^2, 3-4 atm) at 0 °C. ④ Small lots of around 10 tons are transported by tank lorry as high pressure products (18 kg/cm^2 or less)	① Easy to transport and store, as MCH is a liquid at normal temperature/normal pressure. (Since the physical property is like solvent, existing gasoline distribution infrastructure can be used.)
Volumetric hydrogen density	7.1 kg-H_2/100 L (-273 °C) : ○	10.7 kg-H2/100 L (1 MPa, 25 °C) : ◎ 12.1 kg-H2/100 L (0.1 MPa, -33.3 °C) : ◎	4.73 kg-H_2/100 L : Δ
Mass hydrogen density	100 wt% : ◎	17.8 wt% : ○ (cf. hydrogen storage alloy < 5 wt%)	6.16 wt% : Δ
3. Use methods	① Fuel cell ② Direct combustion (mono-fuel combustion, mixed fuel combustion)	① Used after decomposition to hydrogen ② Ammonia fuel cell ③ Direct combustion (mono-fuel combustion, mixed fuel combustion)	① Used after decomposition of hydrogen.

3.2.3　Methylcyclohexane (MCH)

Methylcyclohexane (MCH) is a substance in which hydrogen is bonded with toluene (Fig. 6). Because MCH is a liquid at normal temperature/normal pressure, it has the merits that handling in transportation and storage is easier than with ammonia, and the existing gasoline distribution infrastructure can be used.

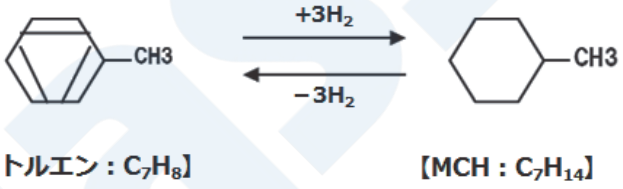

Figure 6　Production of MCH

In the MCH method, hydrogen is transported in the form of MCH, and is then extracted by a dehydrogenation reaction at the user's facility (organic hydride method). The toluene can be recycled and reused repeatedly (Table 1).

After Chiyoda Corporation set a target for industrialization of a catalyst for the dehydrogenation reaction, MCH also attracted considerable attention as an energy carrier. This technology was demonstrated in the above-mentioned supply chain project in which hydrogen energy was imported from Brunei.

As a drawback, the hydrogenation and dehydrogenation processes consume the equivalent of about 30 % of the energy of hydrogen. To solve this problem, a method for direct production of MCH from water and toluene using renewable energy-derived electric power is now under development. If realized, this method will reduce the efficiency loss of MCH.

3.2.4　Methane and Methanol

Although the positioning of the technology called methanation is somewhat different from the three above-mentioned methods, research on this technology is also underway. In methanation, methane and methanol are produced from the CO_2 discharged from electric power plants and other facilities. However, fossil fuel-derived blue hydrogen is not used in this process, as it would be environmentally meaningless to produce methane, *etc*. from hydrogen, if that hydrogen is produced from natural gas (methane, *etc*.) (Fig. 7).

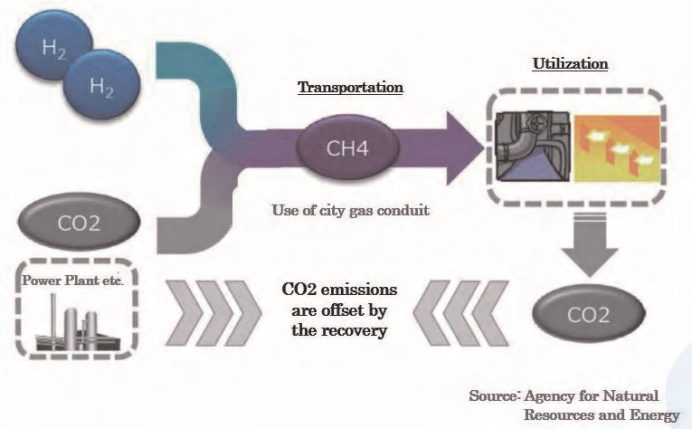

Figure 7　Schematic diagram of methanation process

It can be said the methanation is a technology that reuses CO_2, since the amount of CO_2 recovered when methane and methanol are synthesized, and the amount of CO_2 generated when the recovered methane and methanol are burned are mutually offsetting. In other words, methanation can be considered carbon neutral. This is the same concept as when renewable biomass fuels such as waste wood are used.

The Organization for Carbon Capture and Reuse was established, centering on Japan's National Institute of Advanced Industrial Science and Technology (AIST) and Hitachi Zosen Corporation, and is developing activities aimed at reducing the use of fossil fuels by providing alternative energy using a combination of CO_2 emitted from industry and hydrogen produced by using renewable energy.

4.　EFFORTS FOR UTILIZATION OF HYDROGEN AND OTHER CLEAN FUELS

This chapter touches on recent trends from the perspective of popularizing the use of hydrogen and other clean fuels in Japan.

4.1　Use of Ammonia in Coal-Fired Thermal Power Generation Field

The electric power sector accounts for 40 % of Japan's total CO_2 emissions (Fig. 8).

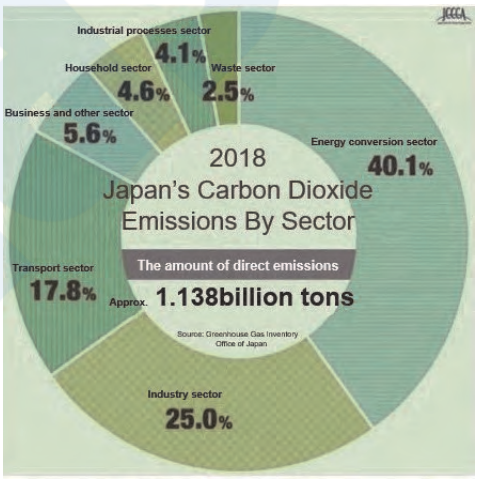

Figure 8　Shares of CO_2 emissions by sector in Japan
Source: Website of the Japan Center for Climate Change Actions (JCCCA)

In the composition of power sources in Japan, the share of fossil fuels exceeds 80 %, as the shares of power generation by natural gas, coal and petroleum are 40 %, 33 % and 9 %, respectively (Fig. 9). In comparison with combustion of natural gas, coal-fired thermal power produces a larger CO_2 emission per unit of generated power. For this reason, construction of new coal-fired plants has become increasingly difficult in recent years, including plants which use ultra-super critical (USC) coal-fired thermal power generation technology, which can reduce unit CO_2 emissions by approximately 10 % in comparison with

conventional coal-fired thermal power plants, and integrated coal gasification combined cycle (IGCC) technology, which can reduce CO_2 emissions even further.

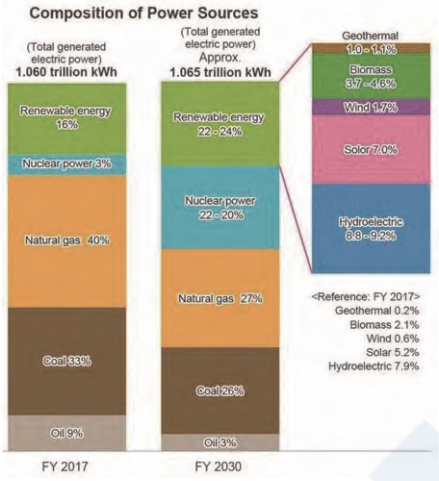

Figure 9　Power source composition in Japan (FY 2017, targets for FY 2030)
Source: Website of the Agency of Natural Resources and Energy

Nevertheless, because coal is a fossil fuel which is comparatively inexpensive and has abundant reserves, even when viewed globally, it is positioned as a key means of power generation from the viewpoint of securing a stable supply of energy in Japan. Although the target for power generation by coal in 2030 is lower than at present, it is expected to maintain a high share of 26 %[4].

Mixed combustion using ammonia in coal-fired thermal power plants is being studied. If carbon-free ammonia is used, the CO_2 emission will decrease in proportion to the amount of ammonia injection. Therefore, mixed combustion of up to 20 % ammonia using the existing equipment is under study.

As features of ammonia combustion, the following are technical issues for mixed combustion:

- The combustion velocity is slow.
- The flame temperature is low.
- NOx is generated owing to the nitrogen content in the fuel.

In addition, corrosivity and toxicity are also issues. When studying use of ammonia as a fuel, it is necessary to consider countermeasures for these various problems.

The New International Resource Strategy [5], which was adopted by the Ministry of Economy, Trade and Industry (METI) in March 2020, calls for expanded use of fuel ammonia, and states that “demonstration projects will be carried out assuming use in thermal power plants, industrial furnaces, ships, *etc*.”

The following is an excerpt from the New International Resource Strategy (March 2020, METI).

IV. Response to climate change problem

2. Directions of response

(3) Expanded use of fuel ammonia

Fuel ammonia is carbon free if techniques such as renewable energy, CO_2 EOR, CCS, afforestation, *etc*. are used. Fuel ammonia also has the advantage that a global supply chain has already been established.

During the period 2014 to 2018, basic research was carried out as a SIP project of the Cabinet Office, confirming the possibility of suppressing NOx emissions, which had been a concern, by technology development.

For reduction of CO_2 from thermal power generation, industrial furnaces, ships, *etc*., in the future, it will be necessary to promote sure technology development, including mixed combustion of fuel ammonia, which is now being promoted by the FS, with a strong awareness of the concept of understanding/importing renewable energy produced in various other countries as an energy resource like petroleum or natural gas, in the same way as hydrogen.

(Fuel ammonia demonstration projects)

- In order to construct supply chains for fuel ammonia, a feasibility study on procurement of ammonia will be carried out.
- In order to promote the use of fuel ammonia, demonstration projects will be carried out assuming mixed combustion in thermal power generation and use in industrial furnaces, ships, *etc*.

Assuming hypothetically mixed combustion using 20 % ammonia in a 1 GW coal-fired thermal power plant, the necessary amount of ammonia is 600,000 tons. According to an investigation of the figures published by the Japan Fertilizer & Ammonia Producers Association, the domestic supply of ammonia in Japan in FY 2019 was 1.1 million tons, of which 240,000 tons were imported. These numbers, the reader can understand the enormous scale of ammonia consumption in mixed combustion in a coal-fired thermal power plant. Since improving the efficiency of marine transportation will also be a key point, research and development in connection with liquefied ammonia gas carriers is being conducted by Nippon Yusen Kaisha (NYK Line) and Japan Marine United Corporation, *etc*.

4.2 Use of Hydrogen and Ammonia in Gas Turbines

Gas turbines have a variety of desirable features, including a short starting time, high output with compact equipment and low generation of NOx, and are used in a variety of applications, beginning with power generation.

With large-scale units, it is possible to achieve generating efficiency exceeding 60 % by constructing a combined generation system with a steam turbine that utilizes the high temperature exhaust gas from the gas turbine. Although the generating efficiency of small-scale gas turbines is lower, high total efficiency can be realized by supplying steam with a waste heat recovery boiler which uses the high temperature exhaust gas.

Large-scale LNG gas combined cycle systems have excellent environmental performance, as the amount of CO_2 per unit of generated output is 310 g-CO_2/kWh, or less than half of that generated by the aforementioned ultra-super critical (USC) coal-fired thermal power plants and integrated coal gasification combined cycle (IGCC) plants, which further reduces CO_2 emissions in comparison with USC.

Efforts are also being made to achieve a dramatic reduction in direct emissions accompanying power generation by mixed combustion of natural gas and hydrogen as fuels for the gas turbine or replacing 100 % of the current natural gas fuel with hydrogen. The fact that the receiving standards for hydrogen to be burned in gas turbines are looser than those required for fuel cells, *etc*. is also an advantage in terms of reducing the hydrogen cost.

Mixed combustion tests with 30 % hydrogen have already been carried out with large-scale, high efficiency turbines, and development of a hydrogen mono-fuel combustion technology is underway. Moreover, use of the waste heat of the turbine to decompose ammonia to hydrogen and nitrogen, and use of the hydrogen in a hydrogen mixed combustion turbine, is also being studied.

Among efforts to take even greater advantage of the outstanding features of gas turbines, a project in which a natural gas-fired turbine power generation system manufactured by Mitsubishi Heavy Industries, Ltd. will be converted to a hydrogen-fired system is in progress in Europe, targeting the start of commercial operation in 2025. The company has also received an order for a 840 MW hydrogen mixed combustion turbine for an overseas project, and plans to convert that turbine to 100 % hydrogen

combustion in the future. In the United States, although the words and actions of President Trump have attracted attention, efforts to reach zero CO_2 emissions by 2050 are also in progress.

5. RENEWABLE ENERGY-DERIVED FUELS

If we consider the global warming problem and resource problem that our descendants will face, the following are thought to be necessary.

- As much as possible, cease using fossil fuels for power generation, and produce and use hydrogen (or ammonia) fuels by using renewable energy (so-called power-to-gas, P2G).
- As much as possible, stop destroying forests and stop burning biomass.

Although the latter can also be considered an international political issue, at present, the former involves various technical issues, as follows:

- Reduction of the cost of renewable energy-derived electricity (development of large-scale renewable energy)
- Improvement of water electrolysis efficiency
- Response to fluctuations in the output of renewable energy power sources
- Establishment of efficient energy carriers for importing energy from overseas

The national government has constructed a facility called the Fukushima Hydrogen Energy Research Field (FH2R) in the town of Namie, Fukushima Prefecture, and is now conducting a P2G demonstration test.

The FH2R facility is equipped with 10 MW solar power generation equipment, water electrolysis equipment and hydrogen storage and supply equipment. The facility can provide a one-month supply of electric power for about 150 households with the hydrogen production from only one day. The hydrogen produced by FH2R is shipped by trailer or gas cylinder bundle (medium-scale transportation container with a structure containing multiple small cylinders). Power produced here can also be used in adjusting the supply-demand balance of the power system (demand response), and thus is expected to contribute to expanded use of renewable energy-derived electricity.

6. CONCLUSION

Japan is the world's 5th largest CO_2 emitting nation, after China, the United States, India and Russia. Because Japan is also the world's 3rd largest economy, the nations of the world take a strict view of Japan's statements and actions in response to environmental problems.

Japan has a low energy self-sufficiency rate, as the country's domestically produced energy is largely limited to hydro power and renewables, and a return to dependence on nuclear power may be difficult for reasons of safety and the problem of public acceptance. Thus, efforts to popularize the use of low carbon energy, like efforts to secure financial resources for pensions and medical costs accompanying of the aging of society, are a top priority issue for Japan. Those of us living today must take on the responsibility of meeting this challenge for the sake of the generations to come.

REFERENCES

1) Ministerial Council on Renewable Energy, Hydrogen and Related Issues: Basic Hydrogen Strategy (December 26, 2017)
2) Hydrogen and Fuel Cell Strategies Council: The Strategic Road Map for Hydrogen and Fuel Cells (March 12, 2019)
3) Cabinet Office, Japan: Final Report on Cross-ministerial Strategic Innovation Promotion Program (SIP), "Energy Carriers"
4) Ministry of Economy, Trade and Industry (METI): Long-Term Energy Supply and Demand Outlook (July 2015)
5) METI: New International Resource Strategy (March 2020)

Recent Topics at IMO

— Outline of discussion at IMO Committees —

External Affairs Department

1. INTRODUCTION

This article introduces recent topics discussed at IMO (International Maritime Organization).

At the previous issue, a summary of the decisions taken at 74th Marine Environment Protection Committee (MEPC 74) and 101st Maritime Safety Committee (MSC 101) held in 2019 was provided. In 2020, it was scheduled to hold MEPC 75 in April and MSC 102 in May, however due to the spread of COVID-19, these meetings have been postponed. At the time of writing this article, it was announced by IMO Secretariat that MEPC 75 and MSC 102 will be held in November 2020.

In this regard, this article provides topics, which are expected to be discussed at MEPC 75 and MSC 102.

2. TOPICS TO BE DISCUSSED AT MEPC 75

2.1 Greenhouse Gases (GHG) Emission Reduction Measures

Measures to reduce GHG emissions from international shipping have been deliberated at IMO, and so far, the Energy Efficiency Design Index (EEDI), the Ship Energy Efficiency Management Plan (SEEMP) and the Data Collection System for fuel oil consumption of ships (DCS) were introduced. Further, at MEPC 72 held in 2018, Initial IMO Strategy on reduction of GHG emissions from ships, which includes emission reduction target and candidate measures to reduce GHG emissions, was adopted.

2.1.1 Review of Technological Developments for EEDI

Regulation 21.6 of MARPOL Annex VI sets out that a review of the status of technological developments which may contribute to the improvement of EEDI should be conducted. It also requires, if proved necessary, to amend the subsequent requirements, i.e. “when to start the each phase” and “the reduction rate”.

1) EEDI phase 3 requirements

At MEPC 74, draft amendments to MARPOL Annex VI to strengthen the EEDI phase 3 requirements were approved. MEPC 75 is expected to adopt the amendments to MARPOL Annex VI (refer to item 2.6(1))

2) EEDI phase 4 requirements

MEPC 74 established a correspondence group (CG), coordinated by Japan, to consider possible introduction of phase 4. MEPC 75 will discuss an interim report of the CG. The interim report indicates that the CG collated and analysed information on new technologies and alternative fuels for improvement of energy efficiency, and considered how EEDI phase 4 can contribute to the 2050 target of the Initial Strategy on reduction of GHG emissions from ships. The CG will continue its discussion and submit the final report to MEPC 76.

2.1.2 Requirements of Minimum Propulsion Power and EEDI

At MEPC 65, “Guidelines for determining minimum propulsion power to maintain the maneuverability of ships in adverse conditions” were developed in order to avoid construction of extremely under-powered ships. At MEPC 71, it was agreed to extend the application period of the Guidelines towards phase 2 of EEDI regulation. Meanwhile, consideration on strengthen of the phase 3 requirements continued. Under these circumstances, concerns were raised that the requirements of minimum propulsion power in the guidelines might become a barrier for meeting the phase 3 requirements.

At MEPC 74, to address the conflict between EEDI and minimum propulsion power requirements, a proposal to introduce a concept of shaft/engine power limitation was considered, and generally accepted. To improve the concept and for further discussion, it was agreed to keep consideration at future session. It was also agreed to proceed with the revision work for requirements of minimum propulsion power in the Guidelines.

MEPC 75 will consider the concept of shaft/engine power limitation, and the revision of the Guidelines.

2.1.3 Short-term Measures for Reduction of GHG

Initial IMO Strategy on reduction of GHG emissions from ships, adopted at MEPC 72, specifies short term target by 2030 and mid/long term target by 2050. While short term measures for new ship can be addressed by strengthening the EEDI requirements, short term measures for existing ships has been an urgent issue at MEPC.

At intersessional meeting held in November 2019, various proposals for the short term measures for existing ships were submitted, and it was agreed to divide them into two approaches:

1) Technical approach

Energy Efficiency Existing Ship Index (EEXI)

2) Operational approach

Annual Efficiency Ratio (AER), Carbon Intensity Indicator (CII), strengthening the SEEMP etc.

MEPC 75 is expected to consider the technical approach for the EEXI in detail. The EEXI is a similar indicator as EEDI and applied to existing ships as follows:

- Attained EEXI for each existing ship should be calculated using similar formula as EEDI
- Required EEXI for each existing ship should be calculated using EEDI reference lines for each category of ships by multiplying reduction factor
- If the attained EEXI value cannot satisfies the required EEXI, the ship should implement a measurement, such as shaft/engine power limitation etc.

MEPC 75 will also consider the operational approach. The proposals under the operational approach are still concept phase, and it is expected to consider the proposals further at MEPC 76.

2.1.4 Mid/Long-term Measures for Reduction of GHG

In order to achieve mid/long term target specified in the Initial IMO Strategy, it is necessary to establish mid/long term measures for reduction of GHG emission from ships by stimulating the de-carbonization of shipping.

MEPC 75 will consider proposals to establish “International Maritime Research and Development Board (IMRB)” and “International Maritime Research Fund (IMRF)” to provide the necessary structure, direction and funding for successful development of low-carbon and zero-carbon technologies. MEPC 75 will also consider market-based measures (MBMs) to incentivize GHG emission reduction from shipping.

2.1.5 IMO GHG Study

At MEPC 74, it was agreed to update the “Third IMO GHG Study 2014”, which estimates the amount of CO_2 emissions from international shipping, and then, the update work has been carried out.

MEPC 75 will consider a draft “Forth IMO GHG Study 2020” with a view to approval. According to the draft Study, GHG emissions from shipping as of 2018 are estimated to be 1,076 million tons, accounting for 2.89% of global GHG emissions. Further, the draft Study estimates that GHG emissions from shipping as of 2050 will be among 90% to 130% of 2008 emissions if no further countermeasures to reduce GHG emissions will be taken.

2.2 Air Pollution

2.2.1 Failure of Exhaust Gas Cleaning System (EGCS)

At MEPC 74, “Guidance on indication of ongoing compliance in the case of the failure of a single monitoring instrument, and recommended actions to take if the EGCS fails to meet the provisions of the guidelines (MEPC.1/Circ.883)” was adopted. The Guidance specifies that EGCS malfunction that cannot be rectified within one hour should be regarded as an accidental breakdown, and actions should be taken as follows:

- changeover to compliant fuel oil
- notify the accident to flag and port States
- If the ship does not have compliant fuel oil, a proposed course of action, such as bunkering compliant fuel oil or carrying out repair works, should be communicated to flag and port States.

MEPC 75 will consider a proposal to allow the immediate use of non-compliant fuel oil after reporting to the flag and port State, if the ship does not have compliant fuel oil on an EGCS failure.

2.2.2 Bunker Delivery Note (BDN)

MARPOL Annex VI requires that each ship should keep a bunker delivery note issued by the supplier for a period of three years after the fuel oil has been delivered on board. Information to be included in the bunker delivery note is specified in appendix V of MARPOL Annex VI.

MEPC 75 is expected to consider a proposal to include flashpoint as mandatory information to be indicated in the bunker delivery note.

2.3 Ballast Water Management

2.3.1 Commissioning of Ballast Water Management Systems (BWMS)

At MEPC 74, draft amendments to BWM Convention to specify the requirements to conduct commissioning testing, sampling and analysis were approved.

MEPC 75 will adopt the amendments to BWM Convention (refer to item 2.6(4)). MEPC 75 will also adopt amendments to "Guidance for the commissioning testing of ballast water management systems (BWM.2/Circ.70)". The revised Guidance specifies the following items:

- The purpose of commissioning testing, sampling and analysis are to validate the installation of BWMS properly.
- Local ambient water should be used for the commissioning testing.
- Representative samples should be analysed for the two size classes of organisms, namely ≥ 50 μm, and ≥ 10 μm to < 50 μm, as specified in the D-2 standard, using indicative analysis methods. Analysis for microbes is not required.

2.3.2 Exemption to Specific Ship Types

MEPC 75 is expected to consider a proposal to exempt specific ship types from the Convention, such as multipurpose salvage ship and rescue tug boat, taking into account the challenges faced by these ship types.

2.4 Control of Harmful Anti-fouling Systems on Ships (AFS Convention)

AFS Convention entered into force in 2008 to prohibit the use of harmful organotin in anti-fouling paints used on ships, -i.e. TBT.

At MEPC 74, it was agreed to prohibit the use of anti-fouling paints that contains cybutryne under the AFS Convention. Moreover, MEPC 74 recognized that further consideration was necessary on the controls of cybutryne which has already been used on board existing ships.

MEPC 75 is expected to approve draft amendments to AFS Convention to prohibit the use of anti-fouling paints that contains cybutryne. For the controls of cybutryne which has already been used on board existing ships, the following requirements will be specified in the draft amendments to AFS Convention.

- Ships bearing an anti-fouling system that contains cybutryne in the external coating layer of their hull shall either remove the anti-fouling system, or apply a coating that forms a barrier to cybutryne.
- For ships of less than 400 gross tonnage engaged in international voyages, if accepted by the coastal States, no action required.
- For ships not engaged in international voyages, no action required.

Based on the above requirements, for ships bearing anti-fouling systems that don't contain cybutryne in the external coating layer of their hull, no action will be required.

2.5 Others

2.5.1 Marine Plastic Litter

With a view to tackling the problem of plastics in the oceans, MARPOL Annex V prohibits discharge of plastics from vessels. However, it was pointed out that this regulation was not effective enough and that some additional actions were needed at IMO level to reduce plastic pollution in the marine environment. To solve this problem, it was agreed to consider the issues, such as reporting of accidental loss or discharge of fishing gear, making garbage record book mandatory for smaller vessels, and obligation to report the loss of containers.

MEPC 75 will consider a "strategy to address marine plastic litter from ships" and timeline for discussion until 2025. MEPC 75 will also consider a proposal on marking of fishing gear with the IMO ship identification number.

2.5.2 Underwater Noise

MEPC 66, held in 2014, adopted "Guidelines for the reduction of underwater noise from commercial shipping to address adverse impacts on marine life (MEPC.1/Circ.833)".

MEPC 75 is expected to consider a proposal to establish new output for MEPC and SDC Sub-Committee to undertake a review of the Guidelines. If agreed, the review will be started at SDC Sub-Committee.

2.5.3 Heavy Fuel Oil in Arctic Waters

MEPC 72, held in 2018, recognized that most significant threat to the Arctic marine environment is the release of oil through accidental or illegal discharge from ships. PPR Sub-Committee has considered measures to reduce the risks of use and carriage

of heavy fuel oil as fuel by ships in Arctic waters.

MEPC 75 will approve draft amendments to MARPOL Annex I to prohibit the use and carriage for use as fuel of heavy fuel oil by ships in Arctic waters. The carriage of heavy fuel oil as cargo will not subject to the prohibition.

2.6 Amendments to Mandatory Instruments

MEPC 75 is expected to adopt amendments to mandatory instruments as follows:

(1) EEDI phase 3 requirements

Amendments to MARPOL Annex VI to strengthen EEDI phase 3 requirements.

- For container ship, advance starting year from 2025 to 2022, and strengthen the reduction rate based on the ship sizes as follows:

DWT	Reduction rate
10,000 and above but less than 15,000 DWT	15～30%
15,000 and above but less than 40,000 DWT	30%
40,000 and above but less than 80,000 DWT	35%
80,000 and above but less than 120,000 DWT	40%
120,000 and above but less than 200,000 DWT	45%
200,000 DWT and above	50%

- For general cargo ship, LNG carrier and cruise passenger ship, advance starting year from 2025 to 2022 and retain 30 % reduction rate.
- For gas carrier (LPG carrier) with 15,000DWT and above, advance starting year from 2025 to 2022 and retain 30 % reduction rate. For gas carrier (LPG carrier) below 15,000DWT, retain the current requirements of starting year in 2025 and the reduction rate.
- For ship types other than above, retain the current requirements of starting year in 2025 and the reduction rate.

(2) Reference line for large bulk carriers

Amendments to MARPOL Annex VI to relax the reference lines for very large bulk carriers more than 279,000DWT.

(3) Sampling of fuel oil used on board

Amendments to MARPOL Annex VI to mandate the designated sampling points for the verification of the sulphur content of fuel oil used on board ships, and amendments to Appendix VI of MARPOL Annex VI to specify verification procedures for the sulphur content of the fuel oil sample.

(4) Commissioning of Ballast Water Management Systems (BWMS)

Amendments to BWM Convention to specify the requirements to conduct commissioning testing, sampling and analysis.

3. TOPICS TO BE DISCUSSED AT MSC 102

3.1 Adoption of Amendments to Mandatory Instruments

MSC 102 is expected to adopt amendments to mandatory instruments as follows:

(1) Amendments to SOLAS regulation II-1/3-8 relevant to mooring equipment

MSC approved new “Guidelines on the design of mooring arrangements and the selection of appropriate mooring equipment and fittings for safe mooring” and new “Guidelines for inspection and maintenance of mooring equipment including lines”. Accordingly, MSC 102 will adopt amendments to SOLAS regulation II-1/3-8 to refer to those Guidelines.

(2) Amendments to B-1 to B-4 of SOLAS chapter II-1 to ensure consistency with regard to watertight integrity

(3) Amendments to IGF Code

Three (3) amendments to the IGF Code as listed below.

1. In paragraph 6.7.1.1, to remove tank cofferdams from the scope of requirement of pressure relief system.
2. To add new paragraph 11.8, in order to require fixed fire-extinguishing system for fuel preparation rooms.
3. To modify paragraph 16.3.3.5.1 concerning tensile tests for materials such as aluminium alloys.

(4) Amendments to IGC Code

As well as the amendments to the IGF Code as mentioned in above 3.1(3)3, amendments to paragraph 6.5.3.5.1 of the IGC Code concerning tensile tests for materials such as aluminium alloys.

3.2 Approval of Amendments to Mandatory Instruments

MSC 102 is expected to approve amendments to mandatory instruments as follows, with a view to adoption at future session.

(1) Amendments to SOLAS chapter III, LSA Code and resolution MSC.81(70)

Amendments to SOLAS regulation III/33, paragraph 4.4.1.3 of LSA Code and the "Revised recommendation on testing of life-saving appliances" (resolution MSC.81(70), as amended), to remove the applicability of the requirements to launch free-fall lifeboats with the ship making headway at speeds up to 5 knots in calm water, are expected to be approved.

(2) Amendments to 2011 ESP Code

Amendments to 2011 ESP Code, which reconsider the provision of thickness measurements at the first renewal survey of double hull oil tankers, would be approved.

(3) Amendments for watertight doors on cargo ships to LL, IBC Code and IGC Code

Amendments for watertight doors on cargo ships to LL regulation 27(13)(a), relevant parts of IBC Code and IGC Code would be approved.

(4) Amendments to chapter 9 of the FSS Code

Amendments to chapter 9 of the FSS Code in respect of fault isolation requirements for cargo ships and passenger ship cabin balconies fitted with individually identifiable fire detector systems, are expected to be approved

(5) Amendments to CSS Code (non-mandatory)

Amendments to CSS Code in order to include conditions for weather-dependent lashing, are expected to be approved. Further the amendments to the associated Guidelines (MSC.1/Circ.1353/Rev.1 and resolution A.581(14)) and 2011 TDC Code would also be approved.

3.3 Approval of Amendments to Guidelines

Amendments to "Guidelines for the maintenance and inspections of fixed carbon dioxide fire-extinguishing systems" (MSC.1/Circ.1318) to provide testing requirements for high pressure cylinders would be approved during MSC 102.

3.4 Second Generation Intact Stability Criteria

Current requirements of intact stability stipulated in SOLAS II-1 take into account static condition of ships, however, the problems related to dynamic stability failures have generally not yet been solved. SDC Sub-Committee has considered and developed the second generation of intact stability criteria to reflect the latest scientific knowledge.

SDC 7, held in February 2020, finalized draft interim guidelines on the second generation intact stability criteria for assessing five dynamic stability failure modes in waves, namely, dead ship condition, excessive acceleration, pure loss of stability, parametric rolling and surf-riding/broaching.

MSC 102 will consider and adopt the interim guidelines. Through the trial use of the interim guidelines, IMO will re-consider the interim guidelines at future sessions.

3.5 Water Level Detectors on Multiple Hold Cargo Ships

Following the sinking of ro-ro cargo ship "El Faro" in 2015, a revision of SOLAS was proposed to require installation of water level detectors in cargo ships with multiple cargo holds other than bulk carriers. SDC Sub-Committee considered the proposal and finalized draft amendments to SOLAS.

MSC 102 is expected to approve the draft amendments to SOLAS to add regulation for water level detectors on multiple hold cargo ships (ro-ro cargo ships and general cargo ships) for cargo holds located below the freeboard deck. The amendments will be applied to multiple hold cargo ships other than bulk carriers and tankers constructed on or after 1 January 2024.

3.6 Onboard Lifting Appliances and Anchor Handling Winches

Requirements for onboard lifting appliance are not specified in SOLAS and inspection for the lifting appliance has been conducted based on the requirements of flag States and port States. SSE Sub-Committee has been working on the requirements for inspection and maintenance for the lifting appliances, and SSE 7, held in March 2020, finalized draft amendments to SOLAS chapter II-I, to provide definition and application of lifting appliances and anchor handling winches, and to refer to two (2) new "Guidelines for anchor handling winches" and "Guidelines for lifting appliances" which are under development.

MSC 102 will approve the draft amendments to SOLAS, which will be applied to lifting appliances having a Safe Working Load above 1,000 kg on or after 1 January 2024. Once the associated draft Guidelines are finalized at SSE 8, the amendment to SOLAS chapter II-I would be adopted in conjunction with the approval of the draft Guidelines at MSC 103.

ClassNK Technical Journal

No.2 (2020 (I) issue)

Published by: Nippon Kaiji Kyokai (ClassNK) Research Institute

Address: 3-3 Kioi-cho, Chiyoda-ku 102-0094 Japan

Tel: +81-3-5226-2737

E-mail: ri@classnk.or.jp

ClassNK Technical Journal

NIPPON KAIJI KYOKAI
Research Institute
3-3 Kioi-cho, Chiyoda-ku, Tokyo 102-0094, JAPAN
Tel : +81-3-5226-2737
Fax : +81-3-5226-2736
E-mail : ri@classnk.or.jp

www.classnk.com

December 2020